TECHNISCHE UNIVERSITÄT MÜNCHEN
Lehrstuhl für Biologische Bildgebung
Chair for Biological Imaging

Thermoacoustic Imaging in time and frequency domain. Theory and experiments

Dipl.-Ing. Univ. Stephan Kellnberger

Vollständiger Abdruck der von der Fakultät für Elektrotechnik und Informationstechnik der Technischen Universität München zur Erlangung des akademischen Grades eines

Doktor-Ingenieurs

genehmigten Dissertation.

Vorsitzender: Univ.-Prof. Dr.-Ing. habil. Gerhard Rigoll

Prüfer der Dissertation:

1. Univ.-Prof. Vasilis Ntziachristos, M.Sc. Ph.D.
2. Prof. George Sergiadis, Ph.D.,
   Universität Thessaloniki/Griechenland
3. Univ.-Prof. Dr.-Ing. Norbert Hanik

Die Dissertation wurde am 17.08.2012 bei der Technischen Universität München eingereicht und durch die Fakultät für Elektrotechnik und Informationstechnik am 27.02.2013 angenommen.

Abstract

Imaging based on the photoacoustic effect is primarily performed with optical excitation, employing ultrashort nanosecond laser pulses of high energy to excite acoustic pressure waves. Optoacoustic imaging provides high resolution with optical contrast and offers versatile applications like the ability to perform structural imaging, functional diagnosis and molecular monitoring of biological processes.

Changing excitation to a different energy level, photoacoustics can also be implemented by employing low frequent radiowaves or microwaves, giving rise to thermoacoustic imaging. Wavelength alteration comes along with different contrast which is based on the conductive, dielectric and magnetic properties of tissue but also with higher penetration depth. Thus, thermoacoustic imaging is potentially capable of whole human body imaging at ultrasound resolution. Despite its overall potential, thermoacoustic imaging has not yet become a widespread biomedical diagnosis tool since thermoacoustic approaches are facing relatively low spatial resolution. Additionally, until now thermoacoustics as a diagnosis tool can only provide anatomical imaging of soft tissue with respect to the lack of appropriate RF or microwave contrast agents.

This thesis aimed at developing alternative technologies and implementations in the field of photoacoustic imaging. A novel RF excitation model is proposed which overcomes the resolution limitations of thermoacoustic tomography, enabling small animal imaging. The main focus of this research directed at the thermoacoustic implementation of molecular and functional methods. Starting with an initial design which operated in the time domain employing ultrashort RF pulses, the effort further developed into frequency domain implementations with respect to the deficiencies the time domain has over the frequency domain.

Thus, dedicated experimental setups evolved which show the steady transition from pulsed sources, employed in time domain thermoacoustics (TD-TAT), to modulated CW sources implemented in frequency domain thermoacoustics (FD-TAT). This gave rise to a preliminary frequency domain optoacoustic tomography system, the first of its kind while also advancing thermoacoustics to the implementation in the frequency domain.

In particular the FD-TAT system is believed to open new applications in the field of RF

based photoacoustic tomography, thus providing a powerful biomedical diagnosis tool which could also be used as a theranostic system for cancer treatment and monitoring.

Acknowledgements

This dissertation would not have been possible without the guidance and support of several individuals who accompanied me during the last years and in one way or another contributed their valuable assistance in the preparation and completion of this research.
First and foremost, my grateful thanks go to my advisor Prof. Dr. Vasilis Ntziachristos who accepted me as his PhD student and always gave me enough freedom and encouragement to carry out unconventional scientific approaches. It has been a pleasure and honor likewise to work with him and learn from his deep insights in all fields of imaging.
My deepest thanks also go to Prof. Dr. George Sergiadis who brought intense light into the darkness during the last years, supporting me with profound insights into the field of RF engineering but more importantly inspiring me beyond technical aspects.
I am especially grateful to my supervisor Dr. Daniel Razansky who came up with the idea of near-field thermoacoustic imaging and assisted me with his enormous technical expertise and knowledge not only in the field of thermoacoustic and optoacoustic imaging.
Many thanks go to Dr. Amir Hajiaboli who joined me in the thermoacoustic group at the IBMI and Murad Omar who became a thermoacoustic member only one year later. Their input encouraged me during this work.
I would like to thank Dr. Amir Rosenthal who (unknowingly?) became a valuable and important part of the thermoacoustic imaging group and shared a portion of his deep knowledge in theoretical insights with me.
I am grateful to Dr. Nikolaos C. Deliolanis for giving me the opportunity to participate in the development of the frequency domain optoacoustic system.
I wish to thank all the people at the IBMI who contributed in valuable discussions, technical support, theoretical feedback and scientific advice. I would like to thank Andreas Buehler for being my roommate and sharing his opinions with me, Dr. Jérôme Gâteau for his immense insights in ultrasound physics, Dr. Nicolas Bézière for assisting me in nanoparticle preparation, Adrian Taruttis for his suggestions regarding complex optoacoustic problems, Dr. Xosé Luís Deán Ben for his advice in optoacoustic theory and experiments, Miguel Ángel Araque Caballero for his expertise in ultrasound applications, Andreas Oancea for his support in various mechanical and technical issues, Marcin

Kacprowicz for his feedback in laser and fiber applications, Josef Konradl for his profound expertise whenever technical problems came up, Erwin Bay and Dmitry Bozhko for sharing various hardware components with me, Pouyan Mohajerani for sharing his scientific and personal opinions and Daniel Queirós for his participation in the development of the FD-OAT system.
My special thanks go to Zsuzsanna Öszi, Susanne Stern and Silvia Weinzierl in various aspects of administration, organisation and ordering.
Further thanks and acknowledgements go to Sarah Glasl, Florian Jurgeleit and Uwe Klemm who assisted me in thermoacoustic and optoacoustic experiments whenever mice were involved.
I am also grateful to Simon Brassel who assisted me during his bachelor thesis.
Special thanks go to Dr. Andreas Murr for technical and also personal discussions.
Finally, the success of this work would not have been possible without the unlimited help of my beloved family who always guided me through life and backed my decisions as well as Karin Radrich for her scientific and personal support which encouraged and motivated me during the last years.

Contents

List of Figures

List of abbreviations

AC	Alternating current
AOM	Acousto optic modulator
CT	Computed Tomography
CW	Continuous wave
DAQ	Data acquisition
DC	Direct Current
DOT	Diffuse optical tomography
EM	Electromagnetic
EMI	Electromagnetic interference
FD	Frequency domain
FDTD	Finite difference time domain
FEM	Finite element method
FF	Far field
FFT	Fast Fourier Transform
FMT	Fluorescence Molecular Tomography
FWHM	Full width half maximum
Hb	Deoxygenated hemoglobin
HbO_2	Oxygenated hemoglobin
HV	High voltage
IBMI	Institute for Biological and Medical Imaging
ICG	Indocyanine Green
Laser	Light Amplification by Stimulated Emission of Radiation
LSQR	Least square
LV	Low voltage
MI	Microwave imaging
MRI	Magnetic resonance imaging
MPE	Maximum Permissible Exposure
Nd:YAG	Neodymium doped yttrium aluminium garnet
NF	Near field
NIR	Near infrared

NRT	Near field radiofrequency thermoacoustic tomography
OA	Optoacoustics
OAT	Optoacoustic tomography
OCT	Optical Coherence Tomography
PA	Photoacoustics
PAT	Photoacoustic tomography
PC	Personal computer
PCB	Printed circuit board
PET	Positron Emission Tomography
PG	Pulse Generator
PRF	Pulse Repetition Frequency
PVDF	Polyvinylidene fluoride
PZT	Piezoelectric transducer (lead zirconate titanate)
quasi CW	Quasi continuous wave
RF	Radiofrequency
ROI	Region of interest
SHG	Second harmonic generation
SNR	Signal to noise ratio
SP	Signal Processing
SPECT	Single Photon Emission Computed Tomography
TA	Thermoacoustics
TAT	Thermoacoustic tomography
TD	Time domain
TL	Transmission line
US	Ultrasound
UV	Ultraviolet

1 Introduction

1.1 Opto- and thermoacoustics in the context of imaging

Imaging is essential in biological discovery and medical diagnosis. Looking back to an eventful history which goes back more than 100 years with the discovery of X-rays, imaging passed through decisive and radical changes in particular in the last decades. Ongoing research is geared towards exploiting new contrast mechanisms and pushing sensitivity and resolution boundaries. Especially optical methods are of particular interest since they proved to be ”a powerful modality in biological discovery” [88].

Photoacoustic imaging in particular represents a relatively new imaging method which covers the entirety of imaging applications: It can be employed on a microscopic level, furthermore it is highly applicable for mesoscopic imaging and finally it can also be used as a macroscopic imaging tool. Technically speaking, photoacoustic imaging can not be regarded as a classical multi-modality imaging instrument. Instead, photoacoustics uses one kind of energy for excitation (electromagnetic energy, e.g. optical light or radiofrequencies) and measures the tissue response as an acoustic wave (ultrasonic detection) or in more simple words, we ”listen to light” [88]. The underlying physical phenomenon, i.e. the photoacoustic effect, was discovered by Alexander Graham Bell [5] in the year 1880. Bell investigated in simple experiments the correlation between absorption of transient electromagnetic energy and the following induction of mechanical waves. Although the effect was well known, it was not until the development of lasers which finally gave rise to optoacoustic imaging in 1981 [92], [106].

The availability of lasers determined the fate of optoacoustic imaging. Ultrashort optical pulses with wavelengths in the Near Infrared (NIR) marked the gold standard for optoacoustic imaging implementations. Applications are not only versatile but seemed to be unlimited since optoacoustics offers high resolution, good (both intrinsic and extrinsic) imaging contrast, fair penetration depth, low artifacts and safe diagnosis.

Besides optoacoustic imaging, it was also in the same time period that the photoacoustic effect was proved using electric pulse stimulation [10] instead of optical pulses. Thermoacoustics arose, which basically terms the thermoelastic expansion in the photoacoustic effect, but more specifically relates to stimulation with Radiofrequency (RF)/microwave electromagnetic energy.
Although thermoacoustics is similar to optoacoustics, simply due to the broader application range and easiness of implementation, optoacoustics has become the workhorse in imaging based on the photoacoustic effect.

During the same time period a third implementation type was discovered. In Rosencwaig's patent [106] a thermoacoustic imaging system was reported which employed a CW modulated electromagnetic source instead of a pulsed generator. Again, this gave rise to novel imaging systems which operated in the frequency domain instead of the pulsed source time domain approach.

Not only these milestones in thermoacoustic imaging but also major applications in biomedical diagnosis demonstrate that thermoacoustic imaging is a methodology which has not yet found its evolutionary dead end. Alternative time domain thermoacoustic implementations in the near-field can potentially overcome resolution limitations while maintaining signal to noise ratio. The near-field thermoacoustic imaging approach which is an important focus of this work describes ultrashort excitation of biological tissue in the close vicinity of radiofrequency or microwave sources where energy coupling is significantly high. Thus, the near-field method is able to provide superior spatial resolution without compromising signal to noise ratio.
Moreover, frequency domain implementations using both optical light and RF for stimulation of tissue demonstrate that thermoacoustic imaging is still at its beginning. Especially with respect to the latter implementation, this work directs the reader towards further possible applications and technological trends of thermoacoustic imaging.

1.1.1 Gaps in imaging modalities

Chart 1.1 depicts current biomedical imaging modalities as a function of penetration depth and resolution. Apparently, there is no optimal imaging technology that can provide ultrahigh resolution while at the same time penetrate soft tissue up to tens of cm. Optical Coherence Tomography (OCT), for instance, provides high resolution with reasonable penetration depth as compared to confocal microscopy [98] which is limited

to few hundreds of microns depending on the tissue [26]. Preferred applications of OCT lie in the field of ophthalmology [118] and coronary artery disease imaging [75].
X-ray Computed Tomography (CT) and MRI (Magnetic Resonance Imaging) offer both high resolution at ~ 50 µm [87] with high penetration depth, suitable for visualizing anatomical structures. MRI particularly yields good contrast from soft tissue. Both technologies are ideal for whole body imaging at high resolution.
Ultrasound (US) imaging is another category which offers high resolution and fairly good penetration depending on the US frequency.
Referring to nuclear imaging techniques, PET (Positron Emission Tomography) and SPECT (Single Photon Emission Tomography) provide functional and molecular imaging like molecular breast cancer imaging [97] or cardiovascular imaging [24].
Microwave imaging (MI) is mainly employed for breast cancer imaging due to the contrast which is based on permittivity and conductivity of soft tissue. MI illuminates objects with microwaves and detects the scattered field after propagation through soft tissue. Although whole body imaging with safe nonionizing radiation is feasible, the main drawback in MI imaging is to be found in diffraction effects which result in limited resolution [64]. The overall spatial resolution was previously limited to ~ 5 mm equivalent to half the wavelength [73], but recent developments improved the resolution in current implementations to $1-2$ mm [9].

Taking a look at the second chart 1.2 which shows the implementation type (factors like cost, complexity) versus the imaging application reveals several gaps in the application range. PET and SPECT are highly sensitive imaging modalities (typically in the order of fmol [87]), but are limited to functional and molecular imaging. Thus, PET is often combined with X-ray CT which provides anatomical contrast. However, PET/SPECT and X-ray CT especially in a combined system are associated with greater cost and moreover use ionizing radiation.
Thermoacoustic Tomography (TAT) and Optoacoustic Tomography (OAT) can close this gap, thus providing anatomical, functional and molecular imaging (the latter ones in particular covered by optoacoustics). Numerous advantages are associated with the photoacoustic method: Being a combination of basically two different technologies, thermoacoustics overcomes limitations of pure optical imaging and unifies the benefits of ultrasound and optical imaging in one modality. This is in particular useful in optoacoustics where specific intrinsic optical contrast is coupled with high ultrasound resolution, thus creating an imaging system which is able to perform anatomical imaging with optical contrast [76], functional imaging, e.g. monitoring ICG perfusion [16] and molecular imaging [87], [22]. Moreover, costs and complexity of the optoacoustic

method is fairly low since it uses ultrasound detection and optical excitation. The full capabilities of optoacoustics will be explained later in this chapter.
Thermoacoustics, on the other hand, offers anatomical permittivity and conductivity contrast similar to the one from microwave imaging, but is limited in terms of functional and molecular imaging (only one group reported on molecular imaging with the thermoacoustic method [82]). Typical problems of conventional thermoacoustics represent a main focus of this work and are extensively discussed later.

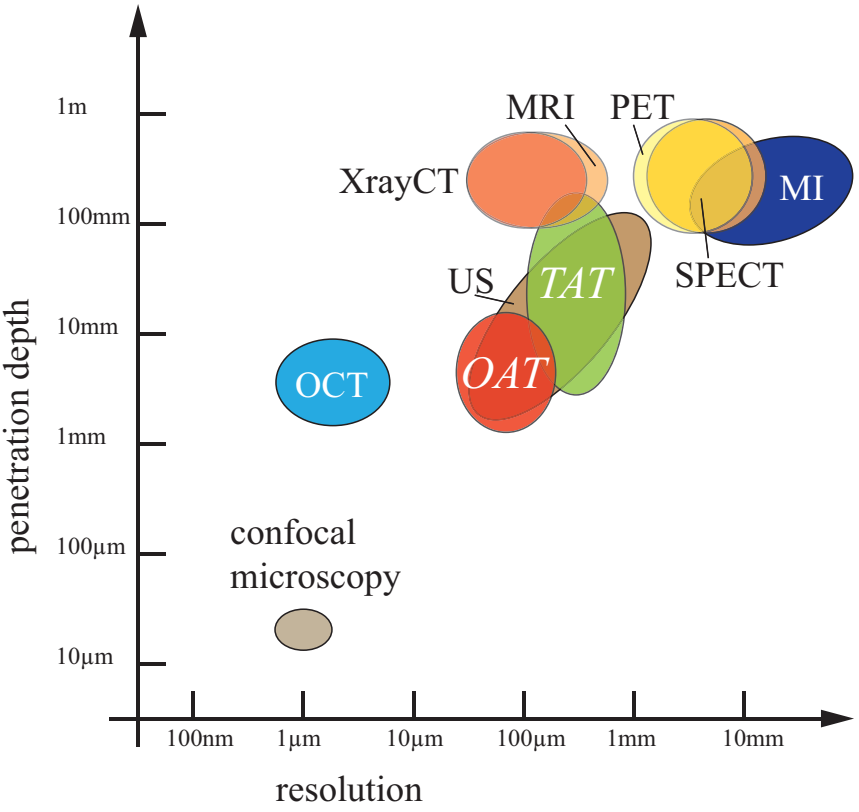

Figure 1.1: Current biomedical imaging modalities: OCT - Optical Coherence Tomography; X-ray CT - X-ray Computed Tomography; US - Ultrasound; OAT - Optoacoustic Tomography; TAT - Thermoacoustic Tomography; MRI - Magnet Resonance Imaging; PET - Positron Emission Tomography; SPECT - Single Photon Emission Computed Tomography; MI - Microwave Imaging (according to [26], [87])

1.1.2 Importance of hybrid imaging

A popular approach to cover the gaps in current imaging modalities is the combination of different technologies. Advantages are obvious: Not only that the drawbacks coming along with one system are overcome but also the benefits that are distinct to each system

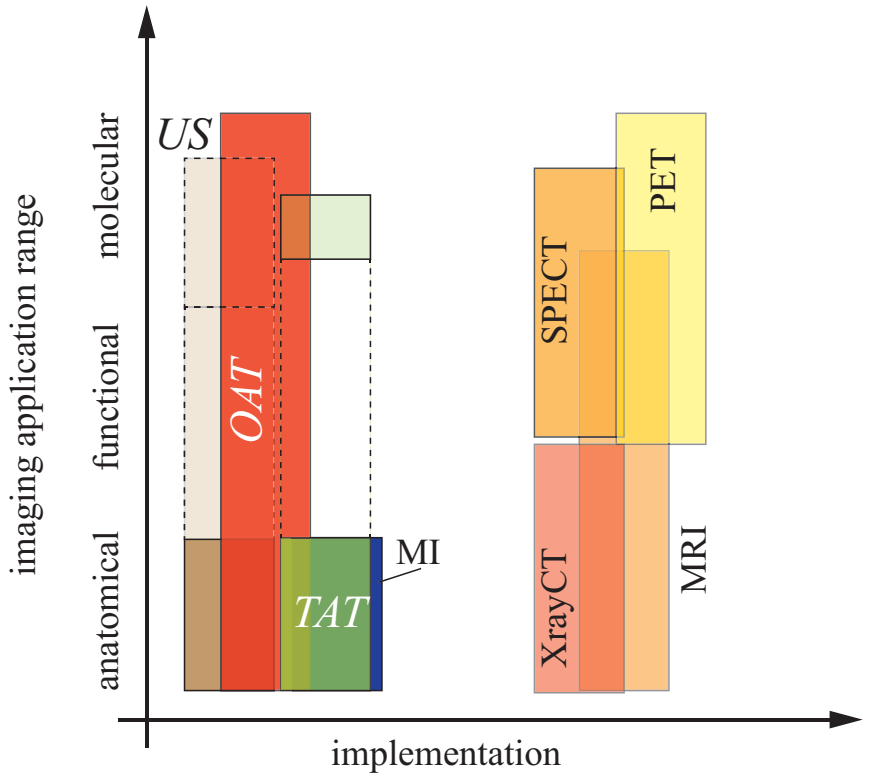

Figure 1.2: Biomedical imaging modalities as a function of imaging applications and implementation (abbreviations see figure 1.1) (according to [85])

are added up. In other words, two systems can be in a way combined complementary so that the resulting imaging system unifies the advantages of both methodologies in one method.

Referring back to figure 1.2, a combination of X-ray CT with PET results in a new imaging method which can provide structural images with molecular and functional imaging applications.
Similarly, MRI and PET can be unified in one system offering soft tissue contrast coupled with molecular and functional applications [55].

In the same line, photoacoustics is a so called hybrid imaging modality since it combines ultrasound and optical/RF/microwave imaging in one modality. Thus, thermoacoustic imaging yields high resolution images of electrical, dielectric or magnetic contrast whereas optoacoustics generates high resolution images providing optical contrast.

1.2 Basics on thermoacoustic imaging

1.2.1 Introduction - the photoacoustic effect

The photoacoustic effect describes the local absorption of electromagnetic energy in tissue followed by mechanical stress waves. When exposed to electromagnetic radiation, tissue is heated up and generates an acoustic pressure wave due to thermoelastic expansion. The mechanical pressure wave can be captured by appropriate pressure detectors which are coupled to the tissue using e.g. water as a coupling medium.
The amplitude of the generated acoustic pressure wave is dependent on the amount of energy absorbed and the time scale at which the energy is deposited in the tissue.
A profound explanation to the photoacoustic effect is introduced in chapter 2.

1.2.2 Thermoacoustics vs. optoacoustics

Two imaging modalities emerged over the past years using different energy regions in the electromagnetic spectrum (see 1.3). However, the generation of acoustic waves following electromagnetic absorption is not limited to the optical and RF/microwave region. In [38], the photoacoustic effect was also investigated using X-rays to excite acoustic waves.
In compliance with the photoacoustic scientific community, this thesis employs the terminology depicted on figure 1.4 where thermoacoustics is employed to determine generally any form of energy absorption by tissue while optoacoustics more specifically reflect optical energy absorption. Photoacoustics moreover refers to the general term when the photoacoustic effect is involved. Therefore, methods including the photoacoustic effect can be clustered into Optoacoustic imaging (OAI) and tomography (OAT) which describe the induction of pressure waves following light absorption whereas thermoacoustic imaging (TAI) and tomography (TAT) commonly relate to all bands of the electromagnetic spectrum, including but not limited to the radiofrequency and microwave bands.

However, there are several aspects that favor the optical and RF/microwave region of the electromagnetic spectrum as illustrated on figure 1.4. First of all, both energies are nonionizing and therefore safe for human and animal imaging applications. Second, both energy regions offer soft tissue contrast. The contrast mechanism for optical and RF excitation will be explained in chapter 2. Third, the RF region and to a lesser extent the optical band provide relatively high penetration depth into biological tissue.

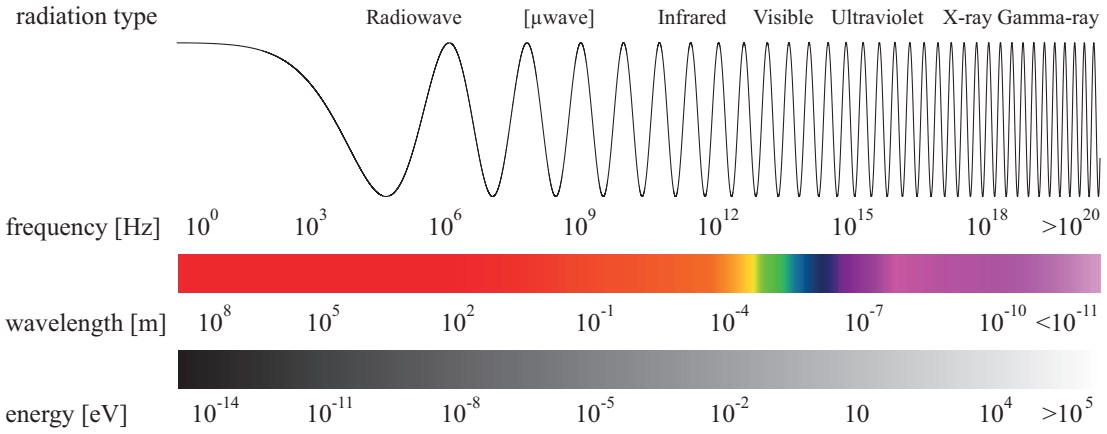

Figure 1.3: Electromagnetic spectrum showing the wavelength with the corresponding frequency and energy from radiofrequencies (RF) to Gamma-rays

Referring in particular to the last point, the absorption coefficient of water over wavelength is plotted on figure 1.5. An optical window covering a wavelength band from $\sim$ 400 nm - 700 nm is clearly visible. Leaving the window either towards higher wavelength (NIR) or lower wavelength (UV) changes the absorption characteristics decisively. Moving to very high wavelength, the absorption coefficient of water decreases gradually. In the microwave region, water still exhibits high absorption whereas in the RF region the absorption further decreases. The absorption mechanisms are further explained in chapter 2.

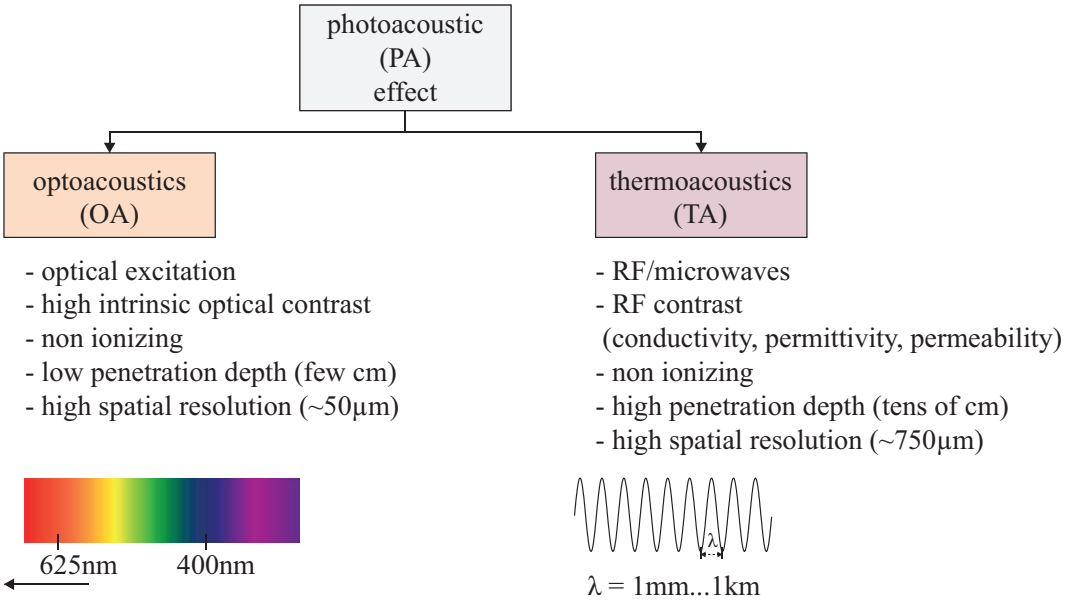

Figure 1.4: Photoacoustic (PA) imaging clustered into its derivatives optoacoustic (OA) imaging when light is used for stimulation of tissue and thermoacoustic (TA) imaging when RF/microwaves are employed to excite acoustic waves from tissue

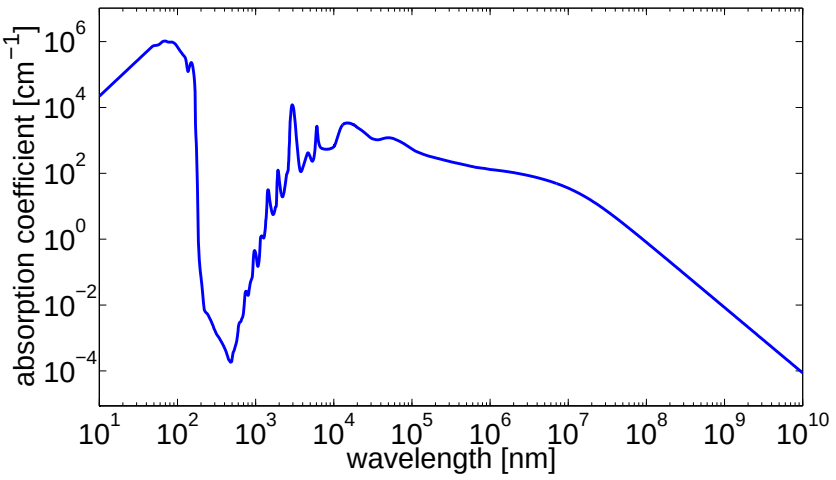

Figure 1.5: Absorption spectrum of water (according to [113])

1.2.3 From time domain to frequency domain

Basically, almost the entirety of important imaging modalities started in time domain before crucial research outcomes paved the way for frequency domain applications. Optical Coherence Tomography, for example, has its origin in the time domain before ”a major revolution [brought] Fourier domain techniques [...] to OCT” [26]. This fourier domain revolution gave rise to two imaging methodologies in addition to the time domain OCT (TD-OCT), namely spectral domain OCT (SD-OCT) and swept source OCT (SS-OCT) [26]. Both the swept source system and the spectral domain system drop the translation stage which is a characteristic feature of time domain OCT. SS-OCT instead employs a tunable light source with narrow spectrum. The sweeping of the wavenumber is equivalent to translating the reference mirror. In SD-OCT, the reflected beam from a broadband light source is dispersed, simultaneously detecting all spectral components of the reflected light.
Benefits that come along with the fourier domain approach include signal to noise ratio improvement by several hundreds [21] by using a spectral domain system and drastic measurement speed improvement since moving elements (i.e. the translation stages) are removed in FD approaches [132].

Similar to OCT, diffuse optical tomography (DOT) can also be implemented in the time domain and frequency domain. Referring to time domain systems, one implementation was described by Ntziachristos et al. [86] in which ultrashort pulses of light were used to illuminate tissue. After propagating through tissue, the temporal point spread functions (TPSF) are broadened because of scattering effects and captured with photon

detectors.
Contrary, frequency domain diffuse optical imaging employs continuous wave light sources which are intensity modulated at a few hundred MHz (see Chance et al. [17]). Reemitted light from the object is reduced in modulation depth and captured with a photon multiplier tube (PMT) using e.g. homodyne or heterodyne detection of the modulated light.
In DOT, the advantages and disadvantages between the TD and FD implementation are much more versatile since each methodology provides distinct benefits. The time domain system offers high sensitivity with higher information content in the measured data, however it also comes along with an expensive setup and long acquisition times. The frequency domain methodology is faster, less expensive but also provides less information because of the single modulation frequency of the light source. Practically, since time domain and frequency domain are linked through the fourier transform, both domains are similar if the frequency domain is measured over a large enough bandwidth to cover the information that is gathered from the short time duration.

Photoacoustics also provides this dual domain implementation, i.e. photoacoustics can be performed in time domain and accordingly in frequency domain. In what follows, both methodologies will briefly be introduced, itemizing the characteristics of each technology as depicted on figure 1.6 and pointing out the benefits that are connected to imaging either in the time domain or frequency domain.

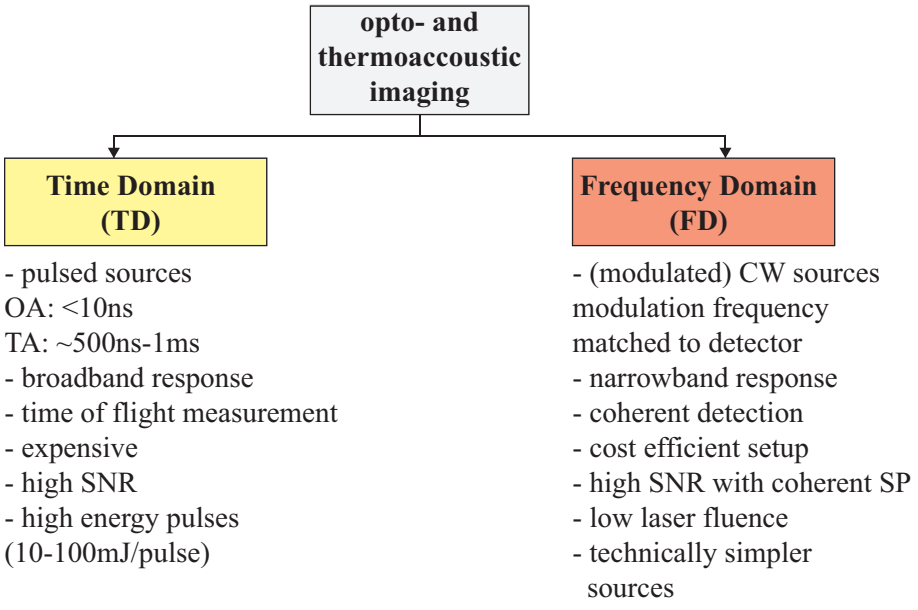

Figure 1.6: Comparison time domain and frequency domain

Time domain photoacoustics

In time domain photoacoustics, the entire pulse period is used for acoustic (either optically or RF/microwave induced) signal generation. Therefore, the time domain approach employs pulsed sources of light in the case of optoacoustics and short RF/microwave pulses for thermoacoustic imaging. The optical pulses are generally below 10 ns (see [100]) which allow for high resolution imaging whereas thermoacoustic pulses are confined to a lower threshold of $\tau_{pulse} \approx 500$ ns due to technical restrictions [64]. Pulsed excitation is followed by a broadband acoustic response from absorbing tissue, thus the acoustic signals inherently contain information on the absorber's dimensions in the spectral components of the measured acoustic waveforms. Furthermore, time domain photoacoustics features time of flight measurements, referring locally induced acoustic pressure signals to distance from the detector with the acoustic wave speed - propagation time dependence. High signal to noise ratio is usually achieved by illuminating the sample with high energy pulses, reaching energy levels of $10 - 100$ mJ. Operation in pulsed mode is typically associated with a complex technical setup and expensive sources. As an example, ultrashort high energy light pulses are usually generated with a tunable optical parametric oscillator laser which is pumped by a Q-switched Nd:YAG laser. Those sources are generally expensive in purchasing and maintaining. Short RF/microwave pulses are most commonly created with a pulsed high frequency generator followed by a high power amplification stage. Similar, those systems need to provide sufficient energy to induce detectable thermoacoustic signals.

Frequency domain photoacoustics

In frequency domain photoacoustics, acoustic signals are generated during the time interval that the source is on, i.e. signals are even detected if the stimulation signal is extended over long time intervals. Whereas in time domain one pulse defines one imaging acquisition window during which signals are captured, frequency domain drops the distinct time space relationship which is a typical feature of time domain systems. In frequency domain, preferably CW sources or sources which generate extremely long pulses are used. The narrowband stimulation profile due to monofrequent CW stimulation induces narrowband photoacoustic signals continuously for the time interval that the source is on. Spatial distribution of absorbers can be retrieved with correlation methods such as pulse compression. Whereas time domain systems usually employ expensive and bulky sources (e.g. OPO-Lasers, RF/microwave amplifiers), frequency domain setups rely on cost efficient sources like diode lasers or narrowband LEDs. Those diode modules are very compact and technically simple due to the high duty cycle. While pulsed lasers

have duty cycles in the order of $0.1\% - 10^{-5}\%$ where the average power is delivered within nanoseconds to achieve high energy pulses, CW lasers exhibit duty cycles of 100% spreading the energy over a longer time. This also results in a lower laser fluence, thus ensuring safe operation conditions for patients.

1.3 Objectives and motivation

From the very beginning, the goal of this research was to push thermoacoustics to small animal imaging in particular covering structural, functional and also molecular imaging. This approach required decisive improvements in image quality, especially in terms of resolution and easiness of implementation and furthermore a comprehensive study on the application of contrast agents or RF/microwave markers which are to be used for functional and molecular imaging purposes. In order to achieve this, the following questions have to be answered:
▷ With respect to established thermoacoustic imaging systems, how can we improve on image quality?
▷ Relating to thermoacoustic tomography, what are the steps to perform structural, functional and molecular imaging?

Both questions imply numerous more profound subcategories like:
► What is the optimal RF excitation waveform (both for high spatial resolution and molecular imaging)?
► How can this RF excitation be implemented in terms of hardware and technology?
► What are the sources of contrast in RF thermoacoustics?
► In particular referring to extrinsic contrast agents, what kind of probe material can be used in order to enhance contrast in thermoacoustic imaging?

These questions are only covering the overall objectives and aims of this research.

1.4 A short introduction to technical implementations

During this research, four different thermoacoustic and optoacoustic systems were built, starting in time domain thermoacoustics with the near-field radiofrequency thermoacoustic (NRT) tomography setup (see chapter 5), moving to frequency domain optoacoustics (chapter 6), then discussing a novel method in chapter 7 while completing the overview

of the experimental systems with the frequency domain thermoacoustic instrumentation (8). Therefore, this research focuses both on theoretical considerations on the photoacoustic phenomenon, in particular on novel excitation modes while at the same time covering experimental implementations of dedicated imaging systems.

1.5 A brief synopsis

This work directs the reader in nine chapters from an introductory section, dealing with fundamental theoretical considerations on the photoacoustic phenomenon, to experimental results based on theoretical findings.
The subsequent chapter 2 starts with theoretical aspects and physical explanations of the photoacoustic effect. It aims at giving a conceptual background for the following chapters which deal with optoacoustic and thermoacoustic signal generation and imaging.
Chapter 3 discusses the photoacoustic effect in frequency and time domain, using a CW modulated source for the former or a pulsed electromagnetic energy source for the latter.
In chapter 4, the basic image reconstruction formulas in time domain and frequency domain are presented.
Proceeding to chapter 5, a novel time domain thermoacoustic imaging system is discussed. First high resolution images of dissipative media, phantoms and an *ex-vivo* mouse are shown which are obtained with the developed system.
The thesis focuses on time and frequency domain imaging, thus an original approach towards optoacoustic imaging using a CW modulated laser is presented in chapter 6. Here, first frequency domain *in-vivo* cross-sectional images of a mouse using a dedicated tomographic imaging system are presented.
Chapter 7 discusses a novel concept of generating thermoacoustic signals employing an intermediate state between pulsed and CW excitation, namely quasi CW thermoacoustics.
Chapter 8 completes the process from theory and physics of photoacoustics to experimental results. Particular effort was devoted to the development and set-up of a high power amplifier which enables magnetic excitation with an adjustable frequency. As a highlight, this chapter presents for the first time a detected thermoacoustic signal following CW excitation at low frequencies in the MHz range.
Finally, chapter 9 is dedicated to conclusions and reconsiders the findings from this work. Particularly, it shows future directions of the thermoacoustic method using CW modulated sources.

2 Theory and physics on thermoacoustics

2.1 Introduction

This chapter directs the reader towards the theory and physics of thermoacoustic signal generation and should be considered as the basic reference for the following chapters. It starts with fundamental considerations on the electromagnetic wave - matter interaction. The basic governing equations of the photoacoustic effect are explained both for optical and RF/microwave excitation. A key point is covered by contrast mechanisms, reviewing optical contrast but also explaining the contrast which can be attained from RF and magnetic excitation.

2.2 Interaction of radiation with matter

This section describes the processes involved in radiation - matter interaction that are related to opto- and thermoacoustic imaging. It starts with a framework of interaction types before explaining in greater detail the corresponding mechanisms.
Consider a photon which is hitting a medium (e.g. a mouse) as depicted in figure 2.1. Basically, three different events can occur depending on properties like e.g. energy of the photon, type of medium, size of medium etc. Figure 2.1 depicts in a simplified way the different types of interaction. According to a first mechanism, photons can be absorbed partially or fully by the medium, thus transferring a part or all of its energy. The process of energy transfer will be explained later. The second mechanism refers to scattering of the photon upon propagating through the medium. Biological tissue represents a turbid medium and therefore exhibits strong optical scattering of photons. Finally, interaction of radiation with matter can also occur in the form of transmission. In this case, the

direction and energy of the photon is not affected and the photon is propagating through the medium. The medium can be regarded as transparent to the photon.

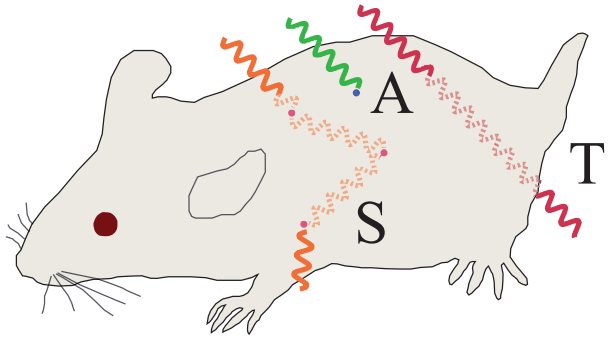

Figure 2.1: Photon interaction with matter: A (green) - Absorption; T (red) - Transmission; S (orange) - Scattering; (dashed lines represent photon propagation within tissue)

2.2.1 Absorption of radiation

Absorption of radiation by matter is of considerable interest for opto- and thermoacoustic imaging since acoustic waves are induced at spots of local electromagnetic energy absorption. This section aims at giving a fundamental understanding of the different absorption mechanisms. With regard to the implementation of both thermo- and optoacoustics, absorption is discussed for the whole electromagnetic spectrum as shown in figure 1.3, starting from low energy levels (RF), reaching the optical spectrum and finally discussing gamma rays at higher energies.

Figure 2.2 reviews again different energy levels on a logarithmic scale. The different absorption mechanisms are given above the energy bar relating to the corresponding energy band.

2.2.1.1 Absorption mechanisms across the EM spectrum

[a] Molecular rotation

Starting from low energy levels, absorption of radiation is taking place in the form of molecular rotation. Corresponding energy levels are in the order of 5 µeV - 1meV which is equivalent to the microwave region of the electromagnetic spectrum. The low frequent radiation is dissipating energy in form of frictional movement of molecules due to a rotational and torsional momentum which is exerted on the axis of the molecules (see

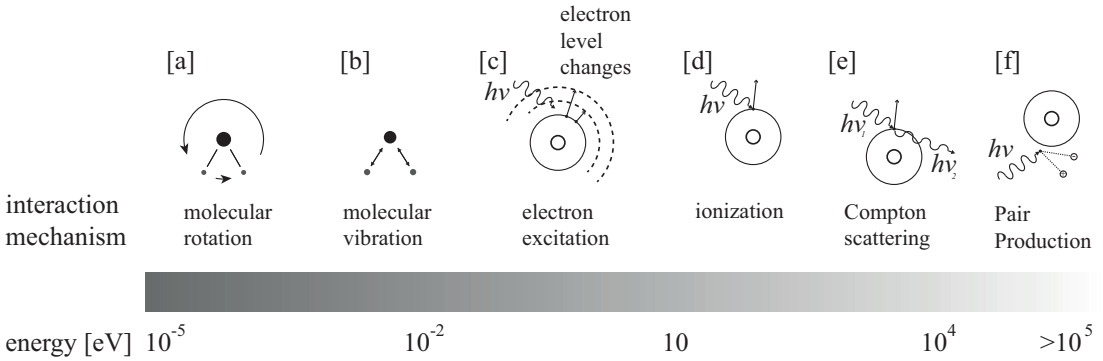

Figure 2.2: Interaction of radiation with matter, starting at low energy levels corresponding to RF while moving towards higher energy levels in the visible spectrum (marked as [c]) and finally reaching ultrahigh energies where Compton scattering [e] and Pair Production is taking place [f] (adapted from [50])

figure 2.2).
In biological tissue, microwave energy is converted into heat because of molecular motion; however, absorption of electromagnetic energy is comparably low since biological tissue is mostly transparent in the microwave band.
Metallic matter like conductors, on the other hand, exhibits significant absorption of microwaves and radiowaves in general. This is due to electric currents which are induced in conductive materials and which result in significant heat release when exposed to radiowaves and microwaves.

[b] Molecular vibration
A second form of molecular motion is occurring at higher energies in the infrared region (IR). When soft tissue is exposed to infrared radiation, energy is taken up in the form of vibrational motion of molecules, resulting again in heat release due to frictional movement (see inset [b] in figure 2.2). Whereas biological tissue exhibits relatively low absorption of RF (depending on the frequency), infrared offers higher absorption but is still less absorbing than optical light.

[c] Electron excitation
In the visible region of the electromagnetic spectrum, absorption of radiation is typically high. Photons elevate electrons from stable energy states to higher excited states, changing the orbital levels of electrons in the individual molecule. Inset [c] in figure 2.2 schematically depicts a photon of energy $E_{ph} = h\nu$ which excites an electron to a higher discrete energy level. It has to be noted that the electron excitation is a nonionizing effect, meaning that the electron of a molecule is not removed after absorption.
The holistic approach towards electron excitation will be explained later in this section.

[d] Ionization
Moving to the Ultraviolet (UV) spectrum, biological tissue becomes more absorbing, thus limiting the penetration depth of photons in tissue. Whereas photon interaction in the optical spectrum is of nonionizing nature, UV light (and X-rays) cause photoionization. As depicted in inset [d] on figure 2.2, photoionization describes the physical effect of expelling an electron from a molecule or atom in response to absorption of ionizing radiation, producing free radicals.

[e] Compton scattering
Advancing to even higher energy levels beyond the UV spectrum, other physical phenomena like Compton scattering take place. The effect is schematically illustrated in inset [e] in figure 2.2. Similar to the photoionization process, a photon with sufficient enough quantum energy (in the order of hundreds of keV) expels an electron from a molecule or atom since the energy exceeds the discrete energy levels of electron excitation. But in addition to the ionization, a second process takes place which results in a scattered photon balancing the energy of the incoming photon and the energy that is absorbed by knocking out the electron.

[f] Pair Production
Finally, although not of importance for the photoacoustic effect but for the sake of completeness, pair production occurs at high energies exceeding 1MeV. Here, interaction of a photon of sufficient energy with a nucleus ends up in a pair of positron and electron. The corresponding illustration is depicted in inset [f] in figure 2.2.

2.2.1.2 Absorption in the visible spectrum

The preceding paragraph presented a generic view over different absorption mechanisms depending on the energy of radiation.
In what follows, the absorption of light by biological tissue, also with respect to the emission effects, is explained.

Basically, absorption of photons in biological tissue can be described by an energy transfer from the photon to the atom or molecule. If photons hit a molecule, energy from the photon can elevate the electron to a higher energy level or raise the molecule to a higher rotational or vibrational state. There are various scenarios in which the absorbed energy can be released. The interested reader is referred to a profound description of light

matter interaction which can be found in the book 'Biomedical Optics' from Wang [125] which also served as the reference for the following explanation.

The Jablonski diagram on figure 2.3 serves as the framework for the following section, illustrating the main processes which are occurring on a photon matter interaction stage.

One process which is of particular interest for the photoacoustic effect considers movement and collision with other molecules. Energy is released by motion of molecules, giving at the same time rise to heating of tissue. In this case, the energy of the photon is converted into kinetic energy, thus removing the photon's contribution to electromagnetic radiation. Since no photon is released, relaxation of molecules is taking place in a *non radiative* nature. In optoacoustics, local temperature gradients within tissue are detected; therefore, *non radiative relaxation* makes up the main contrast in optoacoustic imaging.

Another scenario assumes energy relaxation in form of *luminescence*, in particular *photoluminescence* for the case of photon absorption. *Luminescence* describes the relaxation of electrons from the excited state to the ground state, generating a photon matching the quantum energy. *Luminescence* can further be classified into *fluorescence* and *phosphorescence* according to the life time of stimulated electrons. Life time covers the time period from excitation of molecules or atoms by photon absorption to the time point of energy release.
Consider *fluorescence* with a life time of $\sim$ 1 ns: After absorption, electrons are shifted to higher energy levels within a time scale of 1 fs and subsequently within ps, the electrons drop to the lowest vibrational energy level. The so called internal conversion (see figure 2.3) is not connected to photon emission but vibrational energy conversion. From the excited vibrational energy level, *fluorescence* in terms of *spontaneous photon emission* takes place with the wavelength of the photon being longer and the frequency and energy, respectively, being lower.
For a longer life time in the order of ms to s, *phosphorescence* is occurring. Instead of a direct photon release from the excited state S_1, *phosphorescence* additionally performs an intersystem crossing of electrons which shifts the electrons to a metastable excited triplet state T_1. In this state, energy is conserved because of the forbidden relaxation to the ground state and released under certain conditions. Since *spontaneous photon emission* is forbidden and unfavored in this particular quantum energy state, the time scale for *phosphorescence* is relatively high as opposed to *fluorescence* [125].

For the purpose of completeness, *Raman scattering* as a form of *inelastic scattering* is shortly described. Figure 2.3 briefly illustrates the energy diagram for the *Raman scattering* process. As opposed to *elastic scattering*, *Raman scattering* involves energy conversion between photons and interacting molecules. In *Raman scattering*, the photon excites molecules to a virtual state with relaxation to the ground state in form of photon emission.
On the other hand, *elastic scattering* does not consider energy exchange between photon and molecule. The matter-interacting photons remain part of the radiation field, changing only the propagation direction.

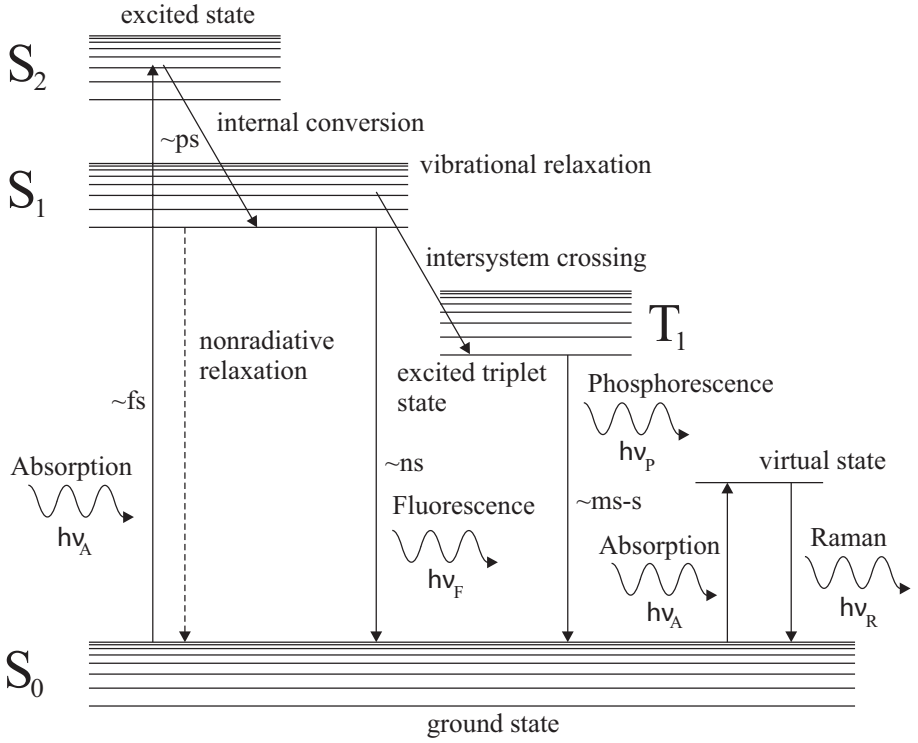

Figure 2.3: Various energy transfer mechanisms following absorption of a photon on the basis of a Jablonski diagram (adapted from [125])

2.3 The photoacoustic effect

The photoacoustic effect is defined by several subsequent processes as depicted in illustration 2.4. Electromagnetic radiation of time varying nature illuminates a region of interest in biological tissue. The target absorbs the energy and heats up because of non radiative relaxation of the tissue. Due to thermoelastic expansion, the temperature gradient is converted into mechanical stress. Induced stress waves are propagating as acoustic pressure

waves in the biological tissue and can be detected with a pressure detector which is coupled to the target by means of an ultrasonic coupling medium like water. Note that the

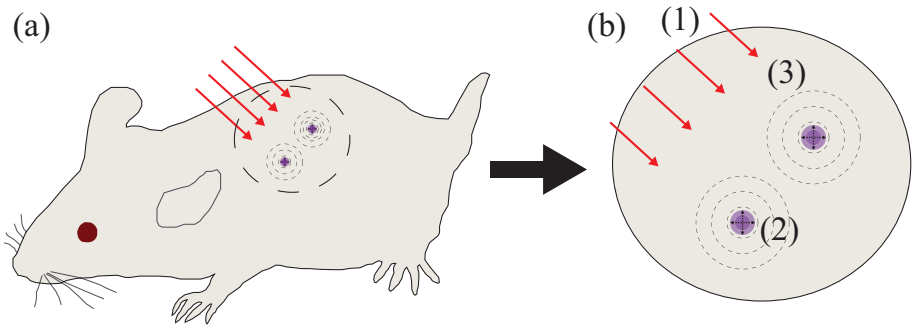

Figure 2.4: Illustration of the photoacoustic effect: (a) Illumination of a region of interest (dashed circle) within biological tissue (e.g. a mouse); (b) ROI from (a): (1) illumination with a time varying electromagnetic source; (2) absorption of electromagnetic energy; (3) induction of mechanical (acoustic) pressure waves following thermoelastic expansion of tissue (dashed lines)

source of electromagnetic radiation has to be of time varying origin since the amplitude of acoustic pressure is dependent on the gradient of the heat source term as will be explained later. Also, the excitation pattern determines the shape of the generated acoustic waves. Therefore, the following sections give a review on the photoacoustic wave equation in its general form before proceeding more specifically to the physics of optoacoustics and thermoacoustics.

2.3.1 General photoacoustic wave equation

2.3.1.1 Photoacoustic wave equation - time domain approach

This section reviews the photoacoustic wave equation in its general form in the time domain.

Generally speaking, the photoacoustic effect can be described by the thermal expansion equation which is a derivative of the generalized Hooke's law and the equation of motion which is deduced from Netwon's second law [125]

$$\nabla \cdot \vec{w}(\vec{r},t) = -\kappa p(\vec{r},t) + \beta T(\vec{r},t) \tag{2.1}$$

$$\rho \frac{\partial^2}{\partial t^2} \vec{w}(\vec{r},t) = -\nabla p(\vec{r},t) \tag{2.2}$$

with the thermal coefficient of cubic expansion β, the pressure p induced at position $\vec{r}$ and time t, the spatial displacement vector $\vec{w}$, the temperature rise T, the mass density ρ and

the isothermal compressibility

$$\kappa = \frac{C_P}{\rho v_s^2 C_V}. \tag{2.3}$$

Herein, v_s indicate the speed of sound in water and C_V and C_p the specific heat capacity for constant volume and pressure, respectively.
The first derivative of the particle displacement vector, equivalent to the particle velocity

$$v_p = \frac{\partial \vec{w}(\vec{r},t)}{\partial t}, \tag{2.4}$$

rearranges basic equations 2.1 and 2.2 to

$$\rho \frac{\partial v_p}{\partial t} = -\nabla p, \tag{2.5}$$

yielding the general form of the photoacoustic wave equation [125]

$$\left(\nabla^2 - \frac{1}{v_s^2}\frac{\partial^2}{\partial t^2}\right) p(\vec{r},t) = -\frac{\beta}{\kappa v_s^2}\frac{\partial^2 T(\vec{r},t)}{\partial t^2}. \tag{2.6}$$

The general form relates the acoustic wave propagation to EM stimulation and specific tissue properties. The right side of equation 2.6 can be furthermore described by the heat diffusion equation

$$\frac{1}{\alpha}\frac{\partial T(\vec{r},t)}{\partial t} - \nabla^2 T(\vec{r},t) = \frac{1}{k} H(\vec{r},t) \tag{2.7}$$

which delineates the spatial distribution of heat H over time t; herein, $\alpha = k(\rho C_V)^{-1}$ represents the thermal diffusivity with the thermal conductivity k. Furthermore, the heating function $H(\vec{r},t)$ characterizes an external spatially dependent temperature input, varying in time.

The time derivative of equation 2.7 with simultaneous solution for the temperature yields

$$\frac{\partial^2 T(\vec{r},t)}{\partial t^2} = \frac{\partial}{\partial t}\left[\alpha \nabla^2 T(\vec{r},t) + \frac{1}{\rho C_V} H(\vec{r},t)\right]. \tag{2.8}$$

The hyperbolic partial differential equation 2.6 can be solved with the Green function, resulting in equation

$$\begin{aligned} p(\vec{r},t) &= \frac{\beta}{4\pi\kappa v_s^2}\int_V \frac{\delta\left(t' - \left(t - \frac{|\vec{r}-\vec{r}'|}{v_s}\right)\right)}{|\vec{r}-\vec{r}'|}\frac{\partial^2 T(\vec{r}',t')}{\partial t'^2} d^3\vec{r}' \\ &= \frac{\beta}{4\pi\kappa v_s^2}\int_V \frac{1}{|\vec{r}-\vec{r}'|}\frac{\partial^2 T\left(\vec{r}', t' = (t - \frac{|\vec{r}-\vec{r}'|}{v_s})\right)}{\partial t'^2} d^3\vec{r}'. \end{aligned} \tag{2.9}$$

Substituting equation 2.8 in 2.9 results in

$$p(\vec{r},t) = \frac{\beta}{4\pi C_p} \int_V \frac{1}{|\vec{r}-\vec{r}'|} \frac{\partial}{\partial t} \left[k\nabla^2 T(\vec{r}',t) + H(\vec{r}',t) \right] d^3\vec{r}'. \tag{2.10}$$

The forward solution to the general wave equation describes the pressure at location $\vec{r}$ and time t, dependent on the first time derivative of the spatial heat diffusion and the heating function. This is the basic equation to determine the pressure distribution within a certain range, determined by time t and position $\vec{r}$ and independent of thermal and stress confinement.

2.3.1.2 Photoacoustic wave equation - frequency domain approach

In frequency domain (TD: $p(\vec{r},t) \rightarrow$ FD: $\hat{p}(\vec{r},\omega)$), the wave equation 2.6 becomes the Helmholtz equation [123]

$$\left(\nabla^2 + \frac{\omega^2}{v_s^2} \right) \hat{p}\,(\vec{r},\omega) = -j\omega \frac{\beta}{C_P} \left(\hat{u}(\vec{r},\omega) \right) \tag{2.11}$$

with the source function

$$\hat{u}(\vec{r},\omega) = k\nabla^2 \hat{T}(\vec{r},\omega) + \hat{H}(\vec{r},\omega). \tag{2.12}$$

Similar to the time domain, the forward solution in frequency domain results in

$$\hat{p}(\vec{r},\omega) = -\frac{j\omega\beta}{4\pi C_p} \int_V \frac{1}{|\vec{r}-\vec{r}'|} \hat{u}(\vec{r},\omega) \exp\left(jk \left| \vec{r}-\vec{r}' \right| \right) d^3\vec{r}'. \tag{2.13}$$

2.3.2 Physics of optoacoustics

Optoacoustics relates to the generation of acoustic pressure waves in response to optical absorption. Two important aspects will be addressed in what follows. First, the propagation of photons in a turbid medium like soft tissue will be explained based on the diffusion equation. Second, the absorption of light which defines the contrast in optoacoustics will be described. Therefore, the spectral behavior of intrinsical absorbers in biological tissue as well as one extrinsical agent is presented at the end of this paragraph.

2.3.2.1 Photon propagation in biological tissue

Propagation of photons in biological tissue is diffusive due to its strong scattering nature. In the optical window, a photon can travel an average length of 100 µm without particle interaction. This is referred to as the mean free path [84]. In the diffusive regime which describes the condition of many photon scattering events with highly diffusive photon distribution, the reduced scattering coefficient can be expressed as

$$\mu_s' = \mu_s(1-g) \tag{2.14}$$

with the dimensionless anisotropy g and the scattering coefficient μ_s. The photon transport in turbid media can be approximated by the diffusion equation according to Haskell et al. [46]

$$\left(\frac{\partial}{c\partial t} + \mu_a - \nabla\cdot[D\nabla]\right)\Phi(\vec{r},t) = S(\vec{r},t) \tag{2.15}$$

with the fluence rate Φ, the source term S, the spatially dependent diffusion coefficient

$$D = \frac{1}{3(\mu_a+\mu_s')} \tag{2.16}$$

and the effective optical absorption coefficient

$$\mu_{eff} = \sqrt{\frac{\mu_a}{D}} = \sqrt{3\mu_a(\mu_a+\mu_s')}. \tag{2.17}$$

In the condition of uniform illumination of the region of interest, the fluence in dependence of the distance from the surface can be calculated according to Beer's law with [124]

$$\Phi(r) = \frac{\Phi(r_0)}{4\pi D r}\exp(-\mu_{eff}r). \tag{2.18}$$

We observe that the fluence is depending on both the reduced scattering coefficient μ_s' and the absorption coefficient μ_a of the tissue.

2.3.2.2 Optoacoustics - sources of optical contrast

Contrast in optoacoustics is originating from optical absorbers in biological tissue. Typical intrinsic absorbers are comprised of e.g. hemoglobin in its oxy- and deoxygenated states and melanin. Referring to the absorption spectrum of water across a broad range of the electromagnetic spectrum as shown in figure 2.5, an optical window which is located at $\sim$ 700 - 900 nm [129] allows for low absorption of water with simultaneous deep

tissue penetration of light. Moreover, Hb and HbO_2 exhibit high absorption of light, thus providing excellent intrinsic contrast agents. The absorption spectrum of the latter two is plotted as a function of the molar extinction coefficient over the wavelength in the visible region in figure 2.6. The region starting from 600 nm to 900 nm is of particular interest since hemoglobin provides maximum difference between its oxy and deoxy state at the wavelength 650 nm and a minimum at the isosbestic point which is located at 800 nm. A multispectral approach which implies imaging at several wavelengths can be used to spectrally differentiate between oxygenated and deoxygenated hemoglobin after spectral unmixing. This idea was developed and implemented at the IBMI and is especially useful for molecular [87] and functional imaging [16].

Additionally, figure 2.7 plots the molar extinction coefficient of Indocyanine Green (ICG) along with oxy and deoxygenated hemoglobin. The exogenous contrast agent provides higher optical absorption within the shown spectrum and exhibits an absorption peak at $\lambda \approx 800$ nm.

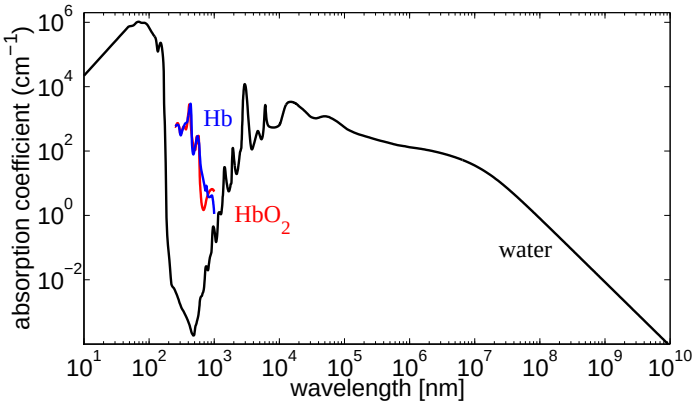

Figure 2.5: Absorption spectrum of water, oxygenated and deoxygenated hemoglobin (data from [94] and [113])

2.3.3 Physics of thermoacoustics

Contrast in thermoacoustics can be attributed to the RF properties of biological tissue. Contrary to optical imaging where scattering in tissue is very strong, scattering plays a minor role in RF imaging [129]. The following section is based on the Maxwell equations as described in 'Microwave Engineering' by Pozar [93], 'Principles of Optics' by Max Born [8] and 'Electromagnetic Waves and Antennas' by Orfanidis [91]. It aims at presenting the basics of electromagnetic wave propagation both in free space and lossy media

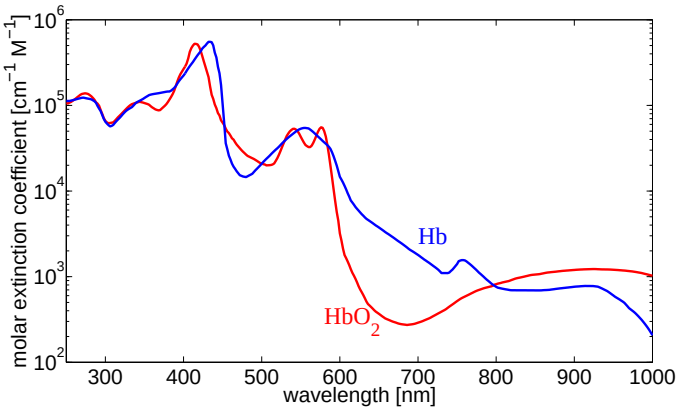

Figure 2.6: Oxygenated and deoxygenated hemoglobin with their molar extinction coefficients [$M^{-1}cm^{-1}$] over wavelength [nm] (data from [94])

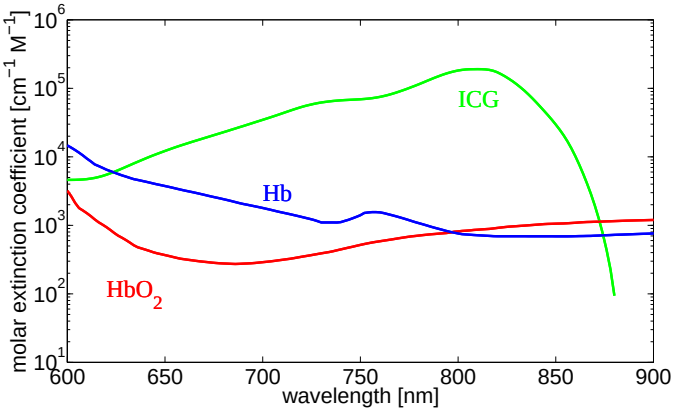

Figure 2.7: ICG, oxygenated and deoxygenated hemoglobin with their molar extinction coefficient [$M^{-1}cm^{-1}$] over wavelength [nm] (data from [72] and [94])

which should be regarded as a reference for the following chapters. At the end, contrast mechanisms along with the sources of RF-contrast for the electric and magnetic case are discussed.

2.3.3.1 Electromagnetic waves in free space

Electromagnetic wave propagation can be modeled by finding a solution to the Maxwell equations. These powerful equations describe in 4 formulas the interaction of time varying electric fields with magnetic fields. The differential form of Maxwell equations is given by

$$\nabla \times \vec{E}(t) = -\frac{\partial \vec{B}(t)}{\partial t} - \vec{M}(t) \tag{2.19}$$

$$\nabla \times \vec{H}(t) = \frac{\partial \vec{D}(t)}{\partial t} + \vec{J}(t) \tag{2.20}$$

$$\nabla \cdot \vec{D}(t) = \rho(t) \tag{2.21}$$

$$\nabla \cdot \vec{B}(t) = 0 \tag{2.22}$$

with the following quantities [93]:

$\vec{E}(t)$ electric field intensity [V m^{-1}],

$\vec{H}(t)$ magnetic field intensity [A m^{-1}],

$\vec{D}(t)$ electric flux density [A s m^{-2}],

$\vec{B}(t)$ magnetic flux density [V s m^{-2}],

$\vec{M}(t)$ (fictitious) magnetic current density [V m^{-2}],

$\vec{J}(t)$ electric current density [A m^{-2}],

$\rho(t)$ electric charge density [A s m^{-3}].

Maxwell's equations represent a summary of the Maxwell-Faraday law 2.19, Ampere's Circuit law 2.20 and Gauss law both for the electric flux theorem 2.21 and the magnetic case 2.22 [91].
The time dependent terms can be simplified with the relationship

$$\vec{E}(\vec{r},t) = Re\left[\vec{E}(\vec{r},\omega)e^{j\omega t}\right], \tag{2.23}$$

resulting in the frequency domain representation or phasor form of the Maxwell equations

$$\nabla \times \vec{E}(\omega) = -j\omega\vec{B}(\omega) - \vec{M}(\omega) \tag{2.24}$$

$$\nabla \times \vec{H}(\omega) = j\omega\vec{D}(\omega) + \vec{J}(\omega) \tag{2.25}$$

$$\nabla \cdot \vec{D}(\omega) = \rho(\omega) \tag{2.26}$$

$$\nabla \cdot \vec{B}(\omega) = 0. \tag{2.27}$$

It has to be noted that the sources of the electromagnetic field are defined by the current $\vec{J}$ and the charge density ρ. The magnetic current $\vec{M}$ is only fictitious since existence of magnetic charges have never been proven [93]. However, for the completeness the magnetic source term is mentioned.
The field intensities are connected with the flux density with the simple relationship

$$\vec{D} = \varepsilon_0\vec{E} \tag{2.28}$$

$$\vec{B} = \varepsilon_0 \vec{H}. \tag{2.29}$$

Equations 2.28 and 2.29 are valid for free-space conditions with the vacuum permeability $\mu_0 = 4\pi \times 10^{-7}$ V s A^{-1} m^{-1} and the vacuum permittivity $\varepsilon_0 = 8.854 \times 10^{-12}$ A s V^{-1} m^{-1}.

2.3.3.2 Electromagnetic waves in material media

So far, electromagnetic wave propagation has been confined to free space conditions. Propagation of electromagnetic waves in matter, e.g. biological tissue, requires the so called material equations which have to be added to the free field form of the Maxwell equations.
With regard to the magnetic and electric flux density, two types of materials have to be distinguished, the first one representing dielectric materials and the second one magnetic materials. Note that the material equations are only discussed for the isotropic case. For the more complex version of anisotropic materials where the polarization and the electric field are direction dependent, a special tensor matrix has to be taken into account.

Considering electromagnetic wave propagation in dielectric material, atoms or molecules undergo a polarization process due to an applied electric field $\vec{E}$. This causes increased electric dipole moments which accordingly result in an additional term to the electric flux $\vec{D}$ represented by the time dependent polarization vector $\vec{P}_{el}$

$$\vec{P}_{el} = \varepsilon_0 \chi_{el} \vec{E} \tag{2.30}$$

$$\vec{D} = \varepsilon_0 \vec{E} + \vec{P}_{el}. \tag{2.31}$$

Herein, χ_{el} represents the electric susceptibility. Substituting equation 2.31 with 2.30 yields

$$\vec{D} = \varepsilon_0 \vec{E} + \vec{P}_{el} = \varepsilon_0 (1 + \chi_{el}) \vec{E} = \varepsilon \vec{E} \tag{2.32}$$

with the complex permittivity ε as a product of the vacuum permittivity ε_0 and the relative permittivity ε_r

$$\varepsilon = \varepsilon_0 (1 + \chi_{el}) = \varepsilon_0 \varepsilon_r = \varepsilon' - j\varepsilon'' \tag{2.33}$$

which are assigned to the medium's properties. ε consists of a real part ε' and imaginary part ε''. The electromagnetic losses can be attributed to the imaginary component, resulting in heat release because of vibrational motion of atom or molecule dipoles [93].

Other than the damping losses, another form of dielectric losses can be attributed to conductivity losses due to free charges which cause a conduction current. The ohmic law

$$\vec{J} = \sigma \vec{E} \tag{2.34}$$

describes a current density in tissue with conductivity σ.

In the other similar case of materials which exhibit magnetic properties, magnetic polarization is occurring due to aligning of magnetic moments to the applied magnetic field. Accordingly, the magnetic flux density is affected by the polarization of the magnetic material

$$\vec{P}_{mag} = \chi_{mag} \vec{H}_{mag} \tag{2.35}$$

$$\vec{B} = \mu_0 \left(\vec{H}_{mag} + \vec{P}_{mag} \right) \tag{2.36}$$

with the complex magnetic susceptibility χ_{mag}.
Equation 2.35 with equation 2.36 yields

$$\vec{B} = \mu_0 \left(1 + \chi_{mag}\right) \vec{H}_{mag} = \mu \vec{H}_{mag} \tag{2.37}$$

with the complex permeability

$$\mu = \mu_0 (1 + \chi_{mag}) = \mu_0 \mu_r = \mu' - j\mu'', \tag{2.38}$$

where μ_r denotes the relative permeability, μ' the real part and μ'' the imaginary part which is responsible for magnetic losses.

2.3.3.3 Propagation of waves in lossy media

The derived Maxwell equations from the preceding section provide the necessary tools to calculate the electromagnetic losses that appear in matter. Again, the holistic approach is discussed in Pozar [93]. In conductive material with the conductivity σ, the Maxwell-Faraday equation in addition to Ampère's law can be rewritten in the form

$$\nabla \times \vec{E} = -j\omega\mu \vec{H} \tag{2.39}$$

$$\nabla \times \vec{H} = j\omega\varepsilon \vec{E} + \sigma \vec{E}. \tag{2.40}$$

Substituting equation 2.40 into 2.39 yields

$$\nabla^2 \vec{E} + \omega^2 \mu \varepsilon \left(1 - j\frac{\sigma}{\omega\varepsilon}\right) \vec{E} = 0, \tag{2.41}$$

which is equivalent to the wave equation or Helmholtz equation in lossy tissue. The wavenumber in the lossless case is given by

$$k = \omega\sqrt{\mu\varepsilon}, \tag{2.42}$$

however, in our case where losses have to be taken into account, the propagation constant k is modified to

$$k = \omega\sqrt{\mu\varepsilon\left(1 - j\frac{\sigma}{\omega\varepsilon}\right)}. \tag{2.43}$$

Furthermore, the attenuation coefficient α and the phase velocity β can be summarized in the complex propagation constant γ

$$\gamma = \alpha + j\beta = j\omega\sqrt{\mu\varepsilon}\sqrt{1 - j\frac{\sigma}{\omega\varepsilon}}. \tag{2.44}$$

Solving the equation for α and β yields the decay rate and the phase of the attenuated traveling wave

$$\alpha = \omega\sqrt{\frac{\mu\varepsilon}{2}\left(\sqrt{1 + \left(\frac{\sigma}{\omega\varepsilon}\right)^2} - 1\right)} \tag{2.45}$$

$$\beta = \omega\sqrt{\frac{\mu\varepsilon}{2}\left(\sqrt{1 + \left(\frac{\sigma}{\omega\varepsilon}\right)^2} + 1\right)}. \tag{2.46}$$

One possible solution to the wave equation 2.41 with one field component in x-direction and propagation in z-direction reduces the Helmholtz equation to

$$E_x(z) = E_{0x}^{+} e^{-jkz} + E_{0x}^{-} e^{+jkz}. \tag{2.47}$$

In time domain, the propagating electric field can be rewritten in the form

$$\begin{aligned} E_x(t) &= Re\left\{\left(E_{0x}^{+} e^{-\gamma z} + E_{0x}^{+} e^{+\gamma z}\right) e^{j\omega t}\right\} \\ &= |E_{0x}^{+}| e^{-\alpha z} cos(\omega t - \beta z) + |E_{0x}^{-}| e^{+\alpha z} cos(\omega t + \beta z). \end{aligned} \tag{2.48}$$

Taking only the positive traveling wave (E_{0x}^{+}) with the propagation factor

$$e^{-\gamma z} = e^{-\alpha z} e^{-j\beta z} = e^{-\alpha z}\cos(\omega t - \beta z) \tag{2.49}$$

into account, we see the exponential decay of the wave with the damping or attenuation factor α, given in [dB] or [Np]. Thus, the penetration depth D_P is the inverse of the attenuation factor according to

$$E(z) = E_0 e^{-\alpha z} \tag{2.50}$$

$$\alpha z = -\ln \frac{E(z)}{E_0} \tag{2.51}$$

$$D_P = \frac{1}{\alpha} \tag{2.52}$$

with the electric field at the surface E_0.

The holistic derivation of power and energy equations for electromagnetic waves can be consulted in the book 'Microwave Engineering' [93], however, the basic equations for power transfer and losses through dissipation will be presented briefly for completeness. The underlying doctrine is Poynting's theorem for the non-static case where the electric field and the magnetic field are coupled. Without any further derivation, the Poynting theorem can be expressed as

$$\begin{aligned} P_S &= -\frac{1}{2}\int_V \left(\vec{E}\cdot\vec{J_s}^* + \vec{H}^*\cdot\vec{M}_s\right) dv \\ &= \frac{1}{2}\oint_S \vec{E}\times\vec{H}^*\cdot d\vec{s} + \frac{\sigma}{2}\int_V |\vec{E}|^2 dv + \frac{\omega}{2}\int_V \left(\varepsilon''|\vec{E}|^2 + \mu''|\vec{H}|^2\right) dv \\ &+ j\frac{\omega}{2}\int_V \left(\mu'|\vec{H}|^2 - \varepsilon'|\vec{E}|^2\right) dv \end{aligned} \tag{2.53}$$

with the electric source current $\vec{J_s}$ and the magnetic source current $\vec{M}_s$. The last integral in equation 2.53 represents the real part of the permeability and permittivity, thus accounting for the stored energy in the field.
Poynting's theorem describes a power balance with the source terms defined by the first integral in equation 2.53. The second integral accounts for the outgoing power of a system (e.g. matter) defined by the surface area S.
We are interested in the conductive, dielectric and magnetic losses which can be compiled to the form

$$P_{loss}(\omega) = \frac{\sigma}{2}\int_V \left|\vec{E}(\omega)\right|^2 d^3r + \frac{\omega}{2}\int_V \varepsilon'' \left|\vec{E}(\omega)\right|^2 d^3r + \frac{\omega}{2}\int_V \mu'' \left|\vec{H}_{mag}(\omega)\right|^2 d^3r. \tag{2.54}$$

Summarizing the first term as the conductivity losses P_{cond}, the second term as the dielectric losses P_{diel} and the last term as the magnetic losses P_{mag}, equation 2.54 can be

rewritten in the general form

$$P_{loss}(\omega) = P_{cond}(\omega) + P_{diel}(\omega) + P_{mag}(\omega). \tag{2.55}$$

Equation 2.55 is referred to as Joule's law which will be used to determine the sources of RF contrast in thermoacoustic imaging.

2.3.3.4 Thermoacoustics - Sources of dielectric contrast

Contrast in thermoacoustics with RF excitation is defined by the electric properties of tissue, more precisely by the complex permittivity ε'' and conductivity σ. Considering a dominating electric field component and furthermore taking into account that the magnetic permeability of free space and biological tissue are almost equal [112], the overall losses in a time varying electromagnetic field as given in equation 2.54 can be reduced to

$$P_{loss}(\omega) = \frac{\sigma}{2}\int_V \left|\vec{E}(\omega)\right|^2 dr^3 + \frac{\omega}{2}\int_V \varepsilon'' \left|\vec{E}(\omega)\right|^2 dr^3. \tag{2.56}$$

Detailed data on the spectrum of the frequency dependent dielectric properties of various soft tissues can be found in Gabriel et al. [35], [36] and Foster et al. [34].
Additionally, the experimental data can also be approximated with a parametric model based on the Debye equation [112], [33]. This has the advantage of generating a prediction model for different dielectric matters. In what follows, two models will shortly be presented. The second model was then used to calculate the approximate frequency dependent dielectric properties of assorted tissues.

Referring to the first method, Hurt [49] developed a parametric fit to experimental data employing the Debye equation

$$\varepsilon(\omega) = \varepsilon_\infty + \frac{\sigma_0}{j\omega\varepsilon_0} + \sum_{i=1}^{n} \frac{\Delta\varepsilon_i}{1 + j(\omega\tau_i)} \tag{2.57}$$

with the static ionic conductivity σ_0, the permittivity ε_∞ for frequencies $\omega\tau \gg 1$, the dispersion magnitude $\Delta\varepsilon = \varepsilon_s - \varepsilon_\infty$ with the static permittivity ε_s for frequencies $\omega\tau \ll 1$. In [49], the spectrum of muscle tissue was modeled according to the above equation using 5 Debye dispersions, being as accurate as 20% to the experimental data.

To overcome the discrepancy with the objective of a more accurate data fit, Gabriel et al. [37] proposed a modified approach to the Debye equation by taking a so called

distribution parameter α_{par} into account. The additional parameter introduces a quantity for the dispersion broadening, thus resulting in equation

$$\varepsilon(\omega) = \varepsilon_\infty + \frac{\sigma_0}{j\omega\varepsilon_0} + \frac{\Delta\varepsilon}{1 + j(\omega\tau)^{1-\alpha_{par}}}. \tag{2.58}$$

The correlating spectrum can then be modeled with the multiple Cole-Cole approach

$$\varepsilon(\omega) = \varepsilon_\infty + \frac{\sigma_0}{j\omega\varepsilon_0} + \sum_{i=1}^{n} \frac{\Delta\varepsilon_i}{1 + j(\omega\tau_i)^{(1-\alpha_{par,i})}} \tag{2.59}$$

by selecting tissue-specific parameters in the expected frequency range.

Figure 2.8 plots the parametric result for the conductivity and permittivity for various tissues in the frequency range from 10 Hz to 100 GHz calculated with the parametric model from equation 2.59. Values are taken from Gabriel et al. [37] and are shown in table A.1 in the appendix A.

To get an idea of different dielectric tissue properties, muscle tissue has a conductivity of $\sigma = 0.7$ S m^{-1} at 100 MHz whereas fatty tissue exhibits a conductivity of $\sigma = 0.05$ S m^{-1}. In terms of contrast this example proves a 14 times higher absorption from muscle tissue compared to fat tissue. Note that both conductivity and permittivity are changing with frequency.

2.3.3.5 Thermoacoustics - Sources of magnetic contrast

The previous case considered a simplified RF excitation scheme with dominating electric field components, neglecting magnetic losses. Conversely, a dominating magnetic field results in a different contrast which is attributed mainly to magnetic energy losses. The following section reviews the main mechanisms of magnetic heating for the particular application within thermoacoustic signal generation and imaging. A profound overview which served as the framework for this section is given in the books 'Hysteresis in Magnetism' by Giorgio Bertotti [6], 'Magnetism in Medicine' by Wilfried Andrä and Hannes Nowak [2] but also in publications by Hergt et al. [47] and Fannin et al. [31].

Magnetic losses are versatile, however only the losses that are associated with magnetic fluids in addition with induced current in solid materials will be discussed. According to [47], [43], the magnetic losses can be structured into

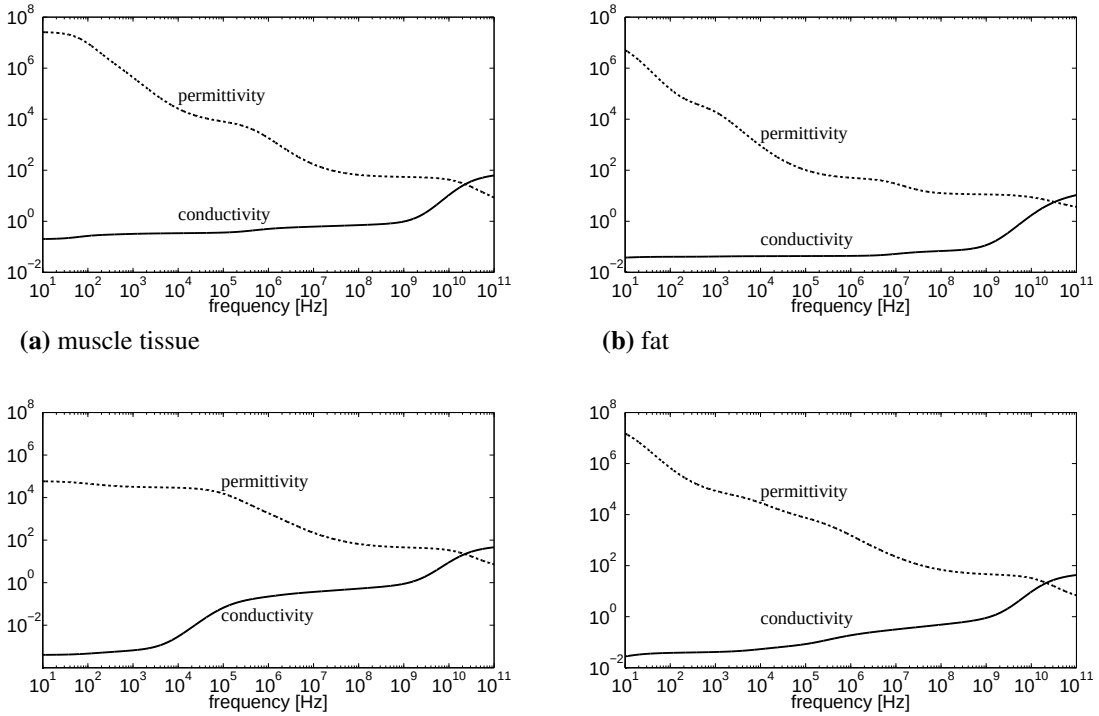

(a) muscle tissue **(b)** fat

(c) skin (wet) **(d)** liver

Figure 2.8: Frequency dependent dielectric properties (dashed lines: permittivity ε, solid lines: conductivity σ) of assorted biological tissue calculated with the parametric model from [37]

- Eddy current losses
- Hysteresis (domain wall motion losses - intrinsic losses)
- Rotational losses in magnetic fluids
- Relaxation losses (e.g. Néel or Brown relaxation losses).

Although eddy currents play a minor role in medical treatments such as invasive hyperthermia [2], the induction of eddy currents in conductive media is shortly discussed with respect to experimental results obtained in chapter 8. However, the majority of biomedical applications, whether based on therapy (e.g. thermal ablation and hyperthermia) or imaging (e.g. magnetic particle imaging [41] or magnetic resonance imaging), is focused on the latter three mechanisms amounting either to relaxation of magnetization of particles or mechanical rotation of particles in a magnetic fluid.

2.3.3.5.1 Eddy current losses

Consider Poynting's theorem given in equation 2.53. Neglecting electric losses, the equa-

tion reduces to the time domain representation

$$-\frac{1}{2}\oint_S \vec{E}\times\vec{H}^* d\vec{s} = \int_V \frac{\vec{J}^2}{\sigma} d^3r + \int_V \frac{\partial \vec{B}}{\partial t}\vec{H} d^3r \tag{2.60}$$

with the electric current density $\vec{J} = \sigma\vec{E}$.
The equation describes a power balance equation with the input (e.g. into the region of interest) on the left side and the stored energy on the right side. The second term on the right hand side represents the hysteresis effects which will be explained in the next paragraph, the first term $\vec{J}^2\sigma^{-1}$ relates to eddy currents. These currents occur in electrically conducting materials as a result from the induction law 2.19. Rewriting the differential form of Faraday's law (induction law) into the integral form yields

$$\oint_S \vec{E} d\vec{l} = -\int\int \frac{\partial \vec{B}}{\partial t}\cdot d\vec{A}. \tag{2.61}$$

Equation 2.61 can be interpreted as circulating electrons in response to a time varying magnetic field. Induced current loops, or simply eddy currents, are dependent on the frequency of the alternating magnetic field and the amplitude of the magnetic field. Eddy currents can be induced both in magnetic and non magnetic materials; the efficiency, however, is depending on the conductivity of the matter. Furthermore, eddy current effects are only present in materials of macroscopic size.
Basically, according to [6], the losses per frequency due to eddy currents can finally be summarized in equation

$$\frac{P}{f} = \int_V \left[\int_0^{f^{-1}} \frac{\left|\vec{J}(\vec{r},t)\right|^2}{\sigma} dt \right] V^{-1} d^3r. \tag{2.62}$$

In biomedical applications, this phenomenon gave rise to eddy current based hyperthermia. However, there are drawbacks to this hyperthermic method. First, eddy current hyperthermia is an invasive therapy method because heat sources, so called thermal seeds, have to be implemented near the tumor for efficient thermal ablation. Second, eddy currents are restricted to materials at macroscopic scale and can not be induced in small particles. This is attributed to the inverse proportionality of heat dissipation efficiency in relation to the size of conducting materials [2]. Thus, the smaller the conducting matter the less-efficient heat dissipation originates from eddy current losses.

2.3.3.5.2 Hysteresis losses

Referring to yet another loss mechanism, hysteresis describes a phenomenon where a quantity X lags behind a quantity Y, or in other words where the output is temporally delayed behind the input [6]. In magnetism, hysteresis more specifically defines the magnetization of materials due to an externally applied magnetic field. The magnetic material is magnetized in one specific direction and will not relax to its equilibrium state when the applied field is removed; hence, it is permanently magnetized.

In alternating magnetic fields, magnetic materials change their magnetization according to the direction of the externally applied magnetic field which results in a hysteresis cycle as shown in figure 2.9. Hysteresis loops can be plotted where either the magnetic flux $\vec{B}$ or the magnetization $\vec{P}_{mag}$ is plotted over the magnetic field strength $\vec{H}$ ($\vec{B}(\vec{H})$ or $\vec{P}_{mag}(\vec{H})$).

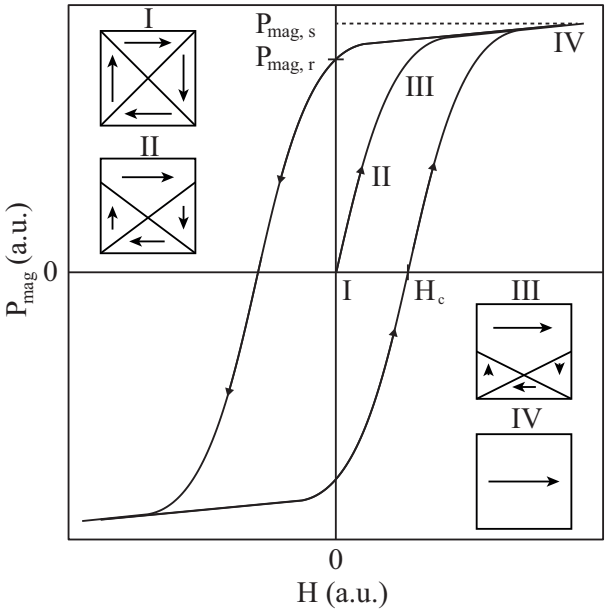

Figure 2.9: Hysteresis loop of a magnetic material exhibiting multiple domains with corresponding domain wall displacements; index c: coercivity, index r: remanence, index s: saturation (adapted from [79])

The phenomenon of hysteresis is related to materials with multiple magnetic subdomains with each of these domains having a magnetization direction. The holistic explanation of multi domain existence is rather complex and not within the scope of the thesis, therefore only the basics which help in understanding the mechanism are explained.

Magnetic domains are separated by so called domain walls (Bloch Walls) as depicted in the insets in figure 2.9. Each domain is characterized by a specific magnetization as illustrated in inset I. In the presence of an external magnetic field, magnetic domains with magnetization in the direction of the applied field are energetically favored over other domains (see inset II and III in figure 2.9). This causes a spatial expansion of the domains

which are equal to the external field vector. Domains which are not aligned to the external field decrease in size. With increasing field strength the size of the energetically favored domains increase until the saturation point results in one single domain dominating the whole material as highlighted in inset IV.

Losses associated with hysteresis are based on domain wall displacements being dissipated as thermal energy. The energy loss can be quantified by the area of the loop described by $P_{mag}(H)$ employing equation [107]

$$E_{hys} = -\mu_0 \oint P_{mag} dH_{mag}. \tag{2.63}$$

Consider an alternating magnetic field

$$H_{mag}(t) = H_{mag,0}\cos(\omega t) = Re\left\{H_{mag,0} exp(j\omega t)\right\} \tag{2.64}$$

and the magnetization M

$$P_{mag}(t) = \chi H_{mag} = H_{mag,0}\left(\chi'_{mag}\cos(\omega t) + \chi''_{mag}\sin(\omega t)\right). \tag{2.65}$$

Thus, equation 2.63 can be calculated as the energy loss per cycle

$$E = 2\mu_0 H^2_{mag,0}\chi''_{mag} \oint_0^{2\pi\omega^{-1}} \sin^2 \omega t dt. \tag{2.66}$$

Solving the integral in equation 2.66 yields the power loss

$$P = fE = \mu_0 \pi \chi''_{mag} f H^2_{mag,0} \tag{2.67}$$

which accounts for dissipation losses due to hysteresis per unit time. Note that the losses are dependent on the material parameters, i.e. imaginary part of the complex magnetic susceptibility χ''_{mag}, magnetic field H_{mag} and the rate of change f.

2.3.3.5.3 Rotational losses

Viscous losses generally refer to heat generation due to frictional motion. As opposed to the previous cases where the material is solid with fixed magnetic domains (hysteresis) and induced loop currents (eddy currents), rotational losses are confined to particles which are suspended in fluids. Exposed to an alternating magnetic field, particles act as small

permanent magnets and are rotated due to a torque moment exerted on the particle

$$T_M = \mu_0 M_R H_{mag} V \tag{2.68}$$

with the remanent magnetization $P_{mag,R}$ [47]. In order to surpass the viscous torque of the fluid, the magnetic field needs to exceed a minimum of

$$H_{mag,min} = 12\pi\eta f \mu_0^{-1} P_{mag,R}^{-1} \tag{2.69}$$

where η is the viscosity.
To get an idea for the required field strength for Fe_3O_4 magnetite particles with $P_{mag,R} = 2.3 \times 10^5$ A m^{-1} suspended in water with a viscosity of $\eta = 1 \times 10^{-3}$ Pa s at frequency f= 100 kHz, the minimum magnetic field for magnetite is calculated to $H_{mag,min} \approx 13$ kHz [2].

Finally, the specific magnetic loss energy can be calculated as

$$W_{mag,rot} = 24\pi^2 \eta f \rho^{-1} \tag{2.70}$$

with the density ρ.

2.3.3.5.4 Relaxation losses

Eddy current losses as well as hysteresis losses are occurring in magnetic materials with dimensions $d_{mag} > 1$ mm [54]. Moving to materials with smaller size on a submillimiter scale, e.g. magnetic micro- or nanoparticles, a fourth type of loss appears which is characterized by relaxation of magnetic particles. Depending on the size of the particle, either Néel or Brown relaxation is the dominating effect. The following paragraph will shortly explain both phenomenons with an outlook why relaxation processes are important for application in thermoacoustic imaging.

A fundamental theorem on the relationship between magnetic particle dimension and magnetic domain was initially postulated by Brown [14] and revisited in 2001 by Aharoni [1]. Briefly, the theorem considers a size dependent single domain particle state which is energetically favorable over the multidomain state. Two spatial thresholds are introduced, one referring to the lower bound which favors one singular magnetic domain and an upper bound which accounts for a non-uniform magnetization with multiple domains within the particle. Therefore, if a particle is small enough so that it exceeds the lower threshold it will behave like a single domain particle. The size of the particle

is of importance for the dominating relaxation mechanism as will be explained in the following.
The considerations are confined to homogeneous particles with an ellipsoidal shape (e.g. spheres) with respect to the unpredictable complexity of irregular shaped particles.

In general, two relaxation mechanisms for the magnetic moment of particles exist. The Brownian relaxation [15] is defined by equation

$$\tau_B = \frac{3\eta V_H}{k_B T} \tag{2.71}$$

with the hydrodynamic volume V_H [107] and the Boltzmann constant k_B. Brownian relaxation describes the motion of entire particles due to an external AC field as depicted in figure 2.10.

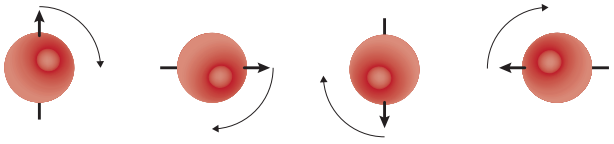

Figure 2.10: Brown relaxation: rotation of the magnetic particle in response to an externally applied magnetic field

The second mechanism was investigated by Néel in 1949 [81]. In contrast to a frictional motion of particles, Néel relaxation accounts for rotation of the magnetic moment within the particle in response to an AC magnetic field. The particle itself is not moving as illustrated in figure 2.11.

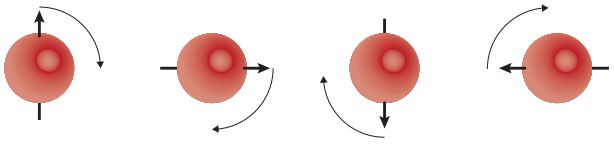

Figure 2.11: Néel relaxation: rotation of the magnetic moment of a magnetic particle in response to an externally applied magnetic field; note the immobility of the particle

According to [107], Néel relaxation is determined by equation

$$\tau_N = \frac{\sqrt{\pi}}{2}\tau_0 \exp(KV_m(k_B T)^{-1})(KV(k_B T)^{-1})^{-1/2} \tag{2.72}$$

with the anisotropy constant K, the magnetic volume $V_m = 4\pi R_p^3/3$, the particle radius R_p, the thermal energy $k_B T$ and the time constant τ_0 which is in the order of 10^{-9} [79].

Consider now a suspension of magnetic particles at different sizes. Depending on different parameters (e.g. particle size, temperature), one of the above mentioned mechanisms is dominating, resulting in an effective relaxation time

$$\tau = \frac{\tau_B \tau_N}{\tau_B + \tau_N}. \tag{2.73}$$

In other words, the faster relaxation time is dominating the relaxation mechanism [47].

In order to estimate the power dissipation losses (equation 2.67) of a magnetic fluid with a distribution of particles at different dimensions, material parameters which are associated with the complex magnetic susceptibility

$$\chi_{mag}(\omega) = \chi'_{mag}(\omega) - j\chi''_{mag}(\omega) \tag{2.74}$$

have to be determined. The complex susceptibility is composed of the in-phase component

$$\chi'_{mag}(\omega) = \frac{\chi_{mag,0}}{1 + (\omega\tau)^2} \tag{2.75}$$

and the out of phase component

$$\chi''_{mag}(\omega) = \frac{\omega\tau\chi_{mag,0}}{1 + (\omega\tau)^2} \tag{2.76}$$

which accounts for magnetic losses. Herein, χ_0 represents the equilibrium susceptibility which is defined as

$$\chi_{mag,0} = \frac{n_p m_p^2}{3k_B T \mu_0} \tag{2.77}$$

where n_p denotes the number density of the magnetic material, $m_p = P_{mag,s} V_m$ is the magnetic moment given by the product of the saturation magnetization $P_{mag,s}$ and the particle volume V_m.

Finally, the power dissipation due to relaxation mechanisms can be calculated with equation

$$P = fE = \mu_0 \pi \chi''_{mag} f H^2_{mag} = \mu_0 \pi \chi_{mag,0} f H^2_{mag} \frac{2\pi f\tau}{1 + (2\pi f\tau)^2}. \tag{2.78}$$

It has to be noted that the relaxation mechanism is highly dependent on particle dimensions. Néel relaxation, for instance, is strongly connected to the size of the particle which causes a narrow peak of maximum power losses.
In the case of Brownian relaxation referring to equation 2.71, the magnetic losses increase with particle size reaching an upper saturation state occurring in high frequent magnetic

fields.

The power losses for low frequent magnetic fields $\omega\tau \ll 1$ are reduced to the frequency independent equation [47]

$$P = \mu_0 \pi \chi_{mag,0} H_{mag}^2 \tau^{-1}. \tag{2.79}$$

Figure 2.12a plots the theoretical complex magnetic susceptibility for a spherical particle, exhibiting a size of 8 nm. Clearly, a maximum of magnetic losses is visible at the point where the imaginary and the real part are crossing. In 2.12b, the effective relaxation time as a function of particle radius is plotted. The curve for time τ_N is dominating for a particle radius < 7 nm and exhibits a steep pitch, corresponding to the narrow peak of maximum power dissipation. On the other hand, Brown relaxation is dominating for a particle radius > 7 nm, characterized by a moderate pitch which relates to the increasing power dissipation occurring in particles of bigger size.

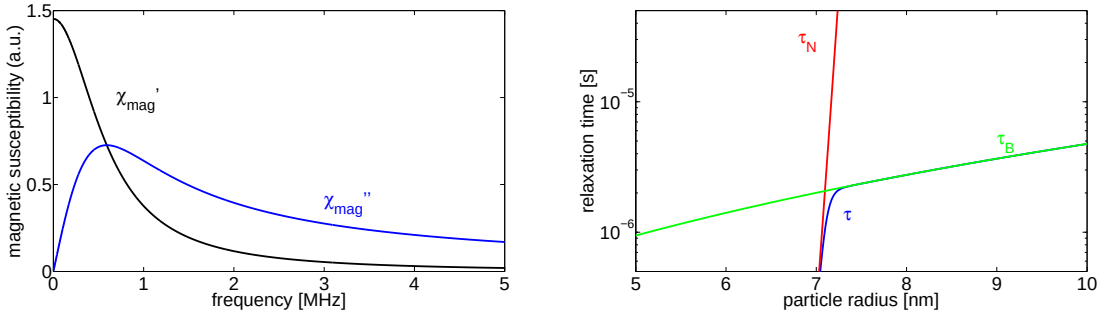

(a) magnetic susceptibility as a function of frequency for particle radius $r = 8$ nm

(b) effective relaxation time τ depending on the particle radius

Figure 2.12: Simulation results for the complex magnetic susceptibility and the effective relaxation time

3 The photoacoustic effect in time and frequency domain

3.1 Introduction

This chapter serves as the introduction towards photoacoustic signal generation in time and frequency domain. Basic properties of the time domain and frequency domain approach were already presented in chapter Introduction 1, therefore the following sections aim at giving an overview based on theoretical considerations.
The chapter starts with a dedicated FDTD simulation tool which is used to solve the photoacoustic wave equation for different excitation patterns. Then, photoacoustics is clustered in several parts. In section 3.3, the time domain method with ideal delta excitation is presented. Following up in section 3.4, a novel thermoacoustic wave stimulation concept is introduced which is settled between time and frequency domain, namely quasi CW thermoacoustics. Advancing to frequency domain, section 3.5 discusses first the excitation with continuous light before completing the chapter with the frequency domain thermoacoustic method, employing frequency modulated low frequent electromagnetic energy to induce acoustic waves.

3.2 Numerical simulation of the photoacoustic wave equation

This section aims at giving a simulation tool for the general photoacoustic wave equation given in equation 2.6. Let us reconsider the formula

$$\left(\nabla^2 - \frac{1}{v_s^2}\frac{\partial^2}{\partial t^2}\right) p(\vec{r},t) = -\frac{\beta}{\kappa v_s^2}\frac{\partial^2}{\partial t^2} T(\vec{r},t) \tag{3.1}$$

with the heat diffusion equation

$$\frac{\partial}{\partial t}T(\vec{r},t) = \left(\alpha\nabla^2 T(\vec{r},t) + \frac{1}{\rho C_V}H(\vec{r},t)\right). \tag{3.2}$$

Eq. 3.2 represents an inhomogeneous wave equation with the heating term $H(\vec{r},t)$. In two dimensions, equation 3.2 can be rewritten as

$$\frac{\partial T(\vec{r},t)}{\partial t} = \alpha\left(\frac{\partial^2 T(\vec{r},t)}{\partial x^2} + \frac{\partial^2 T(\vec{r},t)}{\partial y^2}\right) + (\rho C_V)^{-1}H(\vec{r},t). \tag{3.3}$$

This problem can be approached with diverse solution approaches, e.g. with the finite element method; however, with respect to the easiness of implementation, the two dimensional heat equation is solved numerically with the finite difference method. Based on finite differencing as proposed in the book 'Numerical Techniques in Electromagnetics' from Sadiku [111], the partial differential equation is solved using the implicit approach with the Crank Nicolson Method.

After spatial discretization over the xy space, the heat distribution from equation 3.2 can be rewritten in the implicit form

$$\begin{aligned}\frac{T^{i+1}(m,n)-T^i(m,n)}{\Delta t} =& \frac{\alpha}{2}\left[\frac{T^i(m+1,n)-2T^i(m,n)+T^i(m-1,n)}{(\Delta x)^2}\right.\\ &\left.+\frac{T^{i+1}(m+1,n)-2T^{i+1}(m,n)+T^{i+1}(m-1,n)}{(\Delta x)^2}\right]\\ &+\frac{\alpha}{2}\left[\frac{T^i(m,n+1)-2T^i(m,n)+T^i(m,n-1)}{(\Delta y)^2}\right.\\ &\left.+\frac{T^{i+1}(m,n+1)-2T^{i+1}(m,n)+T^{i+1}(m,n-1)}{(\Delta y)^2}\right]\\ &+(\rho C_V)^{-1}H^i(m,n)\end{aligned} \tag{3.4}$$

where m and n represent the discretization steps in the xy space and furthermore $T^i(m,n)$ and $T^{i+1}(m,n)$ define the temperature at time point i and time point $i+1$ at discretization point (m,n), respectively. Rearranging equation 3.4 according to the time points leads to

$$\begin{aligned}(1+2u)T^{i+1}(m,n) - \frac{u}{2}\left(\Theta^{i+1}\right) =& (1-2u)T^i(m,n) + \frac{u}{2}\left(\Theta^i\right)\\ &+k_c H^i(m,n)\end{aligned} \tag{3.5}$$

with the substitutions

$$\Theta^{i+1} = T^{i+1}(m+1,n) + T^{i+1}(m-1,n) + T^{i+1}(m,n+1) + T^{i+1}(m,n-1) \tag{3.6}$$

$$\Theta^{i} = T^{i}(m+1,n) + T^{i}(m-1,n) + T^{i}(m,n+1) + T^{i}(m,n-1), \tag{3.7}$$

setting $\Delta x = \Delta y$ with $u = \alpha \Delta t (\Delta x)^{-2}$ and $k_c = \Delta t \, (\rho C_V)^{-1}$. Equation 3.5 represents a system of linear equations, thus it can be rewritten in an equivalent Matrix form

$$\mathbf{A} \cdot \mathbf{T}^{i+1} = \mathbf{B} \cdot \mathbf{T}^{i} + \mathbf{b} + k_c \mathbf{H}^{i} \tag{3.8}$$

with the discretization matrix $\mathbf{A}$ at time point $i+1$, the discretization matrix $\mathbf{B}$ at time point i and the boundary vector $\mathbf{b}$ defining the boundary conditions for the FDTD simulation. Through matrix inversion, equation 3.8 can be rewritten to

$$\mathbf{T}^{i+1} = \mathbf{A}^{-1} \cdot (\mathbf{B} \cdot \mathbf{T}^{i} + \mathbf{b} + k_c \mathbf{H}^{i}). \tag{3.9}$$

The latter equation 3.9 describes the temperature distribution in an object depending on *a-priori* boundary conditions $\mathbf{b}$ and the heating function $H(\vec{r},t)$ at time steps Δt.
Substituting the heat term with different heating functions (e.g. a pulsed, CW or quasi CW function) yields the temperature distribution which finally is substituted for each time step into equation 3.1. Thus, the acoustic wave propagation depending on different heating functions can be accurately calculated.

3.3 The photoacoustic effect in time domain

Based on the fundamental principles of time domain photoacoustics given in the introduction 1.2.3, this section starts with a short overview followed by implementation considerations. Additionally, simulation results with the simulation tool presented in the preceding section are presented.

3.3.1 Ideal delta excitation of photoacoustic signals

In a first scenario, the ideal case of delta like excitation is discussed. Fundamentally, two timing factors are decisive for efficient signal generation in time domain photoacoustics ([125], [129]).
The first timing scale, usually referred to as thermal confinement [129], describes the

thermal diffusion of converted EM energy over the heating length L_s depending on the thermal diffusivity α

$$\tau_{th} = \frac{L_s^2}{\alpha}. \tag{3.10}$$

Accordingly, the second condition, commonly termed stress confinement, characterizes the time interval of pressure relaxation over the heating length, given by equation

$$\tau_s = \frac{L_s}{v_s}. \tag{3.11}$$

To get an idea of expected time factors let us first consider a heating length of $L_s = 100$ µm similar to a calculation which was performed in a publication by Xu and Wang [128]. According to Blumm et al [7], the thermal diffusivity of water at $T = 35°\text{C}$ can be approximated to $\alpha \approx 0.145 \times 10^{-6}$ m^2 s^{-1}. This results in a thermal propagation time of $\tau_{th} \approx 70$ ms and a stress propagation time of $\tau_s \approx 70$ ns.
In order to fulfill both the thermal and the stress confinement, the pulse duration of the excitation pulse τ_p has to be shorter than both timing factors for decent acoustic signal generation.

Let us reconsider the heat equation 3.2. In thermal and stress confinement conditions, the heat equation 3.2 can be approximated by

$$\frac{1}{\alpha}\frac{\partial T(\vec{r},t)}{\partial t} = \frac{1}{k}H(\vec{r},t) \tag{3.12}$$

where the spatial diffusion of temperature becomes now negligible. Accordingly, the photoacoustic wave equation 3.1 simplifies to

$$\left(\nabla^2 - \frac{1}{v_s^2}\frac{\partial^2}{\partial t^2}\right) p(\vec{r},t) = -\frac{\beta}{C_p}\frac{\partial H(\vec{r},t)}{\partial t} \tag{3.13}$$

with the time derivative of the heating function expressing the source term.

Since we are dealing with delta like excitation pulses, the heating function can be separated into its spatial and temporal components [102]

$$\frac{\partial H(\vec{r},t)}{\partial t} = H_s(\vec{r})H_t(t) \approx H_s(\vec{r})\delta(t), \tag{3.14}$$

approximating the forward solution to the wave equation 2.10 to the following form

$$p(\vec{r},t) = \frac{\beta}{4\pi C_P}\frac{\partial}{\partial t}\int \frac{H_s(\vec{r}')}{|\vec{r}-\vec{r}'|}\delta\left(t - \frac{|\vec{r}-\vec{r}'|}{v_s}\right) d^3\vec{r}'. \tag{3.15}$$

Equation 3.15 represents the general forward solution to the wave equation that takes into account thermal and stress confinement and delta excitation. The approximation of zero heat conduction is equivalent to an inelastic and therefore irreversible volume expansion due to thermal dissipation (for $\beta > 0$).

3.3.2 Time domain thermoacoustics - a schematic implementation

Figure 3.1 gives a schematic illustration of thermoacoustic signal generation and detection implemented in the time domain. Results from a simple simulation under the assumption of delta like excitation are shown. The acoustic wave detector is at distances d_1 and d_2

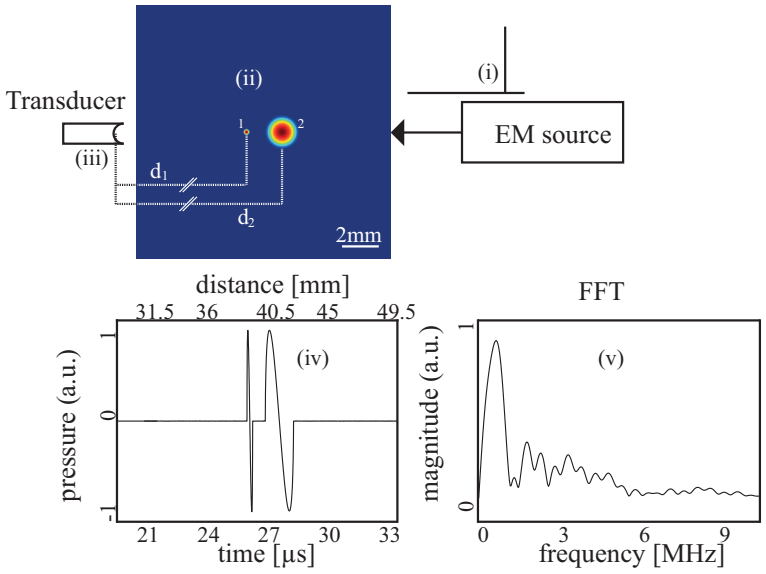

Figure 3.1: Simulation results in time domain thermoacoustics: (i) excitation with delta like pulses; (ii) object 1 ($\varnothing\, 0.4\,mm$) and object 2 ($\varnothing\, 2\,mm$) absorb electromagnetic energy; (iii) transducer detects acoustic pressure waves at time points $t_1 = d_1/v_s$ and $t_2 = d_2/v_s$; (iv) time profile as detected by the ultrasound transducer; (v) FFT of time profile showing the frequency response of the absorbers

from the absorbers which consist of two circular shaped objects (absorber 1: $\varnothing\, 0.4$ mm; absorber 2: $\varnothing\, 2$ mm) with paraboloid absorption profile. The electromagnetic source emits delta-like ultrashort pulses which cause instantaneous heating with subsequent thermoelastic expansion, generating acoustic pressure waves from both absorbers. Data acquisition is triggered at the time point of pulse excitation. The acoustic signals from the first absorber covers a time span of $25.86\ \mu s < t_1 < 26.14\ \mu s$ whereas signal duration from the second absorber lasts from $26.73\ \mu s < t_2 < 28.07\ \mu s$. With the acoustic speed of sound in water, the measured time t_{ab} can be converted into distance from the detector using

equation

$$r = v_s \cdot t_{ab}. \tag{3.16}$$

Thus, the signal duration can be correlated to the size of absorbers. It has to be noted that the acoustic pressure waves in time domain feature bipolar nature with the size of the object defining the spectral components of the acoustic pressure waves. Considering for example small objects, the acoustic response is confined to shorter time, thus resulting in higher frequency components. Vice versa, if large objects are imaged, the acoustic response tends to low frequent components. This has to be taken into account in thermoacoustic experiments when bandwidth limited transducers are used, whereby the detector's frequency response has to be matched to the size of the imaged object.
In a tomographic imaging implementation, either the detector is rotated around the object or the sample is moved in order to collect acoustic signals at multiple projections. The detection system is furthermore synchronized to the trigger event, i.e. the electromagnetic impulse.

3.4 Quasi CW thermoacoustics

3.4.1 Introduction

This section describes an excitation scheme that exhibits features of both pulsed and continuous wave mode. Whereas time domain photoacoustics can be implemented with light and RF/microwave excitation, the so called quasi CW method is confined to thermoacoustic signal generation with a dominating electric field component. In quasi CW operation, a harmonic oscillation which abates after several µs is employed to induce thermoacoustic signals.
The resonance frequency of the excitation is settled within the detection bandwidth of the ultrasonic detector, usually in the low MHz range. Quasi CW can be considered as an intermediate state between pulsed and CW since it offers narrowband excitation but still maintains features of pulsed mode with time confined stimulation and a duty cycle below 0.1%.
Characteristic properties of quasi CW can be summarized as

- narrowband excitation with an exponentially decaying heating function
- thermoacoustic signal stimulation over µs
- low duty cycle 0.1%

- narrowband thermoacoustic response at double excitation frequency
- time of flight measurement

The following section highlights the properties of quasi CW thermoacoustic signal generation and renders simulation results obtained with the simulation tool from section 3.2. Additionally, the double frequency dependency is explained which is a typical characteristic of quasi CW and CW thermoacoustic signal generation.

3.4.2 Quasi CW thermoacoustic signal generation

The quasi CW mode can be defined as an underdamped harmonic oscillation that exponentially decreases over time. A typical implementation with explanations on the acquisition scenario is illustrated in figure 3.2 which presents schematically the operation principle of the quasi CW method. The dimensions and absorption characteristics are alike the ones mentioned in section 3.3.2. A dedicated EM source emits a harmonic oscillation at $f_{quasi\,CW} = 3.5$ MHz which is decaying exponentially and lasting over ~ 10 µs. Two objects are exposed to the electromagnetic field and uptake a portion of the energy, thus resulting in instantaneous heating and subsequent thermal expansion followed by induction of acoustic pressure waves. The generated waves are similar to the excitation profile except that they exhibit a narrowband response at double frequency. An ultrasonic detector which is triggered by the rising edge of the quasi CW oscillation detects the monofrequent sound waves originating from the two absorbers.
The double frequency behavior is highlighted in the fourier transform of the excitation signal shown in inset (ii-b) in figure 3.2 as compared to the thermoacoustic response illustrated in inset (v-b). Whereas the objects are exposed to a resonance at $f_{quasi\,CW}$, the acoustic signal is induced at $f_{tas,quasi\,CW} = 2 \cdot f_{quasi\,CW}$.

To obtain a better understanding of the double frequency behavior let us scrutinize the heating function.
Since we confine the excitation to the RF region of the electromagnetic spectrum, the heating function 2.56 from chapter 2, section 2.3.3.4 has to be taken into account. Although the quasi CW method can also be applied to magnetic fields, thermoacoustics here is restricted to the case of conductive and dielectric contrast. Thus, the heating function can be rewritten as

$$H(\vec{r},t) = \frac{\sigma}{2}\int_V \left|\vec{E}(\vec{r},t)\right|^2 dv + \frac{\partial}{\partial t}\int_V \frac{1}{2}\varepsilon'' \left|\vec{E}(\vec{r},t)\right|^2 dv. \tag{3.17}$$

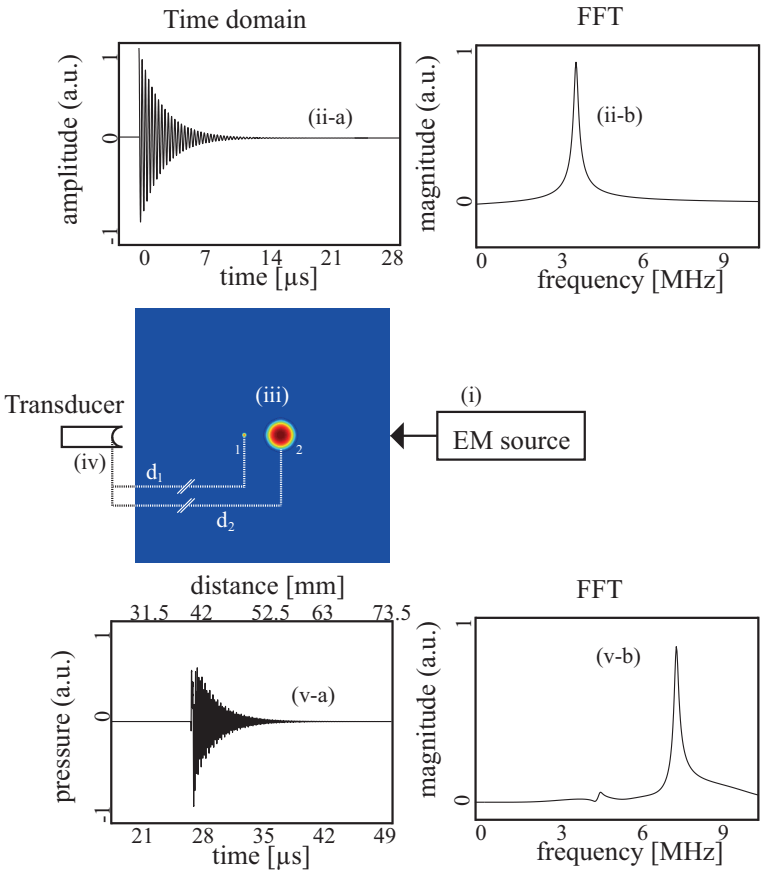

Figure 3.2: Quasi CW thermoacoustic simulation: (i) electromagnetic source with exponentially decaying oscillation profile; (ii-a) excitation signal in time domain; (ii-b) corresponding FFT of (ii-a) with a resonance frequency at $f_{quasi\,CW} = 3.5$ MHz; (iii) absorber 1 ($\varnothing$ 0.4 mm) and absorber 2 ($\varnothing$ 2 mm); (iv) transducer detecting narrowband thermoacoustic signals; (v-a) thermoacoustic response in time domain; (v-b) corresponding FFT of (v-a) with a pronounced peak at $f_{tas,quasi\,CW} = 2 \cdot f_{quasi\,CW}$

The electric field appears as a cosine function with exponential decay. Therefore, the electric field can be approximated by

$$\vec{E}(t) = E_0 \vec{e}_r \exp(-\alpha_D t - \alpha r) \cos(\omega t - \phi_{ph}), \tag{3.18}$$

with the damping coefficient α_D and the phase term ϕ_{ph}. The square of the field can be calculated with the relationship

$$\begin{aligned} \left|\vec{E}(t)\right|^2 =& \vec{E}(t) \cdot \vec{E}(t) \\ =& \vec{e}_r E_0^2 \exp(-2(\alpha_D t + \alpha r)) \frac{1}{2}(1 + \cos(2(\omega t - \phi_{ph}))). \end{aligned} \tag{3.19}$$

Substituting equation 3.19 into 3.17 yields the proportionality

$$H(\vec{r},t) \sim C_g \exp(-2\alpha_D t)\cos(1+2(\omega t-\phi_{ph})) \tag{3.20}$$

with a constant factor C_g. Referring back to equation 2.10, the pressure for quasi CW stimulation can be approximated according to equation

$$p(\vec{r},t) \sim C\int_V \frac{1}{|\vec{r}-\vec{r}'|}\frac{\partial}{\partial t}\left[k\nabla^2 T(\vec{r}',t)+H(\vec{r},t)\right]d^3\vec{r}'. \tag{3.21}$$

The latter equation proves the double frequency dependency of the induced pressure $p(\vec{r},t))$ from the heating function $H(\vec{r},t)$. Note that this relationship is a characteristic feature of thermoacoustic signal generation with electromagnetic field excitation in the low MHz region where the detection elements can be matched to the excitation resonance.
Optoacoustics with CW stimulation does not feature a double frequency dependency but instead a single frequency relationship as will be shown in the next sections where pure CW excitation is discussed, both for the optoacoustic and thermoacoustic case.

3.5 The photoacoustic effect in frequency domain

3.5.1 Introduction

Continuing the transition from time domain to frequency domain photoacoustics, this section aims at giving an overview on pressure signals generated with CW light and RF sources. Simulation results based on the general photoacoustic wave equation from section 3.2 verify an optoacoustic signal which resembles the input modulation, i.e. the modulation frequency of the heating function. Following optical stimulation, CW thermoacoustic signal induction is discussed. Building upon the results from the quasi CW mode, theoretical considerations are completed for CW excitation, showing additionally simulated thermoacoustic signals in response to RF excitation.

3.5.2 Frequency domain optoacoustics

Let us consider an optoacoustic signal generation and detection scenario as depicted in simulation figure 3.3 with two objects of different size (sample 1: $\varnothing$ 0.4 mm, sample 2: $\varnothing$ 2 mm). A laser emits an intensity modulated CW beam with a modulation frequency of

3.5 MHz (see inset (ii-a) and (ii-b) on figure 3.3). Light is absorbed by the objects which gives rise to acoustic pressure waves at distances $d_1 = 38$ mm and $d_2 = 41$ mm from the detector. The absorbers illustrate the temperature profile at one distinct time point of the simulation. An ultrasonic detector (iv) measures acoustic wave signals originating from the absorbers as shown in inset (v-a) and (v-b). Note that the CW acoustic signals start at the position of the first object and are not confined in time. Furthermore, the acoustic response exhibits the same frequency as the modulation signal, thus it resembles a copy of the CW laser beam.

The reason for the single frequency dependence is apparent when we investigate the heating function. In frequency domain optoacoustics, the heating function can be described by equation

$$H(\vec{r},t) = \eta_{th}\frac{\mu_a(\vec{r})}{4\pi D\vec{r}}\exp(-\mu_{eff}\,\vec{r})F(r_0)f_{mod}(t) \tag{3.22}$$

with the conversion factor η_{th} defining the heat conversion efficiency, the diffusion constant D, the effective attenuation coefficient μ_{eff}, the irradiance $F(r_0)$ at the surface of the target and the modulation frequency $f_{mod}(t)$. Assuming cosine like modulation of the CW laser beam, the modulation signal can be represented by

$$f_{mod}(t) = 1 + \cos(2\pi f t). \tag{3.23}$$

Whereas in thermoacoustics the frequency of the electromagnetic field itself is modulated, optoacoustics is characterized by a modulation of the intensity of the laser beam. Thus, in frequency domain optoacoustic imaging the pressure is proportional to the time derivative of the spatial temperature diffusion and the heating function according to equation

$$\begin{aligned} p(\vec{r},t) = \frac{\beta}{4\pi C_p}\int_V \frac{1}{|\vec{r}-\vec{r}'|}\frac{\partial}{\partial t}\big[k\nabla^2 T(\vec{r}',t) \\ + \eta_{th}\frac{\mu_a}{4\pi D\vec{r}}\exp(-\mu_{eff}\vec{r})F(r_0)f_{mod}(t)\big]d^3\vec{r}'. \end{aligned} \tag{3.24}$$

Apparently, the induced optoacoustic pressure is directly dependent on the modulation signal and not on the square. Hence, the optoacoustic signal represents a copy of the intensity coded laser beam.

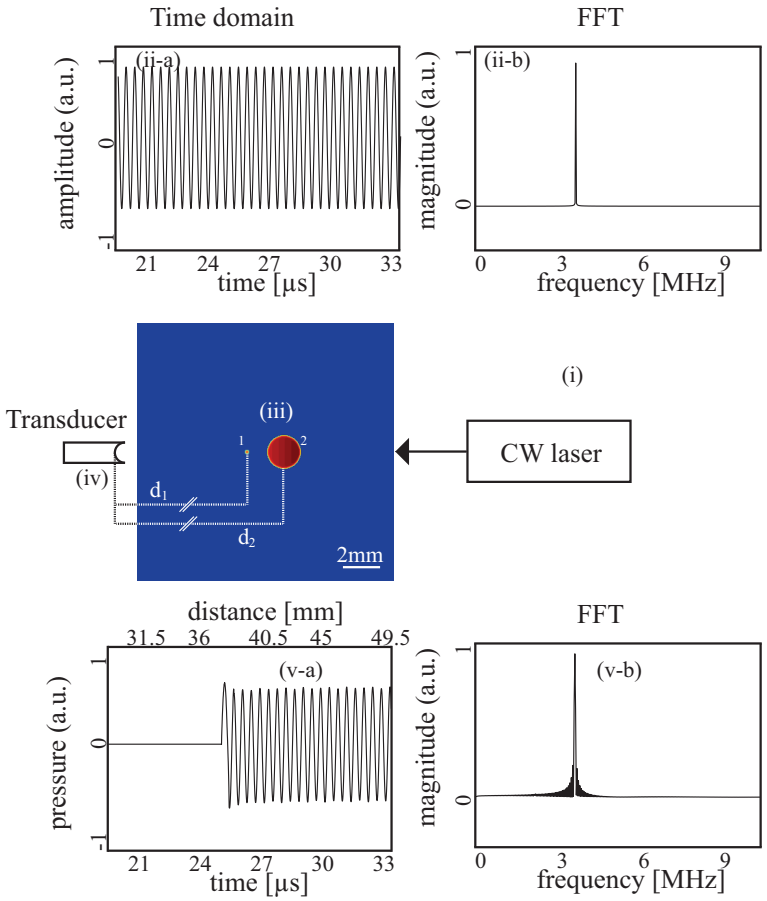

Figure 3.3: Frequency domain optoacoustic simulation scenario: (i) CW laser source emitting a modulated light beam at 3.5 MHz; (ii-a) time domain stimulation profile; (ii-b) corresponding FFT of (ii-a); (iii) optical absorber 1 (⌀ 0.4 mm) and absorber 2 (⌀ 2 mm) in the detection plane; (iv) ultrasound detection unit; (v-a) acoustic response over time; (v-b) corresponding FFT of (v-b) showing $f_{oat} = f_{mod} = 3.5$ MHz

3.5.3 Frequency domain thermoacoustics

Finally, thermoacoustic signals in response to CW excitation at radiowaves are considered in the following section. Recalling the general form of the heating function with the magnetic term results in the time domain expression

$$\begin{aligned} H(\vec{r},t) = \frac{\sigma}{2}\int_V \left|\vec{E}(\vec{r},t)\right|^2 dv + \frac{\partial}{\partial t}\int_V \frac{1}{2}\varepsilon'' \left|\vec{E}(\vec{r},t)\right|^2 dv \\ + \frac{\partial}{\partial t}\int_V \frac{1}{2}\mu'' \left|H(\vec{r},t)\right|^2 dv. \end{aligned} \tag{3.25}$$

Basically, the modulation term can be approximated according to expression

$$A(\vec{r},t) = A_0 \vec{e}_r \exp(-\alpha r)\cos(\omega t - \phi_{ph}) \tag{3.26}$$

where $A(\vec{r},t)$ can be substituted by the electric field quantity $E(\vec{r},t)$ or the magnetic field quantity $H(\vec{r},t)$. The derivation of the double frequency is similar to the quasi CW excitation mode except that the damping term $\exp(-\alpha_D t)$ from equation 3.19 is omitted in formula 3.26.

Simulation results are showcased schematically in illustration 3.4. An electromagnetic source with CW output, exhibiting a modulation frequency of 3.5 MHz, illuminates two objects with sizes similar to the preceding sections. The modulation frequency is shown in inset (ii-a) with the fourier spectrum in inset (ii-b) on figure 3.4. Upon absorption of CW modulated electromagnetic energy, acoustic waves are induced in both absorbers, yielding the thermoacoustic signal shown in inset (v-a) with the corresponding FFT in (v-b). Clearly, the thermoacoustic response to an electric field resonating at 3.5 MHz starts at the position of the first object and resonates at double the frequency $f_{tas,CW} = 2 \cdot f_{CW}$. At the point of intersection (i.e. $t \approx 23.5$ µs), interference of acoustic waves originating from both absorbers can be observed.

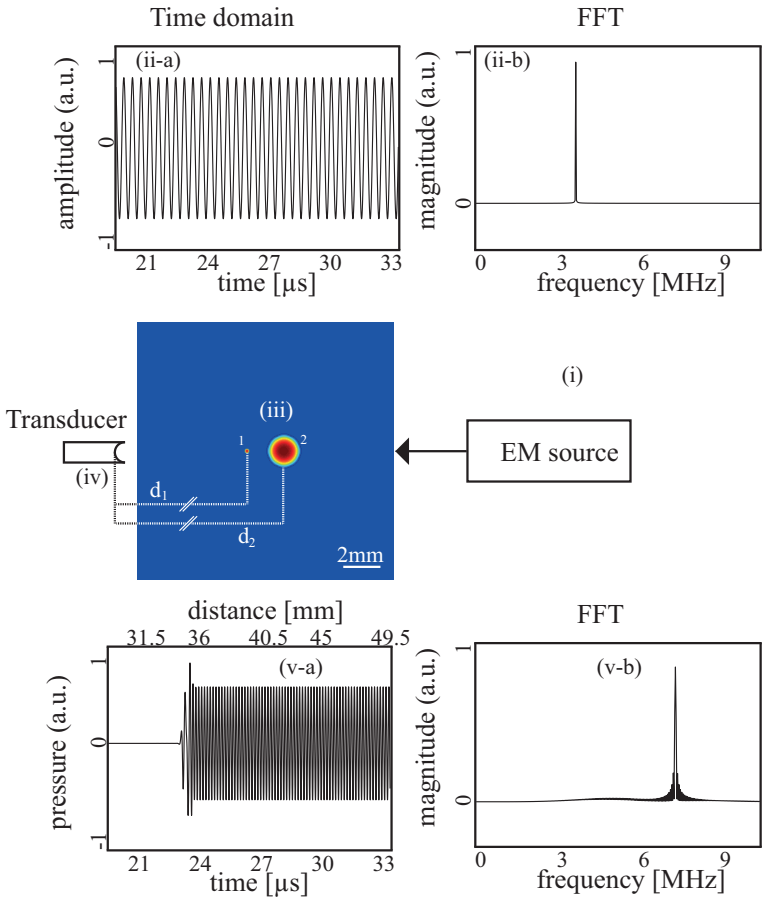

Figure 3.4: Illustration of the thermoacoustic simulation: (i) CW electromagnetic source; (ii-a) CW modulation signal at $f_{CW} = 3.5$ MHz; (ii-b) corresponding FFT of (ii-a); (iii) object 1 (⌀ 0.4 mm) and object 2 (⌀ 2 mm); (iv) ultrasound transducer; (v-a) thermoacoustic response; (v-b) corresponding FFT of (v-a), exhibiting a narrowband response at $f_{tas,CW} = 2 \cdot f_{CW} = 7$ MHz

4 Image reconstruction

4.1 Introduction

This chapter describes two different techniques to reconstruct opto- and thermoacoustic images from a set of measured acoustic signals. The first method in section 4.2 explains the well-known backprojection reconstruction algorithm which is used for time domain thermoacoustic tomography. Section 4.3 points out the frequency domain approach to convert optoacoustic data into tomographic images. Pulse compression with coherent processing which is implemented in radar imaging is adapted for application in frequency domain optoacoustic imaging. The cross correlation method is furthermore discussed which enables spatial tracking of optical absorbers in the region of interest. Cross sectional images are finally attained with the above mentioned backprojection algorithm.

4.2 Time domain thermoacoustic image reconstruction

This section discusses first a typical implementation of a time domain thermoacoustic tomography system. Characteristic TD-features like synchronization of the RF source with the data acquisition, time of flight measurements and scanning geometry are presented. Subsequently, the reconstruction algorithm which is based on the universal backprojection by Xu et al. [128] is explained with respect to fundamental equations and a schematic layout of the image discretization.

4.2.1 Tomographic implementation in time domain thermoacoustics

Figure 4.1 illustrates schematically a time domain tomographic measurement scenario with a pulsed RF source. On the input side, an electromagnetic source emits high energy

RF pulses which are guided onto the object. Upon absorption, the object subsequently discharges the energy by thermal expansion in a broadband acoustic pressure wave (circular dashed line). An ultrasonic transducer which is usually based on PZT or PVDF converts pressure waves into voltage signal equivalents. Rotation of the transducer around the object results in multi-projection data collection at several angular positions. Thus, a tomographic data set can be acquired which is used for signal processing and reconstruction in order to obtain a cross sectional view of the sample. Finally, the reconstructed data set can be displayed on a screen.

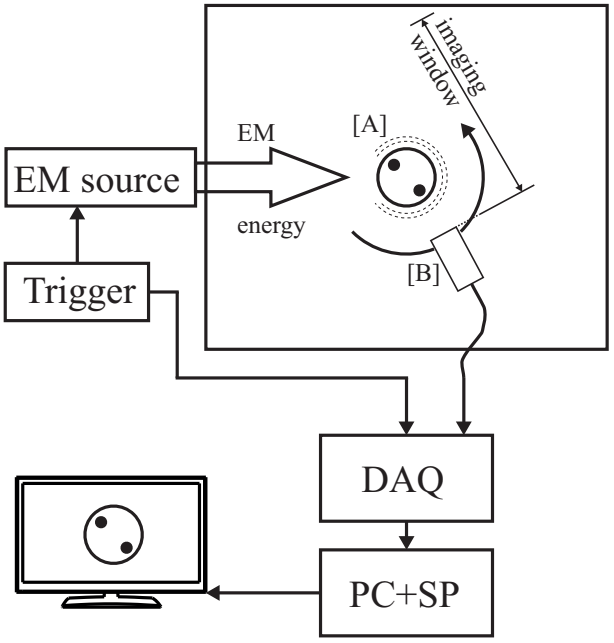

Figure 4.1: Schematic of the tomographic implementation for time domain thermoacoustics - DAQ: Data Acquisition; PC: Personal Computer; SP: Signal Processing; [A] object with emanating acoustic waves; [B] ultrasonic detection unit

The consecutive steps of a time of flight measurement scenario with acoustic wave detection - trigger event synchronization are illustrated in figure 4.2. An ultrashort EM pulse [A], marked as pulse #1, travels at speed $c = (\mu_0 \mu_r \varepsilon_0 \varepsilon_r)^{-0.5}$ to the absorber and simultaneously initiates the data acquisition DAQ 1. An acoustic wave pas #1 is induced subsequently to absorption of EM energy and propagates in a coupling medium at travel speed v_s. Water is commonly used as a coupling fluid with an acoustic speed of $v_s \approx 1500$ m s^{-1}. A second impulse pulse #2 is launched at time point [D], restarting a new data acquisition DAQ 2 to record the acoustic signal pas #2. Note that the distance is proportional to the acquisition time which allows for tracing of the spatial distribution of absorbers.

The launch of the second pulse is defined by the pulse repetition frequency PRF which

is in the order of $10-100$ Hz in time domain macroscopic and mesoscopic opto- and thermoacoustic imaging.
Accordingly, the duty cycle can be obtained from equation

$$D_C = \frac{\tau_{pulse}}{T_p} \tag{4.1}$$

as the ratio of the pulse duration event τ_{pulse} and the period T_p. For example, a pulse repetition rate of 10 Hz with a pulse duration of 10 ns results in a duty cycle of $D_C = 1 \times 10^{-5}$ in time domain thermoacoustics.
Furthermore, the imaging window (see figures 4.1 and 4.2) is defined by the time and accordingly space interval between two trigger events. Therefore, following the initial trigger event, the subsequent trigger has to be initiated after the signal acquisition DAQ 1 has been finished.
According to a sample calculation which assumes an imaging window of 50 mm, meaning that all absorbers within the region of measurement are at a distance of $r = 50$ mm from the detector, yields an imaging time frame of $t_{image} = 75$ µs. The time lag between two pulses t_{p-p} has to be longer than the imaging time frame $t_{p-p} > t_{image}$ to assure correct resolution of signals. Initiating stimulation pulses before completing data acquisition results in overlapping acoustic waves and accordingly in erroneous signal detection.

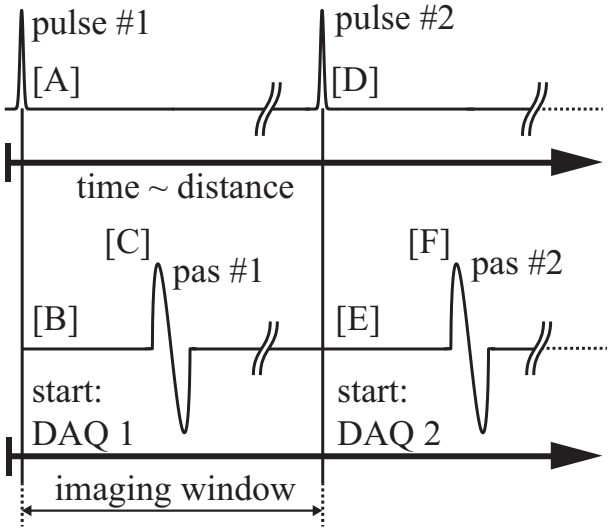

Figure 4.2: Pulse sequence in time domain thermoacoustic imaging; top row: excitation pulses; bottom row: acoustic response; [A] launch of pulse #1; [B] start of Data Acquisition DAQ 1; [C] thermoacoustic response pas #1 from pulse #1; [D] initiation of pulse #2; [E] restart of Data Acquisition DAQ 2; [F] photoacoustic response pas #2 from pulse #2

4.2.2 The backprojection algorithm

The final experimental implementation of the time domain thermoacoustic imaging system which will be described in chapter 5 allowed for thermoacoustic wave detection with cylindrically focused ultrasonic transducers; therefore, thermoacoustic signals were detected from a transversal view. This confines the reconstruction model to a 2 dimensional topology. Similar to time domain image reconstruction in optoacoustic tomography [76], [103], thermoacoustic images presented in this work are reconstructed with a modified universal backprojection algorithm for photoacoustic tomography. The holistic approach to the universal backprojection algorithm can be found in [128], therefore only the basic equations of the universal backprojection formula are described in this section.

Tomographic signal acquisition and image reconstruction implied several steps.

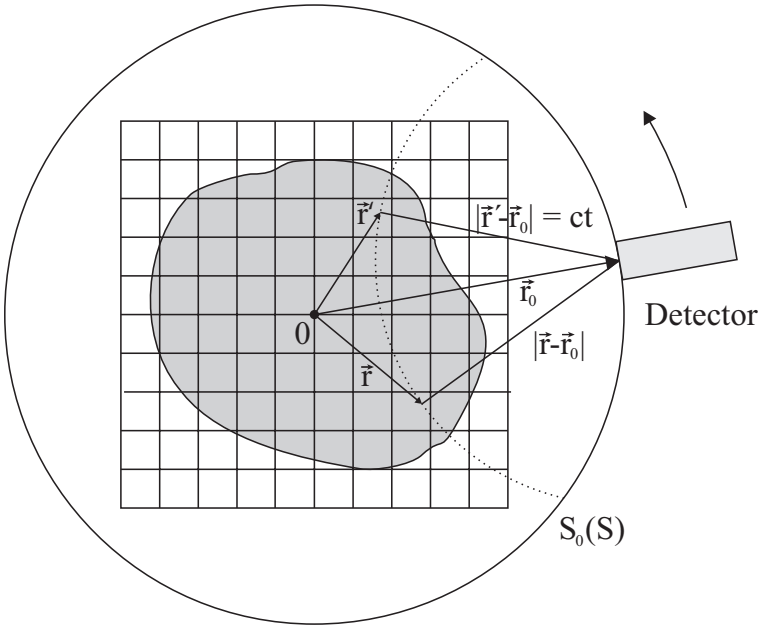

Figure 4.3: Schematic of the spatial discretization: transducer located at position $\vec{r}_0$ detects acoustic signals at arcs covering distances ct with the center of rotation at $x = y = 0$

Figure 4.3 depicts the measurement geometry and image discretization space. In a first step, a thermoacoustic signal, containing the superimposed acoustic waves at the radial distance $r = c \cdot t$ is detected at a specific predefined angle around the object, called projection. The time of flight measurement is then projected onto a predefined mesh which correlates the time dependent thermoacoustic signal to radial distance from the detection element. Moving the detection element to the next projection angle relatively to

the imaging center of rotation (tagged as 0 in figure 4.3), further thermoacoustic signals are detected, projecting the signals in a similar manner onto the grid. Summing up the thermoacoustic data set ends up in a tomographic cross-sectional view of the object where the time-dependent thermoacoustic signals are converted to a spatial dependence with the relationship from equation 3.16

$$r = v_s t \tag{4.2}$$

where t defines the imaging window or equivalently acquisition time frame.

Mathematically, the backprojection algorithm represents an inversion formula to the forward solution of the photoacoustic wave equation 3.15 under assumption of delta excitation. With the Grüneisen parameter $\Gamma = v_s^2 \beta C_p^{-1}$, equation 3.15 can be rewritten in the form

$$p(\vec{r}',t) = \frac{\Gamma}{4\pi v_s^2} \frac{\partial}{\partial t} \int \frac{H(\vec{r}')}{|\vec{r}-\vec{r}'|} dA'. \tag{4.3}$$

Xu et al. [128] proposed a first order approximation to the inversion formula, resulting in the universal backprojection formula given as

$$H(\vec{r}) = -\frac{1}{2\pi v_s^2 \Gamma} \int_S t \left[\frac{\partial p(\vec{r}_0, t = \left|\vec{r}-\vec{r}_0{}'\right| v_s^{-1})}{\partial t} - \frac{p(\vec{r}_0, t = \left|\vec{r}-\vec{r}_0{}'\right| v_s^{-1})}{t} \right] dS. \tag{4.4}$$

The integral in the backprojection term contains a direct component of measured acoustic pressure $p(\vec{r},t)$ referred to as 'delay and sum' term whereas the time derivative part is called modified backprojection reconstruction. Cross sectional images from a set of tomographic data can finally be reconstructed separately or as a combination of both direct and time derivative components.

4.3 Image formation with CW excitation

This section discusses the frequency domain approach towards optoacoustic image reconstruction. FD optoacoustics does not provide time of flight measurements with a direct time - space relationship of absorbers relatively to the detector. Therefore, a different method is presented which is based on the cross correlation to trace back the phase delay of absorbers. Two cases are compared: Section 4.3.1 first discusses a monofrequent excitation scheme unfolding problems like low spatial resolution before section 4.3.2 describes the pulse compression method. Here, frequency modulation of stimulation signals

significantly improves resolution allowing for exact spatial tracking of absorbers.
The section is completed with a schematic implementation of optoacoustic signal excitation and detection within a tomographic imaging system.

4.3.1 Spatial tracking of absorbers employing CW sources

As described in the preceding section, time domain thermo- and optoacoustic tomography employ time of flight measurements to define radial distances of absorbers from the detector. In contrast, FD thermo- and optoacoustics are continuously exciting acoustic waves not confined by distinct trigger pulses. Therefore, acoustic signals can not be directly matched to one trigger event.

Instead of time of flight measurements, the spatial distribution of absorbers can be traced back with the application of distinct processing algorithms, e.g. the cross correlation method. The cross correlation approach allows for calculation of the phase delay between signals which can further be converted into an equivalent time delay.
Equations

$$cc(t) = \int_{-\infty}^{\infty} l^*_{ref}(t) \cdot p(t+\tau)dt \tag{4.5}$$

$$\hat{cc}(\omega) = \hat{l}^*_{ref}(\omega) \cdot \hat{p}(\omega) \tag{4.6}$$

describe the relationship between two time signals $l_{ref}(t)$ and $p(t)$ under assumption of a time shift between both signals. Note that equation 4.5 relates to the time domain while expression 4.6 corresponds to the frequency domain. The modified convolution term 4.5 is simplified to a multiplication with the complex conjugate in the fourier domain 4.6. The result of the cross correlation gives an estimation of the degree to which two signals are correlated. In other words, the cross correlation yields a function which is dependent on the input functions with the time point t denoting maximum coherence.
Applying the method to optoacoustic signal tracking, the cross correlation of the known laser modulation signal $l_{ref}(t)$ with the measured optoacoustic response $p(t+\tau)$ results in a maximum at the time shift τ, equivalent to the distance of the absorber from the detector.
The following simulations present results for signal tracking with monofrequent CW excitation. Simulations were carried out with the approximation of homogeneous illumination and ideal optoacoustic signals neglecting attenuation, noise, energy conversion and detection bandwidth. Simulation parameters with 2 point absorbers are depicted in figure 4.4. Absorber 1 has a distance of $d_1 = 15$ mm from the detector, absorber 2 is

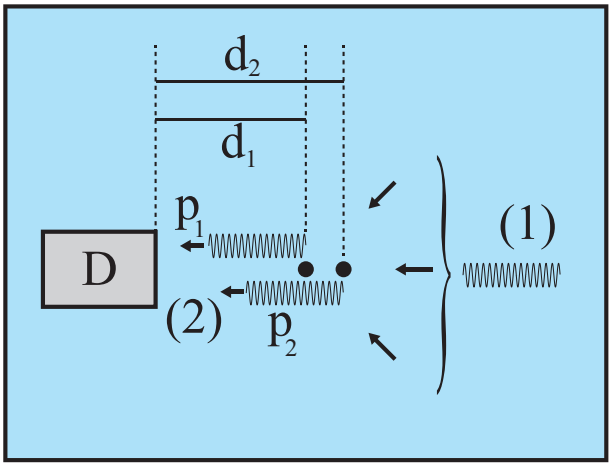

Figure 4.4: Simulation layout for monofrequent CW excitation of two absorbers: D - acoustic detector; p_1 - acoustic pressure wave 1 induced at distance $d_1 = 15$ mm from the detector; p_2 acoustic pressure wave 2 induced at position $d_2 = 21$ mm from the detector

located at $d_2 = 21$ mm from the detector. Relating distance to time with the acoustic speed of sound, the point absorbers are located at time points $t_{d1} = 10$ µs and $t_{d2} = 14$ µs. Following CW stimulation (marked as (1) in figure 4.4), two acoustic pressure waves p_1 and p_2 are induced which are emanating isotropically from object 1 and 2. Note that for the purpose of illustration only the acoustic waves pointing to the detector are portrayed.

The next step implies the calculation of the phase and accordingly time delay of the two absorbers with the cross correlation. Therefore, we have to compare the excitation signal and the simulated optoacoustic response from two absorbers.
Figure 4.5 plots the excitation signal which exhibits a monofrequent oscillation at $f_{cw} = 3.5$ MHz (see FFT in figure 4.5c). In this simulation, the signal lasts for 1 ms with respect to the easiness of illustration, however, in a realistic measurement scenario the illumination would be continuously on. Figure 4.5b shows a zoom shot of figure 4.5a, allowing for a better observation of the oscillation.
The ideal optoacoustic response from both absorbers is shown in figure 4.6a, again with a zoom shot depicted in figure 4.6b. At distance $d_1 = 15$ mm, corresponding to $t_{d1} = 10$ µs, the first absorber generates a CW optoacoustic signal followed by a second response, corresponding to the second absorber at distance $d_1 = 21$ mm or $t_{d1} = 14$ µs. It has to be remarked that the optoacoustic signals are interfering constructively at time point $t = 14$ µs. However, changing frequency, varying the distance between the absorbers or assuming multiple absorbers result in a more complex interference pattern.
Finally, figure 4.7a showcases the cross correlation result calculated from equation 4.5. For the purpose of understanding, the envelope function of the cross correlation in a time

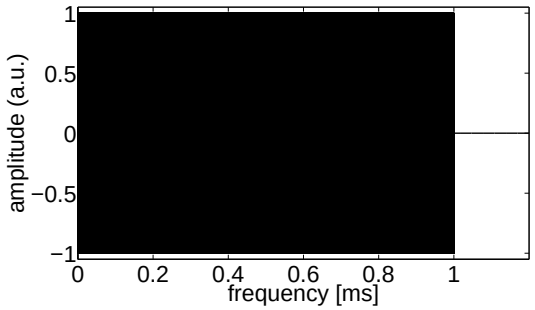

(a) Time domain signal

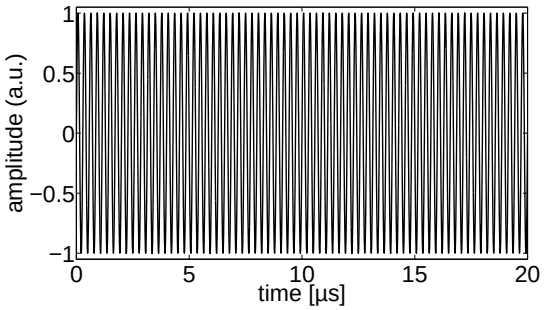

(b) Time domain signal - zoom on figure 4.5a

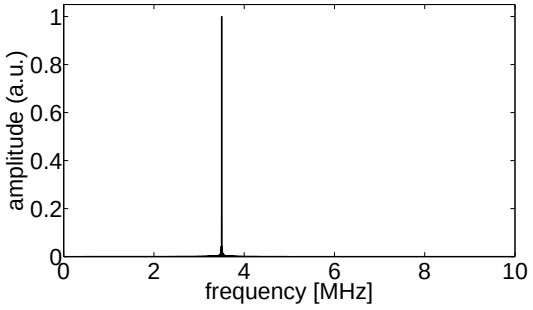

(c) Frequency domain signal

Figure 4.5: Frequency domain optoacoustic simulation: Excitation signal (1) as depicted in figure 4.4 in time domain and frequency domain; $f_{CW} = 3.5$ MHz

confined window is plotted in figure 4.7b. The envelope function clearly exhibits a flat maximum (and minimum which is not shown) at the time duration 10 µs $< t <$ 14 µs, corresponding to the location of the two absorbers.

Obviously, a correct resolution of two or more absorbers is not feasible with a monofrequent approach since the result of the cross correlation function yields a flat maximum, representing the distribution of all absorbers.

4.3.2 Pulse compression

Accurate tracking of absorbers at high spatial resolution can be achieved with the pulse compression method. According to Farnett and Stevens [115], "pulse compression involves the transmission of a long coded pulse and the processing of the received echo to obtain a relatively narrow pulse". In the first place, this statement is valid for Radar applications where Radar can be defined as "an electromagnetic sensor for the detection and location of reflecting objects" [116]. But, at the same time, this holds true for a CW optoacoustic (and thermoacoustic) measurement scenario where the RF source

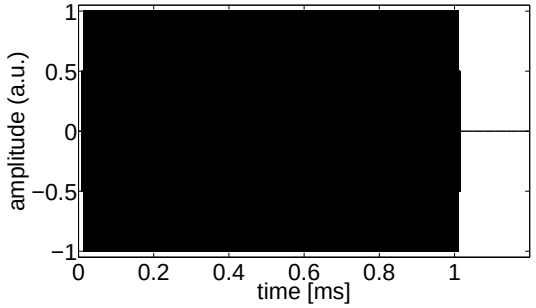

(a) Optoacoustic response in time domain

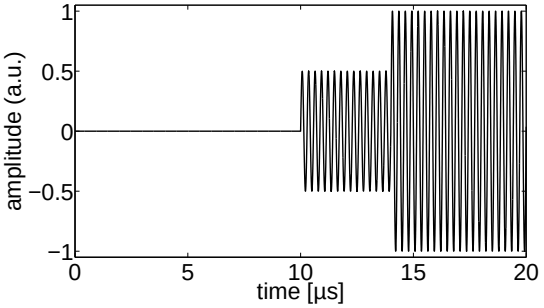

(b) Optoacoustic response in time domain - zoom on figure 4.6a

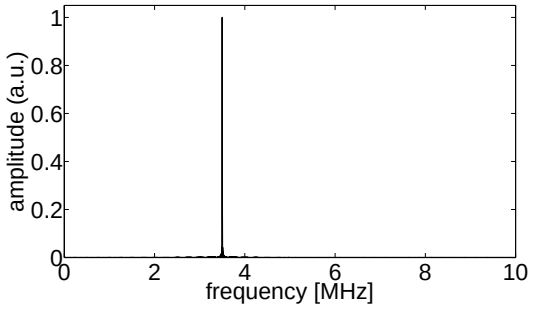

(c) Optoacoustic response in frequency domain

Figure 4.6: Frequency domain optoacoustic simulation: Optoacoustic response (2) as depicted in figure 4.4 in time and frequency domain; $f_{OAS} = f_{CW} = 3.5$ MHz

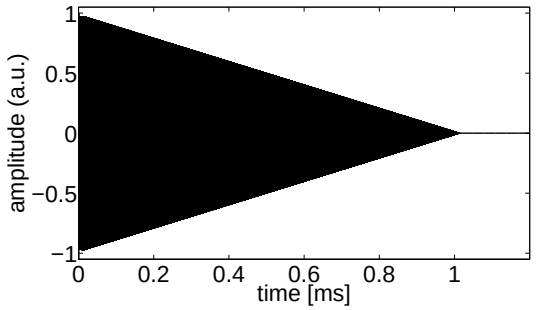

(a) Cross correlation

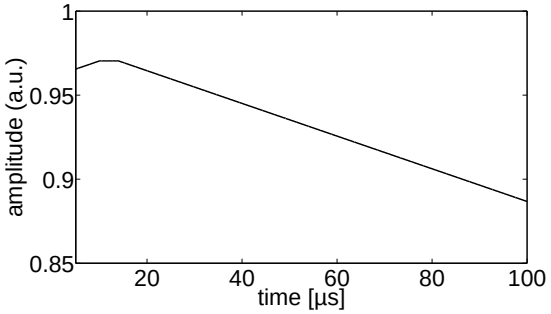

(b) Envelope of cross correlation from figure 4.7a

Figure 4.7: Monofrequent cross correlation result of two absorbers with the envelope function revealing the approximate position/time delay

is substituted by a laser and instead of reflection the absorption of objects in form of acoustic waves is measured.

Implementation of pulse compression in frequency domain optoacoustic imaging has been published by Telenkov et al. [123], [121], [122] for a specific lateral illumi-

nation and detection geometry. There are several advantages associated with the pulse compression approach, especially for CW optoacoustic tomography. Since the acoustic response in a CW excitation scenario represents a replica of the modulation signal (see section 3.5), the modulation bandwidth can be chosen according to the detection bandwidth of the transducer. Furthermore, pulse compression involves the application of matched filters for enhancing SNR. Another important point is that pulse compression allows for accurate spatial tracing of absorbers within the detection plane, enabling image reconstruction with continuous wave lasers.

The following simulation presents one specific pulse compression example, demonstrating the waveform signals of excitation and acoustic response along with the cross correlation result.
The modulation waveform can be defined as

$$x(t) = A\cos(2\pi f_0 t + \pi b t^2) \tag{4.7}$$

with the initial frequency f_0, the amplitude A and the sweep rate b for the case of linear waveform modulation.
Simulation parameters, illustrated in figure 4.8, are similar to the previous section 4.3.1. Two point absorbers are homogeneously illuminated with a frequency chirp (portrayed as (1) in figure 4.8). Optoacoustic signals are induced in both absorbers which are located at position $d_1 = 15$ mm and $d_2 = 21$ mm. Although ultrasonic waves (marked as (2) in figure 4.8) are propagating isotropically, only acoustic waves facing the detector are illustrated.
The reference signal $l_{ref}(t)$, equivalent to the excitation signal in optoacoustic tomography, represents a linear frequency modulated waveform according to equation 4.7, covering a bandwidth of 4 MHz and starting from $f_{start} = 1$ MHz. Figure 4.9a shows the time domain signal with a chirp duration of 1 ms, exhibiting a frequency of 1 MHz at time point $t = 0$ s and reaching 5 MHz at the end of the chirp ($t = 1$ ms). A small sector from the chirp signal is shown in figure 4.9b. In frequency domain, the chirp signal covers a bandwidth of 4 MHz as depicted in the FFT of the chirp signal in figure 4.9c. It has to be noted that in a realistic measurement scenario the object is exposed to continuous wave excitation and not only one time confined chirp as depicted in figure 4.9. However, for the easiness of illustration, only one time-limited chirp is shown here.

Assuming 2 point absorbers as depicted in figure 4.8, the detected ideal pressure signal $p(t)$, neglecting attenuation, noise, energy conversion efficiency and detection bandwidth, resembles the waveform plotted in figure 4.10a, with a small section depicted

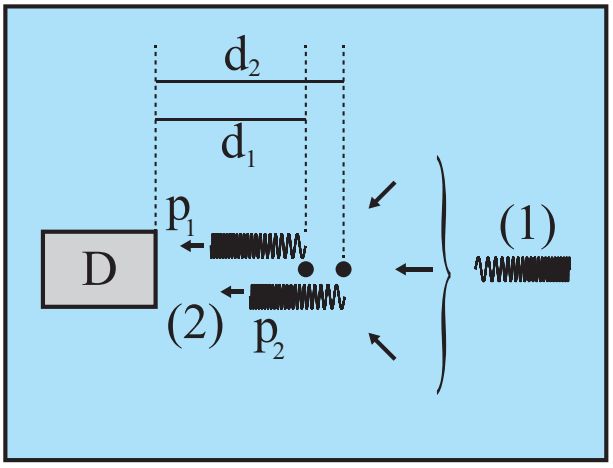

Figure 4.8: Simulation layout for 2 absorbers at distances $d_1 = 15$ mm and $d_2 = 21$ mm from the detector D

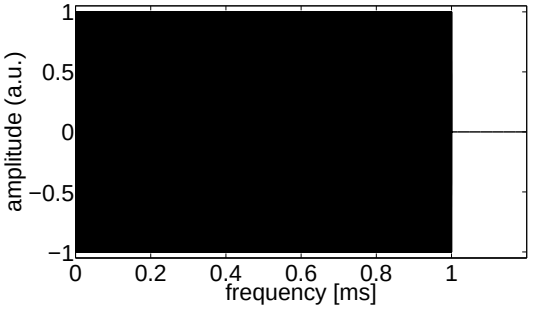

(a) Chirp modulation signal starting at $f_{start} = 1$ MHz covering a bandwidth of 4 MHz

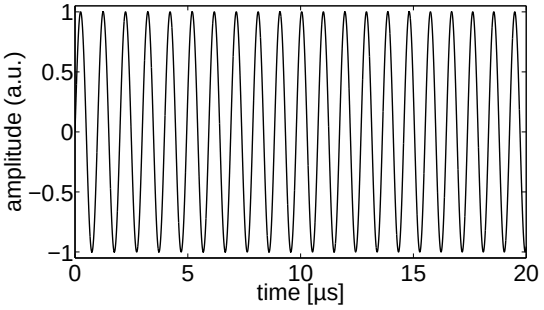

(b) Chirp modulation signal - zoom on figure 4.9a

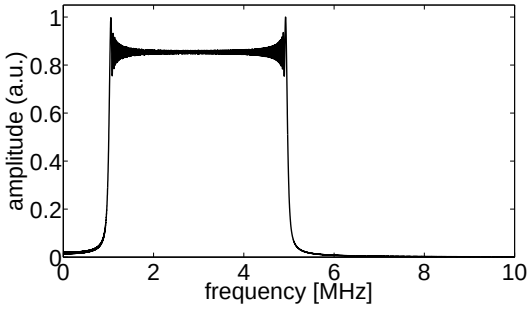

(c) Corresponding FFT of chirp modulation signal

Figure 4.9: Pulse compression simulation: Chirp signal $l_{ref}(t)$ (1) as depicted in figure 4.8 in time domain and frequency domain using a chirp bandwidth of 4 MHz

in figure 4.10b. The corresponding frequency domain signal is shown in figure 4.10c. The time domain signal exhibits an interference pattern due to the superposition of acoustic signals originating from different absorbers. Furthermore, the time domain signal is

phase shifted by $t_1 = 10$ µs, corresponding to the distance $d_1 = 15$ mm from the absorber 1 to the detector.

The phase delay of both absorbers can be reconstructed using equation 4.5, yielding the result plotted in figure 4.11. The cross correlation result of the interference pattern 4.10a with the reference pattern 4.9a highlights 2 peaks, corresponding to the two point absorbers at distances 15 mm and 21 mm. Clearly, it exhibits the shape of a sinc function which is a result of the cross correlation between two frequency modulated chirps. Thus, the cross correlation in combination with the pulse compression method is able to recover accurately the position of optical absorbers.

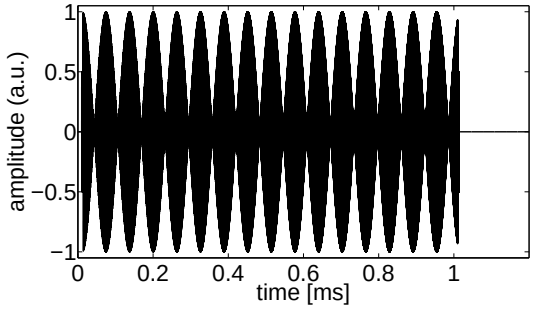

(a) Optoacoustic response in time domain

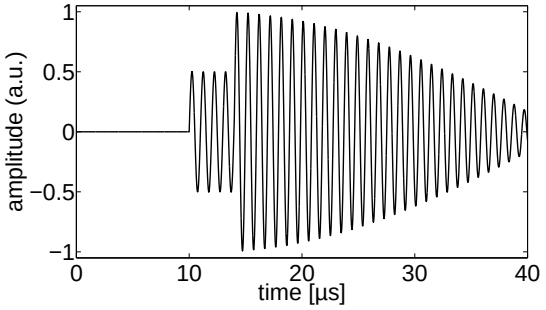

(b) Optoacoustic response in time domain - zoom on figure 4.10a

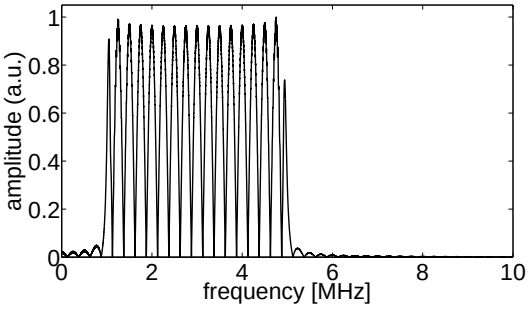

(c) Optoacoustic response in frequency domain

Figure 4.10: Optoacoustic response $p(t)$ from two absorbers in time and frequency domain; $f_{start} = 1$ MHz; $f_{stop} = 5$ MHz

4.3.3 Schematic implementation of the tomographic FD-Scanner

Pulse compression in combination with coherent processing methods like the cross correlation allows for spatial resolution of absorbers. The implementation of the signal

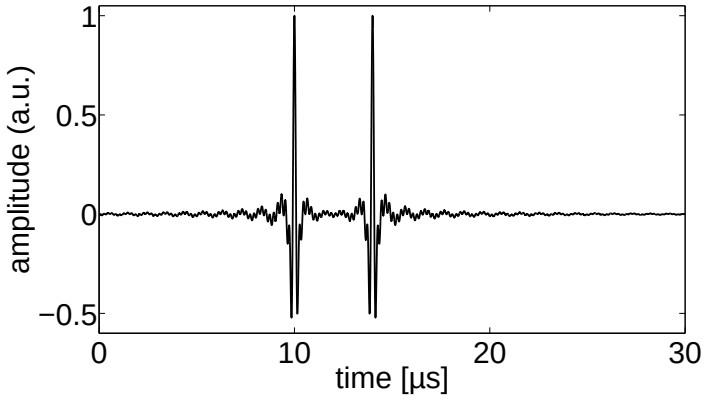

Figure 4.11: Cross correlation of the laser reference $l^*_{ref}(t)$ with the optoacoustic signal $p(t)$ according to equation 4.5, recovering the time delay and correspondingly the position of the two absorbers

processing method in the FD tomographic scanner is briefly explained here to underline the operation mode of acoustic wave excitation and detection. However, the holistic approach with an experimental setup is described in chapter 6.

In the previous section, optoacoustic signals were simulated with one excitation chirp. In a practical optoacoustic experiment, a set of several consecutive chirps is launched onto the object. Figure 4.12 illustrates the frequency domain equivalent to the pulsed thermoacoustic approach from figure 4.2. In this example, three chirps are shown with the data acquisition starting at the launch of chirp #1 (equivalent to marker (A)). The optoacoustic response is time-delayed (marked as (B)) and repeating with the stimulation chirps.

Implementing the concept into a tomographic setup yields the schematic shown in figure 4.13. The sketch demonstrates briefly the design which can be used to acquire optoacoustic data originating from CW optical excitation over several projections. An optical fiber [A] guides modulated light to the sample [C]. Optoacoustic signals are excited due to CW stimulation and captured by an ultrasonic transducer [B]. As an example, two projections are portrayed, the first projection $\{p = 1\}$ in solid lines at $\phi = 0^\circ$ and another projection at $\phi = 180^\circ$, illustrated in dashed lines. The number of projections is only limited by time, a fact which will be observed in chapter 6.

Comparing the schematic system to the time domain (Fig. 4.1), an important FD feature is the simultaneous data acquisition (DAQ) of both the modulation signal which is generated by a function generator (FG) and the optoacoustic signal. This is due to the coherent processing concept which cross correlates the *a-priori* known reference, i.e. the laser modulation signal with the measured acoustic signal. Another important difference is the trigger generator which synchronizes the data acquisition and the function generator. The

trigger event defines the start of the reference as well as the optoacoustic measurement since both are coupled. The trigger event is important for correct coherent processing since it defines the launch of the chirp at time point $t = 0$. The PC with the signal processing unit performs the cross correlation and forms images from the measured data. Therefore, cross sectional images of objects can be reconstructed by cross correlating the reference signals $l_{ref}(t)$ with the optoacoustic signals $p(t)$ at each projection and employing the backprojection formula given in section 4.2.2.

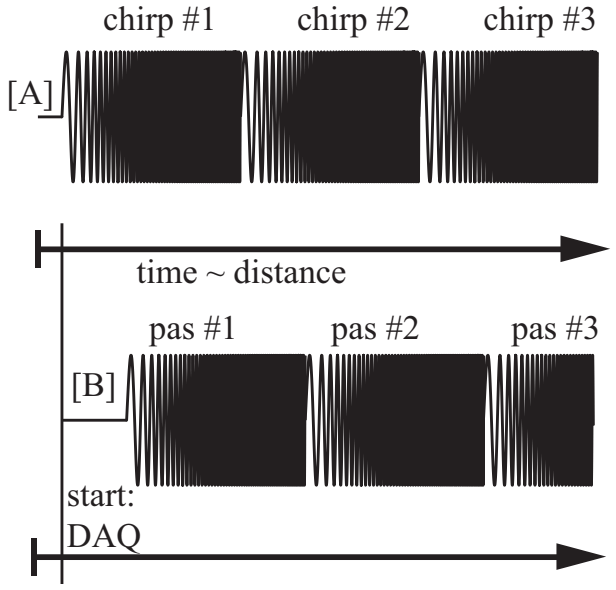

Figure 4.12: Chirp sequence in frequency domain optoacoustic imaging; top: excitation chirps; bottom: acoustic response; [A] launch of frequency modulated chirps ($chirp_x$); [B] photoacoustic responses pas_x due to excitation chirps (chirp_x)

Finally, 4.14 schematically depicts the topology of a typical frequency domain tomographic measurement. At projection pj, a trigger event is occurring, launching an electrical chirp which is driving the laser and triggering the data acquisition. The optical chirp is then guided onto the object, inducing acoustic pressure waves. An acoustic detector captures the mechanical waves and a data acquisition system acquires both the acoustic signal and the modulation signal. After a complete data set is acquired, the PC sends a command for a new projection, moving the motion controller to the next measurement angle, restarting the whole procedure. Repeating the routine over pre-defined projections yields in a tomographic data set which is used for frequency domain reconstruction using the backprojection formula.

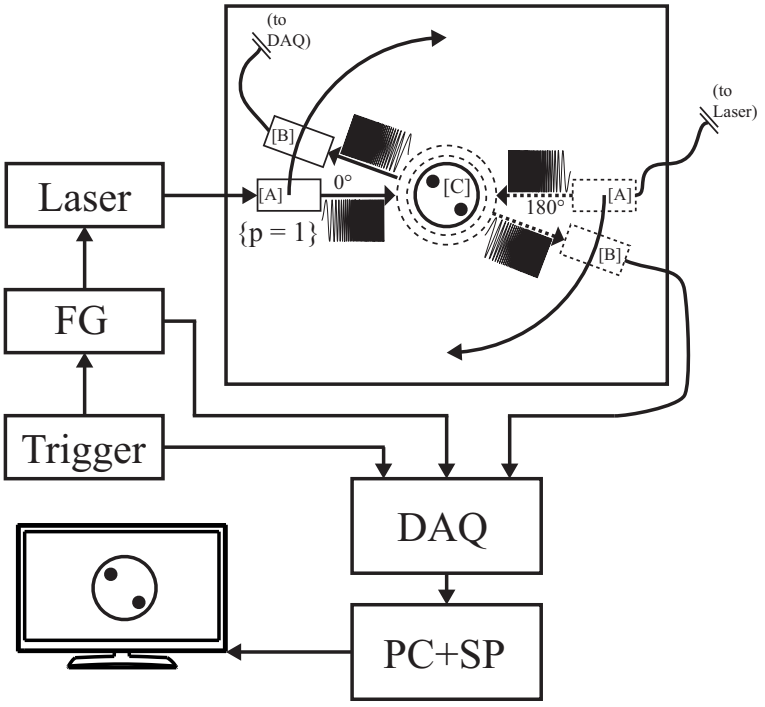

Figure 4.13: Schematic of the tomographic implementation for frequency domain optoacoustics; solid line: projection at 0°; dashed line: sample projection at 180°; [A] laser source; [B] acoustic detector; [C] object; FG: Function Generator; DAQ: Data Acquisition; PC+SP: Personal Computer and Signal Processing

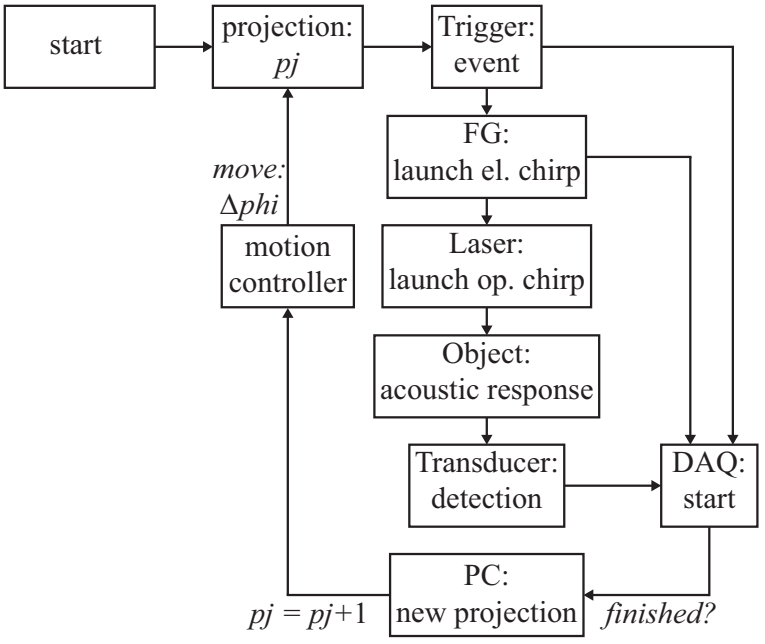

Figure 4.14: Schematic topology of tomographic data acquisition

4.4 Summary and conclusive remarks

This chapter discussed image reconstruction in time and frequency domain employing a modified version of the backprojection algorithm. Whereas time domain thermoacoustic images can be reconstructed directly from measured acoustic signals, frequency domain optoacoustic signals require further signal processing in order to retrieve the spatial distribution of absorbers. The pulse compression method in combination with the cross correlation was presented which allows for calculation of the time delay of absorbers within the imaging plane. After coherent processing, image reconstruction is facilitated in a similar way as the time domain approach, combining the time delay of absorbers with the backprojection algorithm.

5 Time domain thermoacoustic tomography

5.1 Introduction

This chapter discusses thermoacoustic tomography in the time domain. Considering various approaches towards thermoacoustic signal generation, section 5.2 clusters TAT into its contemporary derivatives and reviews furthermore four different types of conventional thermoacoustic imaging systems. Deficiencies coupled to conventional TAT approaches are pointed out which served as a motivation towards a novel design for a RF-based thermoacoustic imaging system operating in the near-field. In particular with respect to the scheme of excitation, section 5.3 discusses the new approach towards thermoacoustic signal generation, also taking into account design considerations for the new imaging system; here, benefits of the new design compared to other thermoacoustic imaging modalities are presented. Furthermore, the physical basics of the near-field approach are briefly explained, giving a definition of the radiation fields of an electromagnetic energy emitting element. One key point includes the experimental near-field radiofrequency thermoacoustic (NRT) tomography setup that has been built at the Institute for Biological and Medical Imaging (IBMI). The schematic of the pulse generator is presented along with the experimental tomography setup, used for both phantom and small animal imaging. Dedicated simulations prove the energy absorption in the near-field of EM energy dissipators. Proceeding to the results, the performance of the system is tested on various phantoms and copper wires to determine the spatial resolution of the system before going towards biological imaging and finally *ex-vivo* small animal imaging.
Section 5.4 continues the evaluation of the developed tomography scanner, unfolding the limitations that come along with the design. Finally, section 5.5 discusses the results and gives a further outlook.

5.2 Existing thermoacoustic tomography systems

Diagram 5.1 showcases various implementations of thermoacoustic imaging systems. Whether based on a pulse modulated high power microwave source [130], [83], [67] or on electric current pulses [10], the physical phenomenon of electromagnetic energy dissipation within the target is common to all thermoacoustic implementations. Referring to the former method, the microwave source usually exhibits frequencies in the hundreds of MHz [63] or goes up to several GHz [52] and is typically pulse modulated with durations of 500 ns to 1 ms. Regarding the latter methodology, electric current pulses are used for thermal stimulation of tissue. However, another approach is operating the target within the cavity of a propagating electromagnetic field [29].
Referring to signal acquisition, acoustic wave capturing is either implemented in a single detection geometry [10] where either the transducer or the object is rotated to acquire acoustic data from different projections [71] or with multiple detectors as suggested in [66]. In what follows, a brief overview on different thermoacoustic signal generation and imaging methodologies is given.

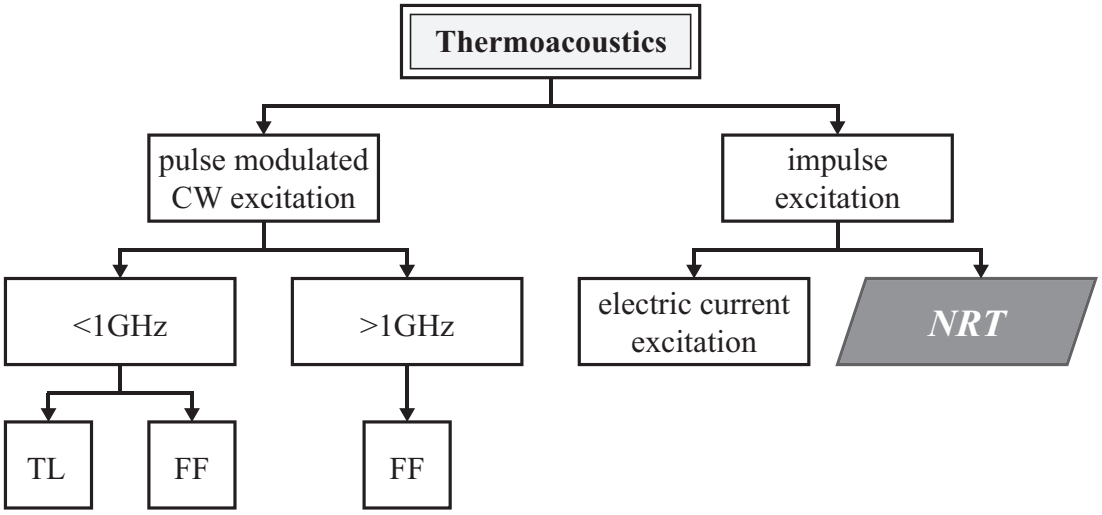

Figure 5.1: Overview of thermoacoustic imaging modalities in time domain; TL - transmission line based systems; FF - far field operating implementations; NRT - near-field based thermoacoustic imaging system

5.2.1 Thermoacoustic signal generation with electric current pulses

More than 40 years ago, Bowen et al. [10], [11] introduced an original way of inducing acoustic pressure waves following short pulse excitation. The key component in this

system is a custom made impulse generator that delivers electric current pulses onto the object under test. Impulses with durations of 0.4 µs were generated through discharging an energy storing capacitor by means of a thyratron. Voltage levels were limited to $\sim$ 1.2 kV, resulting in an energy per pulse of $\sim$ 3 mJ.
The apparatus allowed for *ex-vivo* experiments on muscle phantoms. Therefore, the phantom was placed in between electrodes, acting as the dielectric medium similar to a capacitor layout. The acoustic detection element was immersed in vegetable oil which was filled on top of the phantom to ensure acoustic coupling.
Thermoacoustic signals were also induced *in-vivo* on the human upper arm with simple application of contact gel between the electrodes and the transducer being attached to the arm.
Despite the low costs and manageable complexity of the approach, the obtained results were limited to signal generation only and did not yield images representing a map of electric current absorption. Furthermore, signal to noise ratio was low due to the low energy per pulse.

5.2.2 Thermoacoustic tomography at 434 MHz

The first thermoacoustic tomography system which aimed for *in-vivo* breast cancer imaging was reported over a decade ago in a publication by Kruger et al. [64]. Operating at 434 MHz, the thermoacoustic CT imaging system can be regarded as a pioneer towards clinical dissemination. The developed scanner consisted of a high power RF generator with 25 kW output power, delivering electromagnetic pulses either through an antenna [67] or a waveguide [68] within a duration of 500 ns. The generator could be triggered at a repetition rate of 4 kHz, resulting in a total average power of 50 W. This thermoacoustic pioneer system yielded high quality images of excised pork kidneys [64] along with breast cancer images [66] and overcame the limitations of pure microwave imaging which is restricted in resolution due to the long wavelength of microwaves [9].

However, the described scanner showcases the fundamental problem basically all thermoacoustic imaging systems are confronted with. This deficiency is associated with the duality between signal to noise ratio and spatial resolution. The described system stimulates tissue with long electromagnetic pulses in the order of 500 ns resulting in a spatial resolution of $\sim$ 1 mm. Shortening the pulse durations to enhance resolution compromises signal to noise ratio since less energy per pulse is stored in the sample. It is therefore a common practice to mitigate resolution demands by prolonging impulse durations to favor signal to noise ratio. Thus, this approach allowed for imaging of

bigger structures but also prevented thermoacoustics from small animal imaging at high resolution.

5.2.3 Thermoacoustic tomography employing GHz sources

Another similar approach moved to higher excitation frequencies, employing high power GHz sources. Stimulation frequencies are set to 3 GHz [69] with a peak power of 2 kW, recently also reaching power levels of 20 kW [95]: The pulse duration is typically in the range of 500 ns.
In a publication by Nie et al. [83], microwave sources at $f = 1.2$ GHz and $f = 6$ GHz with peak powers of 300 kW and pulse durations ranging from 300 ns up to 1.2 µs were employed. In both cases, oil was used as acoustic coupling medium.
Since the frequency is one order of magnitude higher compared to the method from section 5.2.2, absorption of electromagnetic energy is increased and tissue penetration is lowered. Whereas the previous system aimed mainly towards *in-vivo* breast cancer imaging, the above mentioned scanner also validated the possible application of contrast enhancers. In [96], contrast agents consisting of single-walled carbon nanotubes were applied to increase thermoacoustic signals, the first step towards molecular imaging.
Although the presented image quality is high and the potential role of TAT in molecular imaging was proven, the described systems do not benefit from the superior spatial resolution that the ultrasound detection theoretically offers; hence, these conventional thermoacoustic systems were still restrained from imaging small structures and performing small animal imaging.

5.2.4 Thermoacoustic imaging using a transmission line

Preceding systems placed objects in the far field of the EM energy emitting element, e.g. a microwave antenna or a waveguide. In the paper [29], Fallon et al. proposed a dedicated RF testbed to induce acoustic pressure waves. Instead of a microwave source where the load is ideally defined by the object, this approach consists of a RF generator that is connected to a metallic imaging tank which is terminated by coaxial cables. The imaging tank with defined geometrical dimensions operates as a cavity for the propagating EM-field. The object is placed within the cavity, damping the EM-field according to its absorption characteristics.
The methodology has several advantages:
The excitation frequency $f = 108$ MHz of the RF source is relatively low compared to

other systems, allowing for deep tissue penetration. The RF testbed uses deionized water as an acoustic coupling medium in contrast to mineral oil from other thermoacoustic imaging systems and it offers a well defined E-field with dominating TE10 wave. Especially the excitation concept, with the cavity providing input and output of the applied electromagnetic field, allows for monitoring of power absorption within the testbed which contains the object.
However, drawbacks are associated with the geometrical limitations since the cavity dimensions are defined by the resonance frequency, allowing only for imaging of objects which are within the cavity size. Furthermore, a dedicated shielding of electromagnetic interferences in order to protect the ultrasonic transducer has to be considered. Additionally, the pulse duration is > 240 ns, limiting the system from resolving small structures.

5.2.5 Summary of conventional thermoacoustic signal generation

The preceding sections should be regarded as a referential overview on state of the art thermoacoustic scanners. Certainly, developments in thermoacoustic imaging are not restricted in terms of applications but still derivatives of one of the above mentioned methods. As an example, Mashal et al. [77] operated a thermoacoustic scanner at 3 GHz as suggested in section 5.2.3, investigating the effect of microbubbles on thermoacoustic signals.
However, fundamental problems associated with conventional approaches can be boiled down to limitations connected to low power RF/microwave sources, focusing shortcomings and resolution deficiencies which are ultimately resulting in deficient signal generation.
As demonstrated above, the drawbacks in signal to noise ratio were overcome with a prolongation of the electromagnetic pulse duration. By increasing the excitation pulse to $\tau \approx 500$ ns, more energy could be stored in one pulse, thus increasing power deposition in the object. Although longer pulses yield higher SNR, at the same time resolution requirements are mitigated.
In order to image objects at high resolution, the electromagnetic pulses have to be ultrashort. Spatial resolution is inversely proportional to the excitation pulse duration, thus the shorter the pulse the better the resolution but at the same time the shorter the pulse the less energy it carries.
All these factors were taken into account when a new design was considered and developed which should ultimately overcome the limitations of thermoacoustic imaging.

5.3 Thermoacoustic tomography with impulse excitation

Summarizing the drawbacks associated with thermoacoustic imaging systems from the preceding sections, thermoacoustics operating in its conventional method offers low spatial resolution in the order of mm, needs complex and costly hardware and is struggling to achieve sufficient signal to noise ratio. Based upon these constraints, a novel excitation model was elaborated which will be presented in the following sections.

5.3.1 A sample calculation

Prior to motivation and design considerations for the thermoacoustic imaging system, a brief reference to the Introduction chapter 1 is given where optoacoustics and thermoacoustics were compared to each other. This is in particular important with respect to the design considerations for the novel thermoacoustic imaging system since the optoacoustic approach can be regarded as the gold standard. To recall, thermoacoustics is inherently struggling with a lower signal to noise ratio as compared to optoacoustics. Whereas optical light is highly scattered and absorbed within the first mm in biological tissue [125], radiowaves can easily penetrate the whole body with low scattering [129]. Moreover, optoacoustics takes advantage of the short wavelength of optical light, enabling focusing of optical beams onto confined areas. Thus, the laser energy per pulse which is usually $\sim 10-100$ mJ can be concentrated on small illumination spots, ending up in sufficient signal to noise ratio and high resolution with pulse durations $\tau < 10$ ns. This means that thermoacoustics with RF excitation has to cope with comparably low absorption, large wavelength of $\lambda_{RF} > 0.6$ m and less powerful sources. Especially the fact that RF radiation can not be focused to the same extent as optical light has to be taken into account into the design considerations.

In order to gain insight into the differences between optoacoustics and thermoacoustics, the following sample calculation compares radiant exposure, employing typical values from an optoacoustic system to ones from a thermoacoustic implementation.
Figure 5.2 depicts a chart of a laser beam with a diameter $\varnothing\,10$ mm hitting tissue surface. The laser pulses ($\lambda = 800$ nm) have energies $E = 10$ mJ with a duration of $\tau = 10$ ns. The assumed illumination spot of 10 mm would result in a radiant exposure of $H_{laser} \approx 13$ mJ cm^{-2}. This value is still within the maximum permissible exposure (MPE) level which is set to $MPE = 20\,C_A$ mJ cm^{-2} [3] where $C_A = 10^{2(\lambda-0.7)}$ for

$\lambda = 700 - 1050$ nm (λ in micrometer).

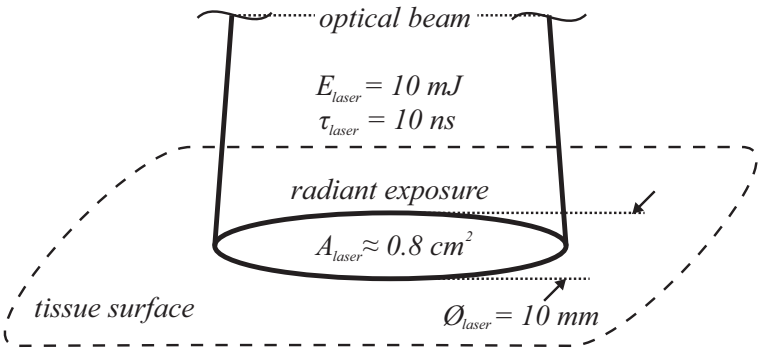

Figure 5.2: Schematic showing the optical radiant exposure on the tissue surface with calculation parameters

A similar calculation is performed for the RF case as shown in figure 5.3. Instead of a laser, this calculation assumes a microwave source with a carrier frequency of $f = 434$ MHz, a peak power of 25 kW and a pulse duration of $\tau_{RF} = 500$ ns. These values are taken from [66]. Although focusing of radiowaves is not feasible to the same extent as in the optical case, this calculation adopts a waveguide which is coupled closely to the tissue surface. Other radiating elements like a helical antenna can also be used, but with respect to the focusing capabilities of a waveguide over the helical antenna, the waveguide with its more directive field is chosen for the calculation. For the sake of easiness, the waveguide has a cylindrical shape and a diameter $\varnothing$ 8 cm, resulting in an aperture of $A_{RF} \approx 50\ \mathrm{cm}^2$. With these values, the radiant exposure is determined to $H_{RF} \approx 0.25\ \mathrm{mJ\ cm}^{-2}$.

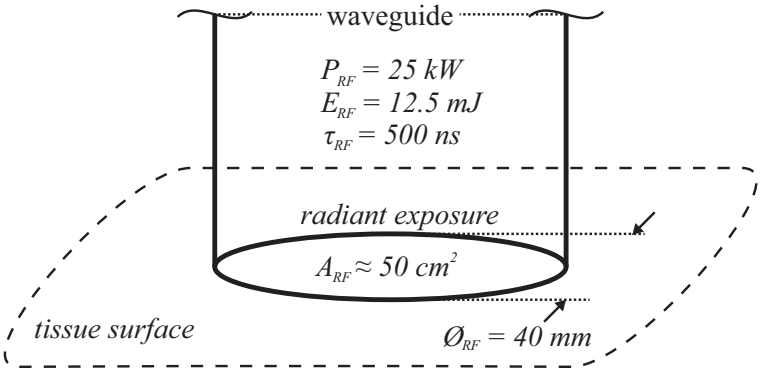

Figure 5.3: Schematic demonstrating the RF radiant exposure on the selected tissue surface along with calculation parameters

This coarse calculation sample assumes optimal radiant exposure under ideal conditions. Of course, in a realistic scenario only a portion of the energy within the waveguide is actually dissipated within the medium. Nevertheless, the radiant exposure for RF

excitation is > 50 times smaller than the optical counterpart due to the limited focusing capability and low power RF source.

5.3.2 Design considerations for a novel thermoacoustic method

This section discusses important design aspects and critical requirements to the thermoacoustic tomography system. Based on the results from previous sections and limitations of conventional thermoacoustic approaches, an 'ideal' thermoacoustic imaging system should be able to provide:

- high spatial resolution
- high signal to noise ratio
- cost efficient setup with manageable complexity
- high penetration depth

Referring to the first aspect, the resolution should be in the order of < 100 µm to allow for small animal imaging. With this resolution requirement, the electromagnetic pulse duration has to be $\tau_{RF} < 50$ ns, taking into account the inverse proportionality of spatial resolution and electromagnetic pulse duration.
Furthermore, the thermoacoustic method should achieve high signal to noise ratio without compromising high spatial resolution requirements. Performing a cross reference to optoacoustics which uses optical pulses with energies of $10-100$ mJ resulting in laser fluence $\Phi = 40$ mJ cm^{-2} [129], the thermoacoustic system should provide RF pulses with similar energies to ensure sufficient signal to noise ratio.
A third point involves a compact and inexpensive system which should provide the possibility of flexible transport. Therefore, low cost hardware components and compact technologies are needed.
A last point deals with the desirable feature of deep tissue imaging up to tens of cm as opposed to optoacoustics which is limited to few centimeters [87]. High tissue penetration requires RF excitation frequencies $f_{RF} < 100$ MHz [57] since water absorption of microwaves significantly restricts deep tissue penetration.

To summarize the demand profile, the novel thermoacoustic method needs to provide ultrashort RF pulses at $\tau_{RF} < 50$ ns with stimulation frequencies $f_{RF} < 100$ MHz and energies exceeding $E_{RF} = 100$ mJ/pulse.

5.3.3 NRT - a novel approach towards thermoacoustic signal generation

The majority of thermoacoustic imaging systems is based on pulse modulated CW excitation with its known deficiencies. However, in order to meet the requirements from section 5.3.2, an innovative thermoacoustic signal generation method is demanded.
Therefore, a similar model to the one described in 5.2.1 is considered. It basically relies on a source that emits ultrashort electromagnetic impulses which result in a broadband excitation. The short pulses carry energies of hundreds of mJoule to ensure decent thermoacoustic signal generation. To overcome focusing constraints, the biological object is closely coupled to an energy dissipating element since biological tissue has notable electromagnetic energy absorption in the near-field of RF sources [104], [19]. Since the novel thermoacoustic method is operating in the near-field, the term NRT - near-field radiofrequency thermoacoustic tomography - was adapted for the new technology. Especially the near-field energy coupling delineates the NRT method from the approach discussed in section 5.2.1. Whereas the latter induced an acoustic response by passing electric current directly through the tissue, the former relies on non-contact energy coupling in the reactive non-radiating zone of an energy dissipating element.

5.3.4 Near and far field definitions

Prior to the description of the schematic and experimental setup, this section reviews field radiation types of propagating electromagnetic fields.
The Hertzian dipole is used to define the radiation pattern of an antenna. This imaginary elementary antenna is an appropriate model to calculate the near and far field of a radiating element. The holistic approach towards the field equations is summarized in [133]; however, here only the basic equations are given.
The radiation pattern of a Hertzian dipole with the radial electric field component E_r, the inclination field component E_θ and the azimuth magnetic field component H_ϕ can be derived from Maxwell's equations to the following form:

$$H_\phi = j\frac{I\Delta l}{2\lambda}\frac{\exp(-jkr)}{r}sin\theta\left(1+\frac{1}{jkr}\right) \tag{5.1}$$

$$E_\theta = jZ_0\frac{I\Delta l}{2\lambda}\frac{\exp(-jkr)}{r}\sin\theta\left(1+\frac{1}{jkr}+\frac{1}{(jkr)^2}\right) \tag{5.2}$$

$$E_r = jZ_0 \frac{I\Delta l}{2\lambda} \frac{\exp(-jkr)}{r} 2\cos\theta \left(\frac{1}{jkr} + \frac{1}{(jkr)^2} \right) \tag{5.3}$$

Here, Z_0 denotes the free space wave impedance and Δl the characteristic length of the radiating element with the current I. Equations 5.1 to 5.3 contain expressions for both the far field and near field components. Depending on the distance r from the antenna, the radiation pattern can be separated into two field regions.

Near-field

Assuming the near-field condition $r \ll \lambda$, distance dependent phase rotations do not occur ($\exp(-jkr) \approx 1$) and only the components with highest power $(jkr)^{-p}$ are valid. Thus, equations 5.1 to 5.3 can be rewritten in the form

$$H_\phi \approx j \frac{I\Delta l}{2\lambda} \frac{\sin\theta}{r} \left(\frac{1}{jkr} \right) = \frac{I\Delta l}{4\pi} \frac{\sin\theta}{r^2} \tag{5.4}$$

$$E_\theta \approx jZ_0 \frac{I\Delta l}{2\lambda} \frac{\sin\theta}{r} \left(\frac{1}{(jkr)^2} \right) = -jZ_0 \frac{I\Delta l\lambda}{8\pi^2} \frac{\sin\theta}{r^3} \tag{5.5}$$

$$E_r \approx jZ_0 \frac{I\Delta l}{\lambda} \frac{\cos(\theta)}{r} \left(\frac{1}{(jkr)^2} \right) = -jZ_0 \frac{I\Delta l\lambda}{4\pi^2} \frac{\cos\theta}{r^3}. \tag{5.6}$$

In near-field condition, the electric and magnetic field components $\vec{E}$ and $\vec{H}$ are phase shifted by $\frac{\pi}{2}$. Additionally, the magnetic field is decreasing proportional to r^{-2} whereas the electric field is reduced by r^{-3}.

Far-field

In the far-field of the elementary dipole, equations 5.1 to 5.3 can be described by

$$H_\phi \approx j \frac{I\Delta l}{2\lambda} \frac{\exp(-jkr)}{r} \sin\theta \tag{5.7}$$

$$E_\theta \approx jZ_0 \frac{I\Delta l}{2\lambda} \frac{\exp(-jkr)}{r} \sin\theta \tag{5.8}$$

$$E_r \approx jZ_0 \frac{I\Delta l}{\lambda} \frac{\exp(-jkr)}{r} \cos\theta \frac{1}{jkr}. \tag{5.9}$$

In far-field conditions, only the components with lowest power $(jkr)^{-p}$ are valid. The magnetic and electric field components are of equal phase and decreasing proportional to r^{-1} (H_ϕ and E_θ) and r^{-2} (E_r) for equivalent energy. At far distances from the antenna, the term E_r becomes negligible and therefore the radial field component disappears.

Figure 5.4 depicts schematically the wavelength dependent radiation region of an electromagnetic energy transmitter (e.g. an antenna). The near-field can further be separated into a radiating near-field, also known as Fresnel region, and the reactive near-field. The transition from reactive to radiating near-field is defined by the wavelength dependent distance

$$R_{NF} = 0.62\sqrt{\frac{D^3}{\lambda}} \tag{5.10}$$

where D relates to the aperture of the antenna. In the reactive region, the imaginary part of the electromagnetic field components is dominant over the real part. Reaching the radiating near-field, the real part of the field starts to dominate; however, the field distribution is highly dependent on the distance from the transmitting element (see equations 5.4 to 5.6 where $E \sim r^{-3}$ and $H \sim r^{-2}$).
The far field, also called Fraunhofer region, begins at a distance

$$R_{FF} = 2\frac{D^2}{\lambda}. \tag{5.11}$$

Here, the field consists of transversal electromagnetic field components with radial parts $E_r = H_r = 0$.

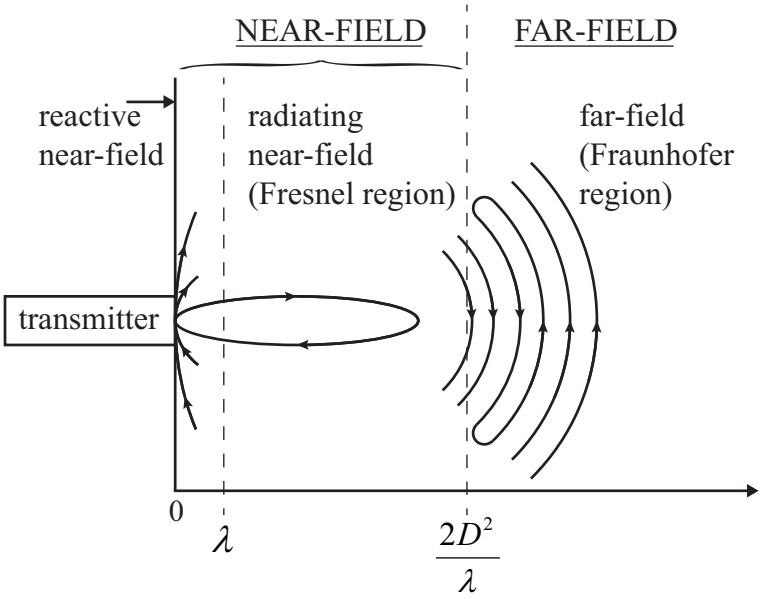

Figure 5.4: Wavelength dependent field zones originating from an electromagnetic energy transmitter; near-field is furthermore separated into reactive near-field and radiating near-field

5.3.5 NRT system components

The following sections are dedicated to the NRT setup . First of all, the custom made impulse generator is explained, showcasing its specifications and electric circuit. In the next step, the hardware components of the NRT setup are described.

5.3.5.1 Nanosecond impulse generator

The NRT method requires a dedicated impulse generator for efficient induction of thermoacoustic signals. As mentioned in sections 5.3.2 and 5.3.3, the pulser should provide ultrashort nanosecond impulses $\tau < 50$ ns, containing energies up to hundreds of mJoule per pulse. To match these requirements, a custom-built high voltage impulse generator which employs cost effective and common electronic components has been set up.
Figure 5.5 depicts the schematic of the nanosecond pulser. The transformer unit (External Trigger Transformer, Model: TR-1700, Perkin Elmer Optoelectronics, Fremont, CA, USA) splits the impulse generator into a low voltage (LV) and a high voltage (HV) part. The low voltage side is comprised of an input for the trigger signal and a dedicated circuit which transforms the low voltage trigger waveform into a 400 V signal. This is achieved by an adjustable DC power supply (Model: 1AA24-P20-M, Ultravolt, Inc., Ronkonkoma, NY, USA) which is controlled by a thyristor ($BTW69-1200$), triggered by the input pulse. Since the spark gap (Triggered Spark Gaps - Ceramic Metal, Model: GP-41B, Perkin Elmer Optoelectronics, Fremont, CA, USA) on the high voltage part expects a 28 kV signal for triggering, the 400 V signal on the LV-side has to be converted into a 28 kV signal using the $70:1$ transformer.
On the high voltage side, an adjustable high voltage power supply (Model: 30C24-N125, Ultravolt, Inc., Ronkonkoma, NY, USA) charges a RC circuit. The spark gap short circuits the RC circuit upon receiving a trigger signal from the transformer, thus creating a high voltage pulse in the nanosecond range. A part of the impulse energy is coupled into the object by means of the energy coupling element [A] (see figure 5.5) while a portion of the energy is also dissipated in the resistor R_{var}.

For a better understanding, figure 5.6 shows a simplified version of the electric circuit from figure 5.5 in form of a block diagram which should serve as the reference for following sections. Low voltage trigger signals are converted into high voltage counterparts to close the switch. The energy storage unit which is charged to -30 kV is short circuited in nanoseconds, resulting in high energy ultrashort impulses at the output. Lastly, the induced energy is transmitted into the object and partially dissipated in the resistor.

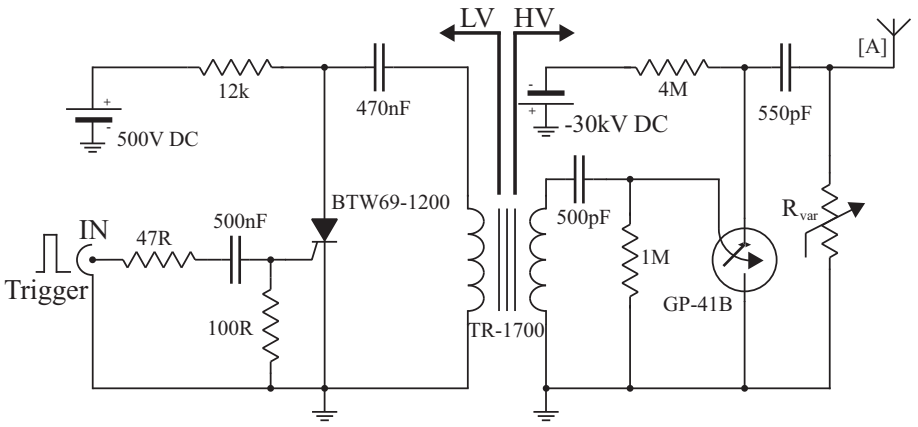

Figure 5.5: Schematic of the nanosecond impulse generator used for NRT measurements: [A] - energy coupler

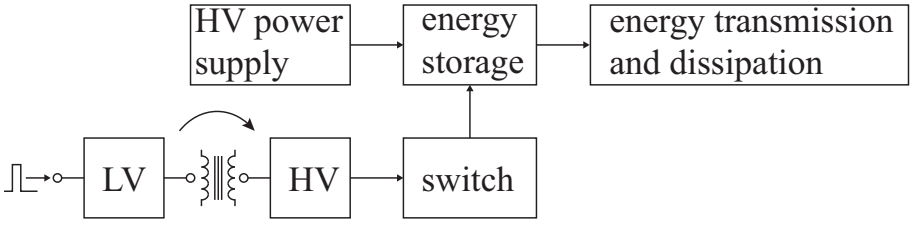

Figure 5.6: Block diagram describing the conversion from low voltage (LV) trigger signals to high voltage (HV) equivalents, resulting in nanosecond pulses

In NRT, the energy per pulse is determined by the capacitor value and the voltage of the power supply according to equation

$$E = \frac{1}{2} C U^2. \tag{5.12}$$

For the measurements presented in this chapter, a 500 nF capacitor was used, limiting the energy per pulse to $E_{NRT} \approx 250$ mJ. However, more energy can be stored by using bigger capacitors or increasing the voltage. Accordingly, bigger capacitors also result in longer pulses and shorter rise times, thus limiting the performance of the NRT method. Therefore, appropriate capacitor values have to be determined prior to measurements.

Taken from publication [57], figure 5.7 depicts the normalized output voltage of the nanosecond impulse generator using above described settings. The voltage is detected with a high voltage divider at the location of the energy coupling element. The full width half maximum (FWHM) of the impulse is shorter than $\tau_{pulse} \leq 22$ ns with a 10% to 90%

rise time $\tau_{rise} \leq 10$ ns. The corresponding fourier transform of the signal is shown in figure 5.7b, revealing a broadband frequency response with frequencies up to > 20 MHz, exhibiting a pronounced peak at $f_{RF,peak} \approx 10$ MHz.

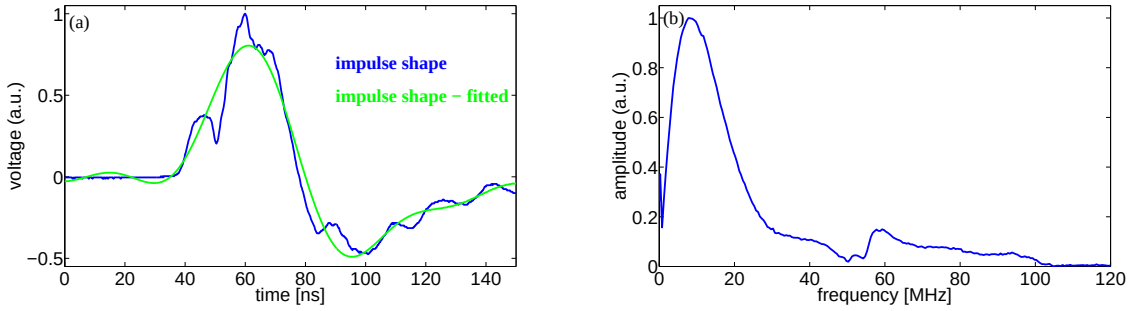

(a) Nanosecond impulse measured with a voltage divider (blue) along with a fit of the curve

(b) Corresponding fourier transform of the measured pulse shape (a)

Figure 5.7: Output of the impulse generator in time and fourier domain, measured at the output of the impulse generator with a high voltage divider (taken from [57])

5.3.5.2 NRT instrumentation

Figure 5.8 depicts the experimental NRT setup which was used to perform thermoacoustic tomography with impulse excitation. A similar schematic was described in 2011 in the publications [57], [58] while a modified version of the NRT setup with focus on phantom imaging was published by Razansky et al. [101]. Main components include the NRT source, the energy coupling element, the sample and the ultrasonic wave detection element.

The NRT source was driven by a function generator (Model 33210A Function/Arbitrary Waveform Generator, Agilent Technologies, Santa Clara, CA, USA) which created $+10$ V trigger pulses.
Referring to the energy coupling element, a helical shaped transmitter as depicted in the setup exhibited the best performance in terms of signal to noise ratio and stability of the system. This is attributed to the better impedance matching of the helical transmitter to the capacitive output of the nanosecond pulser. The sample was located in the close vicinity of the energy coupler to ensure maximum energy coupling. Depending on the size of the sample, two different ultrasound transducers were used for imaging. Table 5.1 lists a low frequent 3.5 MHz transducer that was mainly used for small animal and phantom NRT-imaging whereas the high frequent 7.5 MHz transducer was employed for

copper wire imaging to determine the resolution performance of the system. The water tank was comprised of two concentric cylinders which were filled with different mediums. The outer cylinder was filled with an RF absorbing saline solution at a concentration level of 0.2%, acting as a terminating layer which prevented the formation of standing waves in the imaging tank. The inner layer was filled with deionized water containing the sample, the transducer and the energy transmission element.

	Model	center frequency	focal distance	bandwidth	focus type
#1	V382	3.5 MHz	38.1 mm	76.3%	cylindrical
#2	V320	7.5 MHz	25.4 mm	77.5%	cylindrical

Table 5.1: Ultrasound detectors used for NRT imaging

A tomographic data set over 360° was acquired by either rotating the object or moving the transducer around the object with a rotational stage (Model PR50PP, Newport, Corporation, Irvine, CA, USA). Additionally, volumetric data acquisition from multiple planes was accomplished by vertical translation of the detector with a linear translation stage (LTA-HS,Newport Corporation, Irvine, CA, USA). A high speed 4-channel oscilloscope (Model DPO7254, Tektronix Inc., Beaverton, OR, USA) digitized data from the transducer at a sampling rate of 200 MS/s at 8 bit. Signal to noise ratio (SNR) could be increased by multiple acquisitions per projection and an optional broadband amplifier (Model AU-1332, Miteq, Hauppage, NY, USA). Data acquisition, positioning and triggering were controlled with a personal computer (PC) employing either a custom-built LabVIEW interface (LabVIEW2009, National Instruments, Austin, TX, USA) or a custom-developed Matlab code (Mathworks, Natick, MA, USA). To compensate for saturation effects of the transducer especially in combination with the amplifier, the thermoacoustic signals were high pass filtered with a custom made frequency filter at a cut-off frequency $f_{HP} = 300$ kHz.

5.3.6 NRT results

The following sections present numerical simulations and experimental results obtained with the developed near-field thermoacoustic scanner.
First, simulations showcase the near-field energy coupling capabilities. Two different software tools were used: COMSOL (COMSOL AB, Stockholm, Sweden) operating with the finite-element method and CST studio (CST AG, Darmstadt, Germany) employing the FITD method. Upon conforming near-field energy coupling efficiency, a series of

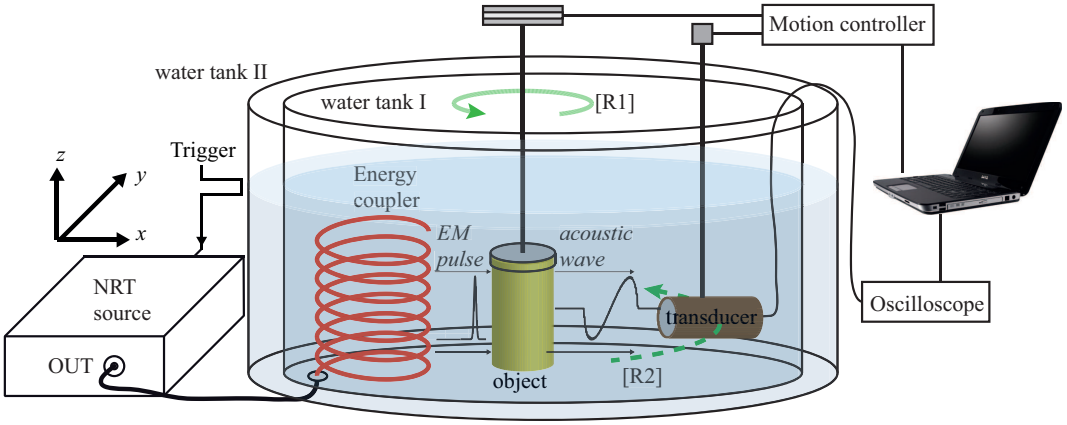

Figure 5.8: Schematic diagram of the experimental near-field radiofrequency thermoacoustic (NRT) tomography setup; [R1] - rotation of the object; [R2] - rotation of the transducer

different phantom measurements were conducted in order to evaluate the performance of the NRT approach. The first NRT experiments were performed on high-absorbing copper wires which exhibit significant RF-absorption. The copper wires had a diameter of ~ 100 µm and were employed to determine the resolution of the system.
The next generation of phantoms consisted of tubes filled with saline solution, intended to mimic soft biological tissue. The third generation of phantoms was comprised of a complex heterogeneous combination of excised biological tissue with alternating absorption coefficients. Finally, the NRT method was tested on *ex-vivo* mice that underwent special treatment with high absorbing foreign body insertion to highlight the resolution characteristics of NRT.

5.3.6.1 Numerical simulation

Two different types of simulations were performed to evaluate the predicted performance of the NRT method. In the following, the results from the publication by Razansky et al. [101], relating to the FEM simulation, are presented before describing the results from the paper [57] which used a time domain solver to the Maxwell equations.

FEM-simulation
In a first simulation, the overall potential of the near-field energy deposition was examined on a simple geometry consisting of a quarter-wave monopole antenna with a length of $l = 8.3$ cm and a radius of 2 mm. The simulation parameters comprised furthermore an excitation of the monopole antenna at 100 MHz, matching the length of the monopole for quarter-wave harmonic excitation in water. The monopole was surrounded by a saline

medium with a conductivity of $\sigma = 0.5$ S m^{-1} and a relative permittivity of $\varepsilon_r = 77$. Figure 5.9a shows the power density in dependence of the normalized radial distance from the $\lambda/4$ monopole on a decibel scale. Most of the power is dissipated within the close vicinity of the monopole. A more qualitative result can be obtained by estimating the effective volume where most of the energy is dissipated. Figure 5.9b plots the cumulated amount of absorbed electric power density which is integrated over an infinitely long cylindrical volume of radius ρ. More than 50% of the power is dissipated within a radius of ~ 11 cm and $\sim 40\%$ is dissipated within the radius which is equal to the monopole length.

It has to be noted that these results were obtained for the specific case of single

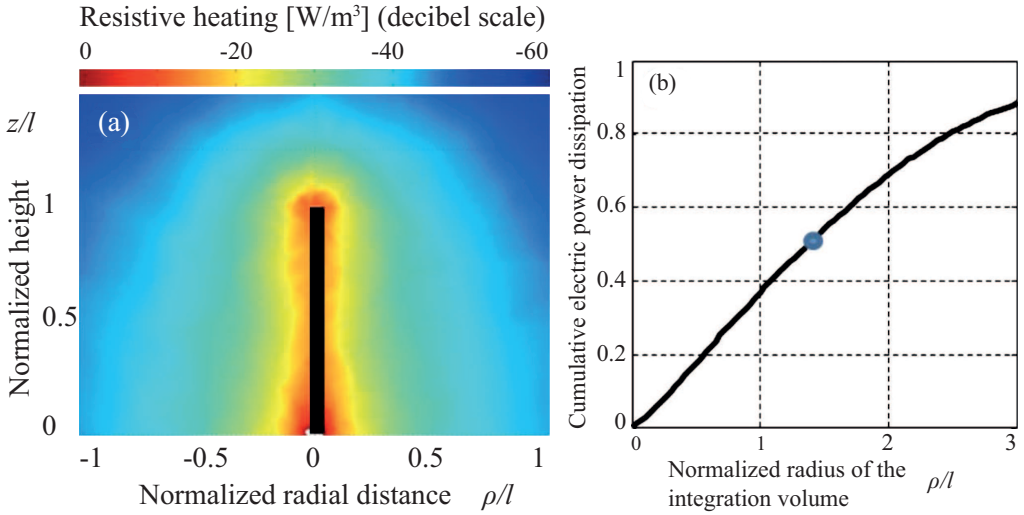

(a) Resistive heating $10log_{10}\left(\sigma\left|\vec{E}\right|^2\right)$ (power absorption density) of a monopole in dependence of the radial distance from the center of the monopole

(b) Volumetric electric power dissipation around the antenna, normalized to the total transmitted power of the antenna; marker highlights 50% absorption within the close vicinity of the monopole

Figure 5.9: Simulation results from a $\lambda/4$ monopole obtained with COMSOL (taken from [101])

frequency excitation at 100 MHz using a quarter wave monopole. Moreover, the impulse duration differs in the publication by Razansky et al. [101] from the excitation profile described in publication [57]. The monopole configuration was only implemented in this preliminary setup and was only used for one phantom measurement comprised of saline tubes.

As discussed earlier, small animal imaging and phantom experiments were performed with a helical antenna which is presented later on. However, although a single resonant monopole is not the ideal choice for efficient energy coupling due to its narrowband

frequency response, these simulations serve as a proof-of-principle of the NRT method and should in the first place demonstrate the power dissipation of radiating elements as a function of distance from the element.

FITD simulation

The power deposition was furthermore examined with a time domain solver, using Computer Simulation Technology. In contrary to the previous simulation, the whole NRT setup from figure 5.8 was modeled, including the sample which had a cylindrical shape ($\varnothing$: 2 cm, length: 10 cm) and tissue properties of $\sigma = 0.8$ S m^{-1} and $\varepsilon_r = 100$, simulating EM properties of biological tissue at 10 MHz [36]. The helical antenna was approximated with a diameter of 3 cm and seven turns. In order to evaluate the effect of grounded conductive parts (e.g. the transducer) on the electric field distribution, a conductive element in the size of the transducer was modeled next to the sample. Furthermore, the custom made water tank comprised of two cylinders was taken into consideration in the simulation. Similar to the setup, the outer cylinder was simulated with a water saline concentration at 0.2% while the inner container was filled with deionized water. As described in [57], the outer layer of the water tank had the effect of an absorbing layer terminating the electric field and minimizing reflections on the water - air interface.

The time domain simulation was carried out with the finite-integration time-domain (FITD) method which is based on the discretization of Maxwell's equations in its integral shape [119], [80].

The measured electric impulse from figure 5.7 was utilized to drive the simulation. The instantaneous power deposition in the imaging tank is shown in figure 5.10 at different time positions starting from 30 ns after initiation of the pulse and demonstrates resistive heating in 10 ns time steps. During the time points 40 ns to 60 ns, a maximum peak of power deposition appears which corresponds to the 20 ns duration of the electric pulse. At time point 90 ns, a second excitation is taking place due to electric field reflections on the water - air interface and also because of the finite response of the antenna. However, the power deposition is several times smaller than the main excitation. Note that the conductive part which is represented by a metallic transducer has negligible impact on the electric field distribution [57].

5.3.6.2 Spatial resolution of the NRT system

The following section presents experimental results obtained with the NRT system. Before showing NRT images of soft tissues, the performance of the system is characterized

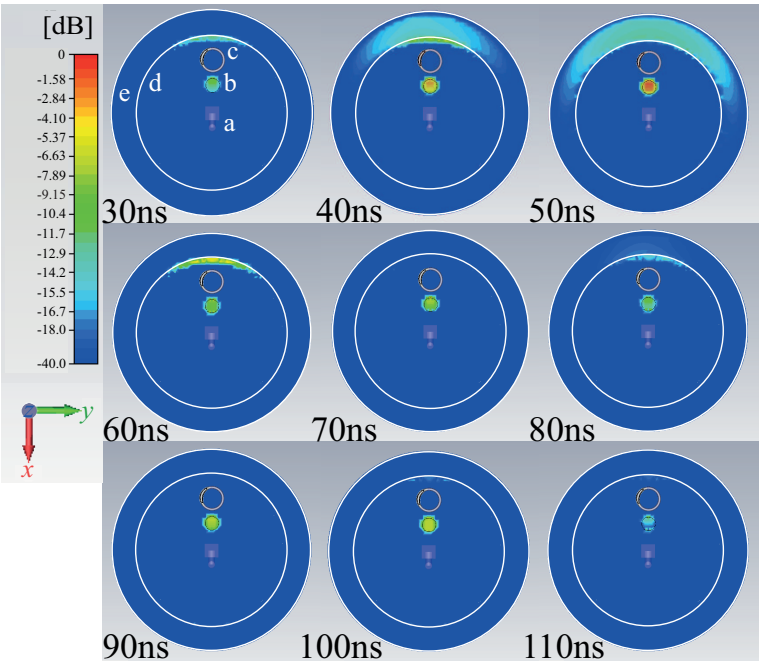

Figure 5.10: Imaging tank consisting of two containers showing the normalized distribution of instantaneous power deposition at 9 distinct time points; (a) acoustic detector; (b) object; (c) helical energy coupler; (d) inner imaging tank containing deionized water; (e) outer tank containing 0.2% saline

in terms of spatial resolution, measuring thin copper wires.

In 3D space, the spatial resolution in ultrasound applications can be separated into axial, lateral and elevational components. Figure 5.11 depicts the individual resolution constituents. The axial resolution defines the ability to distinguish between two point spread functions along the ultrasound beam. On the other hand, the lateral resolution determines the capability to resolve two point spread functions in perpendicular direction to the ultrasound beam. For the three dimensional case, the elevational resolution is a factor for the slice thickness.
This thesis focuses on cross sectional images which render a 2D view of samples, thus the elevational resolution, relevant in 3D applications, is not considered here. Furthermore, the images were acquired in a non limited view tomographic topology. Thus, the spatial resolution can be calculated according to equation

$$R_{sp} = 0.92\frac{v_s}{f_c} = \lambda 0.92 \tag{5.13}$$

with the cutoff frequency f_c defined by the transducer bandwidth [124].

From an experimental perspective, the resolution of the developed system can be determined with two point like absorbers consisting of thin copper wires. Therefore, two wires

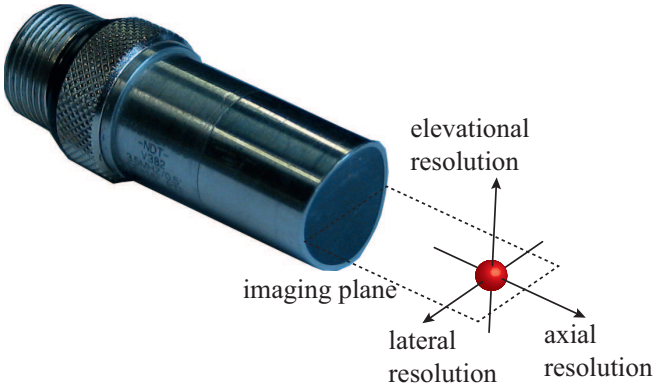

Figure 5.11: Resolution constituents in 3D space: axial resolution is along the imaging plane while the elevational resolution is perpendicular to the imaging plane; the lateral resolution is in the imaging plane parallel to the sensitive area of the detector

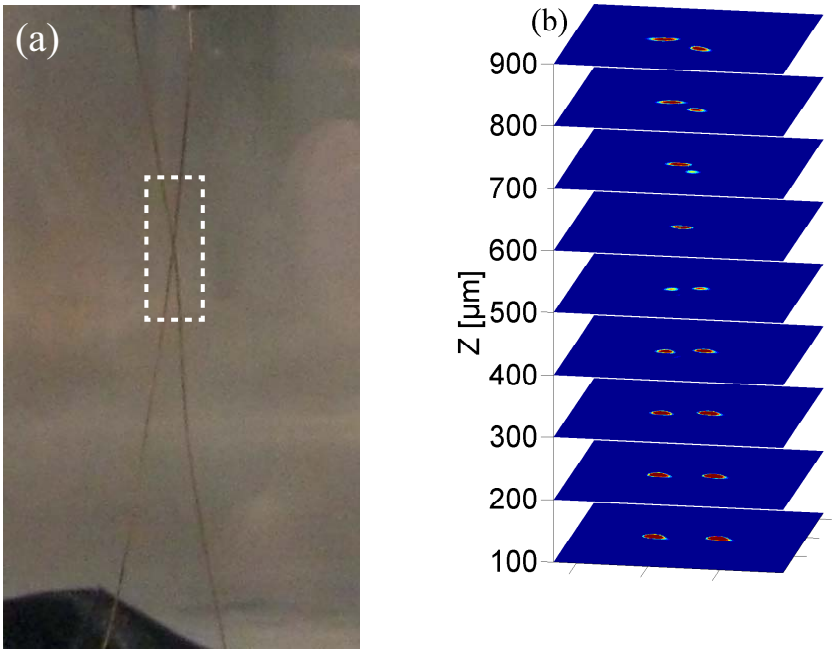

(a) Photograph from the X-shaped wires

(b) NRT reconstruction of the highlighted area, marking the crossing of two copper wires in (a)

Figure 5.12: Resolution experiment with two X-shaped copper wires

with a diameter of 100 µm were aligned in a X-shape that allowed for exact determination of the resolution of the system. During imaging, the wires were scanned in the elevational axis at 100 µm distance, acquiring in total 9 slices at the point where the two wires formed a crossing. Taking into account the size of the wires and the excitation frequencies of the electromagnetic pulse, a 7.5 MHz (transducer #2 from table 5.1) was chosen for imag-

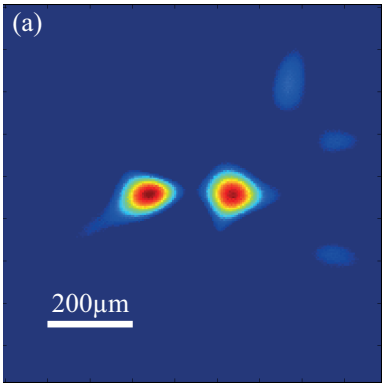

(a) NRT reconstruction at position $z = 500$ µm from figure 5.12b

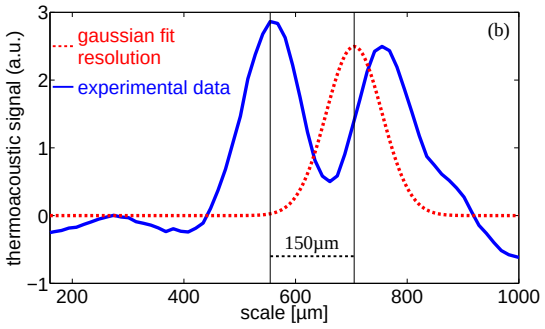

(b) one dimensional cut through the reconstruction 5.13a for evaluation of in-plane resolution; solid line - experimental data; dashed line - gaussian fit onto data

Figure 5.13: Resolution results from two X-shaped copper wires

ing. The wires were scanned in full tomography mode, resulting in 180 projections with $\phi = 2^\circ$ circular step size.

Figure 5.12a showcases the geometrical layout of the two copper wires with the highlighted area marking the imaging region. The NRT reconstructions at 9 imaging levels on the elevational axis are depicted in figure 5.12b, revealing the correct orientation of the wires in the imaging plane. The spatial resolution was determined by plotting the one dimensional profile through the NRT reconstruction at $z = 500$ µm, approximately at the position where both wires were crossing (see figure 5.13b). According to the Rayleigh criterion, the resolution is defined as the coincidence of the maximum of the first PSF with the minimum of the second PSF [8], [57]. With the gaussian overlay onto the experimental data set, the spatial resolution was measured to 150 µm, being in correspondence with the numerical resolution according to equation 5.13.

5.3.6.3 NRT with tissue mimicking phantoms

This section presents the experimental results from soft tissue that were obtained with the NRT method. All results are based on the publications by Razansky et al. [101] and Kellnberger et al. [57]. Except the first phantom which was measured with a monopole configuration, all NRT experiments shown in the following were carried out with the helical shaped energy coupler as depicted in the NRT setup 5.8. In order to evaluate the performance of the thermoacoustic system, different phantoms were prepared with varying absorption characteristics and geometrical layout to investigate factors like imaging contrast, penetration depth for deep tissue imaging and the capability to image a heterogeneous compound of biological tissues as a preparation measurement towards

small animal imaging.

Starting with a basic experiment, a homogeneous phantom which consisted of saline filled tubes was built. This fundamental approach should demonstrate the overall capability of the NRT method to image tissue mimicking phantoms. In a next step, the contrast mechanism of NRT was tested on two tubes which were filled with low absorbing mineral oil and high absorbing saline solution. With respect to the assumed deep penetration potential of the radiofrequency driven NRT method, a study was prepared which compared two different phantoms comprised of an absorbing saline tube embedded within either a low or high absorbing bigger tube. In a last experiment, a phantom composed of a heterogeneous distribution of biological tissues, exhibiting different RF absorption, was tested in the NRT setup.

Saline filled PVC tubes

The first phantom experiments were carried out on 4 low RF absorbing PVC tubes filled with physiological saline solution. In parallel to the experiment, the electromagnetic power absorption density was simulated assuming a quarter wave monopole which is excited at 100 MHz. Figure 5.14a shows the simulated resistive heating in the close environment of the monopole where most of the electromagnetic energy is concentrated within the 4 tubes. This can be attributed to the high conductivity of the saline containing straws in comparison to the low conducting deionized water which was used as an acoustic coupling medium. Another important aspect which can be observed from the simulation is that the energy density in the tubes is constant and not varying with distance from the monopole or more importantly with distance from the boundaries of the straw. In other words, according to the simulation the energy absorption is constant over the width of the PVC-tubes.

Similar to the simulation geometry, the NRT measurement was performed by rotating the tubes over 360°, acquiring the thermoacoustic signal over 180 projections each 2°. The corresponding reconstruction is depicted in figure 5.14b and reveals the correct size and dimensions of the tubes. The tubing walls due to their non-conductive nature appear as black-colored rings whereas the saline solution in the tubes is reconstructed as white hotspots. In [101], we attributed the non uniform signals to uneven mixed saline solutions in the tubes, tomographic rotation artifacts or limited detection bandwidth of the transducer (for the measurements, transducer #1 from table 5.1 was used).

Additionally, figure 5.14c plots the thermoacoustic signal from one specific projection of the tomographic data set. Clearly, the phantom signal from the saline filled PVC tubes is resolved while also the electromagnetic interference originating from the impulse

generator can be observed. This interference is coupled into the transducer at the point of triggering and lasts for ~ 5 µs due to relaxation of the transducer.

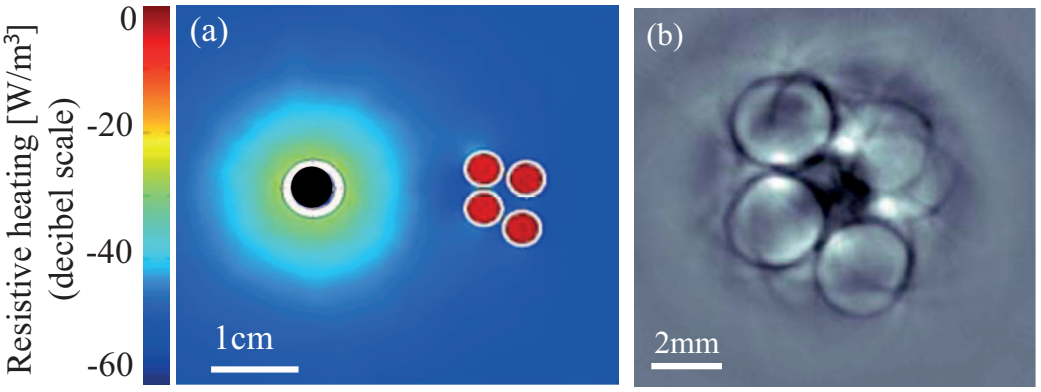

(a) Simulation showing the absorbed energy density distribution using a quarter wave monopole for excitation

(b) Corresponding measurement showing the NRT reconstruction of four tubes after 360° data acquisition

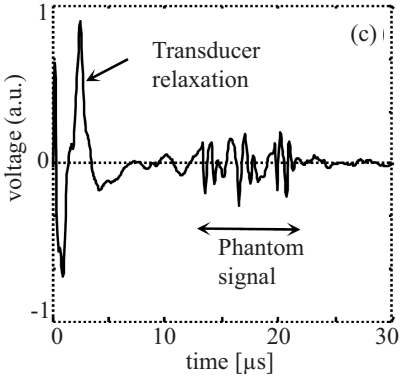

(c) Example of the time domain thermoacoustic response from 4 saline tubes as depicted in figure 5.14a

Figure 5.14: NRT simulation result, image and a schematic representation of the detected thermoacoustic signal from PVC tubes containing a 0.9% saline solution using the quarter wave monopole for excitation (taken from [101])

NRT contrast

The following study evaluates the NRT performance in terms of imaging contrast. Referring back to chapter 2, absorption in soft tissue is attributed to regions of high conductivity. More specifically, according to section 2.3.3.4, muscle tissue turns out to have a 14 times higher conductivity as compared to adipose tissue at frequency $f_{RF} = 100$ MHz.

The following phantom study consisted of two tubes which were filled with a low absorbing mineral oil solution (M8410, Sigma Aldrich, St Louis, MO, USA) and a high absorbing physiological saline solution. The geometrical layout of the phantom is shown in figure 5.15. Observing the NRT image, only the high absorbing saline tube can be reconstructed whereas the second tube does not show up due to the low thermoacoustic signal from the non-conducting mineral oil. The image also appears with a strong signal from the boundaries of the tube whereas the interior is not resolved clearly. The tubing walls, corresponding to the deionized water - saline interface, represent a high frequency thermoacoustic signal in contrast to the center of the tube which is comprised of low frequent signal components which are filtered by the high pass filter and the limited detection bandwidth of the transducer (transducer #1 with a center frequency of $f = 3.5$ MHz). Additionally, a polarization effect is occurring at the tubing walls since the liquid inside the tubes is charged.

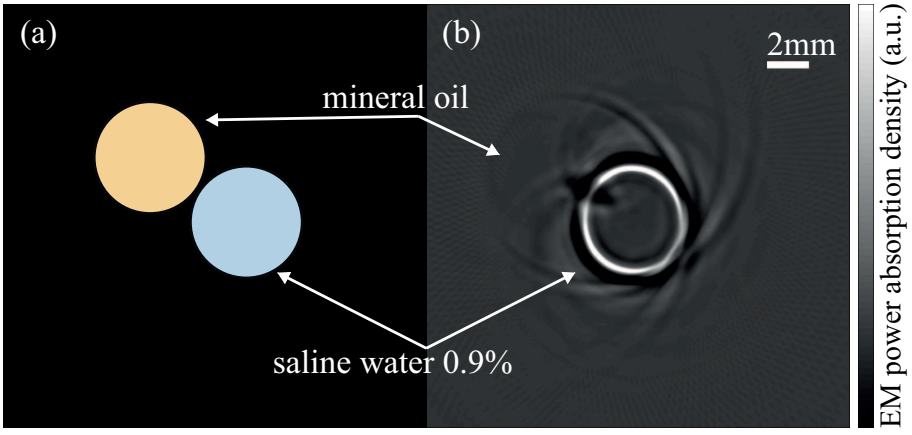

Figure 5.15: NRT imaging experiment showing two PVC tubes filled with low RF absorbing mineral oil and high RF absorbing 0.9% saline solution; (a) chart of the phantom layout; (b) NRT image of (a)

NRT penetration capabilities

The penetration depth capability was tested on two phantoms consisting of a bigger tube which contained a smaller tube with a defined RF absorption. The outer tube ($\varnothing$ 65 mm) of the first phantom was filled with low absorbing mineral oil whereas the second phantom with similar dimension was filled with an absorbing saline water solution at 0.1% concentration. A straw with a diameter $\varnothing$ 5 mm was embedded in both tubes containing a physiological saline solution (0.9%). The right hand side in figure 5.16 depicts the layout of the phantoms with the low absorbing tube on the top and the higher absorbing object at the bottom.

Similar to the previous phantom measurement, the mineral oil does not provide ther-

moacoustic contrast and therefore does not show up in the image. The insertion in the first phantom is resolved clearly and renders the dimension of the straw. Again, low frequencies are filtered by the high pass filter and the limited detection of the transducer (transducer #1 with central frequency of $f = 3.5$ MHz) which effectively measures frequencies down to $f \sim 1$ MHz.

The second phantom featured a higher absorbing outer tube which attenuated the penetrating electric field. Observing the reconstruction in figure 5.16, the outer tube with the low absorbing liquid and the inner tube with the high absorbing physiological saline solution are resolved in the NRT image. The strong signal from the boundaries of the objects can be ascribed to the afore mentioned limited detection bandwidth and frequency filtering.

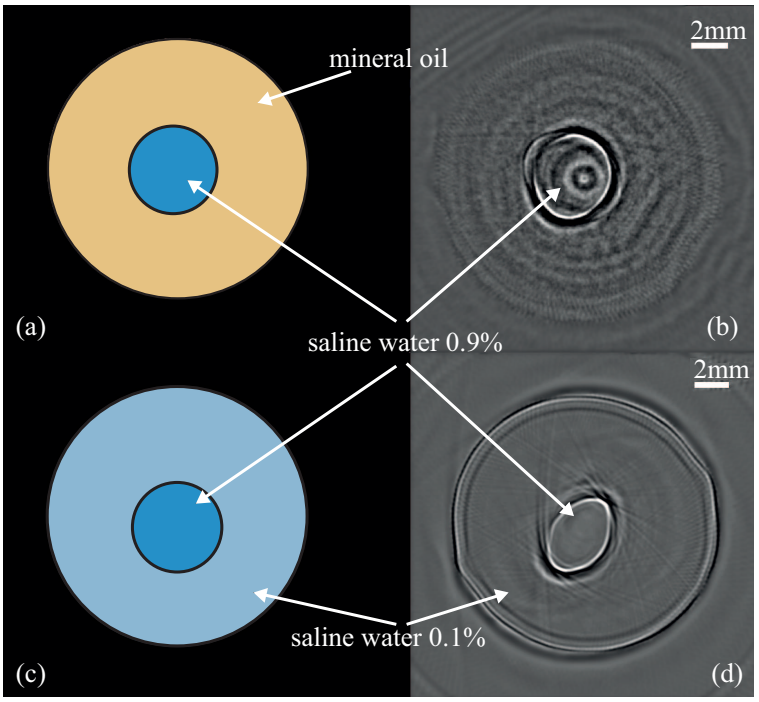

Figure 5.16: NRT images along with a sketch of absorbing objects embedded in non absorbing and low absorbing media: (a) Cross sectional view of a phantom comprised of a mineral oil tube containing a 0.9% saline tube with a diameter of ⌀ 5 mm; (b) corresponding NRT image of (a); (c) cross sectional view of a phantom consisting of a big 0.1% saline tube containing a 0.9% saline tube (⌀ 5 mm); (d) corresponding NRT image of (c)

Biological tissue

Before proceeding towards *ex-vivo* small animal imaging, the performance of the NRT system was tested on a phantom which was comprised of heterogeneously distributed biological tissues. With respect to the expected frequency components of the thermoacoustic

signal, transducer #1 with a central frequency of 3.5 MHz was used for the measurements. Figure 5.17 showcases the layout of the phantom which consisted of two layers of biological tissue, namely pork fat and chicken meat, and a highly absorbing saline water tube insertion with a dimension of $\varnothing\,3$ mm. The whole phantom was wrapped in an isolating low RF absorbing foil to preserve the absorption characteristics of chicken meat. Similar measurements demonstrated a degrading of the thermoacoustic signal over time when excised biological tissue like muscle was exposed to deionized water.
After preparation of the phantom, NRT imaging was initiated by rotating the object in the imaging tank and subsequently reconstructing the image shown on the right hand side of figure 5.17. The resulting NRT image resolves the transition from the low absorbing fat component to the higher absorbing chicken meat. Furthermore, the saline tube embedded in the center of the phantom is resolved along with artifacts which are contributed to acoustic mismatching of the PVC tube ($v_s \approx 2380$ m s^{-1}) to the peripheral soft tissue ($v_s \approx 1500$ m s^{-1}).

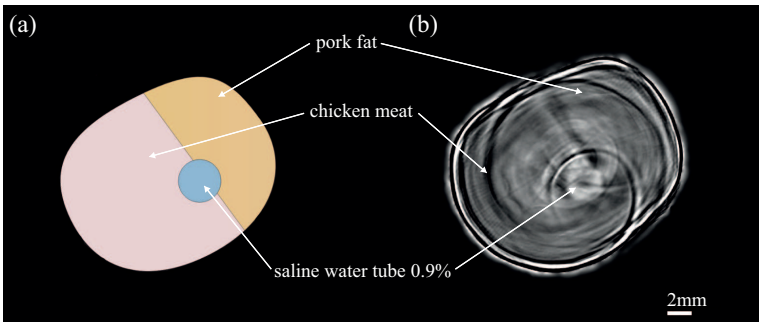

Figure 5.17: NRT image of biological tissue: (a) cross sectional view of a heterogeneous phantom consisting of chicken meat, pork fat and 0.9% saline tube; (b) corresponding NRT image of (a)

5.3.6.4 *Ex-vivo* small animal imaging with NRT

The final step includes imaging of an *ex-vivo* mouse. Hence, a nude mouse was prepared for near-field thermoacoustic imaging using transducer #1 from table 5.1. Post-mortem, the mouse received special treatment prior to the experiment. A highly dissipating copper wire ($\varnothing\,230\,\mu$m) was inserted subcutaneously in the back of the mouse to obtain a known reference in the NRT reconstructions. The mouse was then measured at the pelvic region and subsequently after the first measurement, the copper wire was removed. A second NRT measurement was initiated at the same imaging level without the copper wire. After the NRT experiment, the mouse was frozen to $-80\,^{\circ}$C, cryosliced and photographed at the pelvic region for comparison of the thermoacoustic images.

Figure 5.18 shows the results of the *ex-vivo* mouse measurement. The image on the left hand side corresponds to the measurement with the wire inserted into the back of the mouse. Clearly, the dissipative copper wire is highlighted in the image with high contrast. Furthermore, anatomical details like the spinal cord or the hindlimb are also visible. Removing the copper wire yields the NRT image shown on the right hand side. This time, more anatomical details are appearing like the urinary bladder and again the hindlimb and spinal cord. The fact that the copper wire features significant absorption in comparison to the lower absorbing soft tissue leads to the low contrast from soft tissues in the image where the copper wire is present. For comparison, the cryoslice image shown in the center of figure 5.18 shows good correlation between the NRT images and the histological slice.

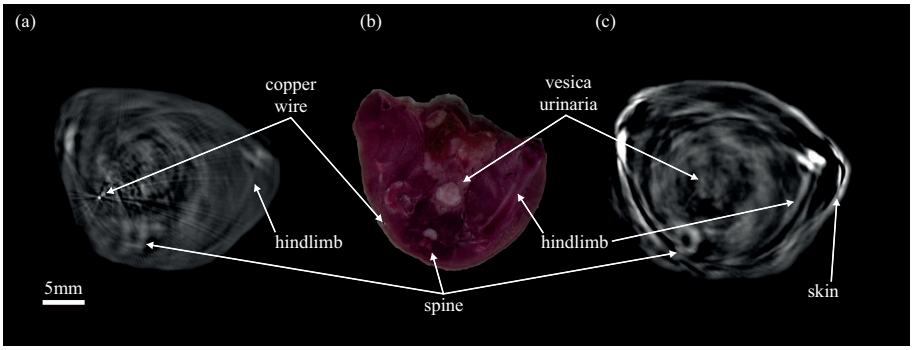

Figure 5.18: *Ex-vivo* mouse imaging with NRT. (a) Cross sectional view from an intact mouse with a subcutaneously inserted copper wire ($\varnothing$ 230 μm); (b) cryosection of the mouse at approximately the same level; (c) NRT mouse image after removing of the copper wire

5.4 Limitations to near-field radiofrequency thermoacoustic tomography approach

In the first place, the NRT method was developed to cross the resolution limits that are associated with conventional thermoacoustic approaches. But in addition to it, NRT should also be capable of resolving extrinsically administered RF energy absorbing probes in order to enhance thermoacoustic signals and contrast. In other words, the NRT method should not only be used for small animal anatomical imaging but at the same time be employed as a functional and molecular imaging tool. The physical rationale behind the idea is originated in the assumption that RF absorbers exhibit a broadband absorption profile. Among the candidates for RF probes could be paramagnetic and superparamagnetic nanoparticles which are already in use in MRI studies ([105], [114]) as well as

gadolinium-based agents. But also conductive particles like carbon nanotubes or gold nanoparticles are possible candidates especially with respect to the NRT contrast which is attributed to conductivity. As an example, Pramanik et al. [96] successfully applied single-walled carbon nanotubes in a thermoacoustic imaging system, demonstrating a twofold signal enhancement.

The NRT measurements presented in this chapter demonstrated the NRT capabilities when it comes to superior resolution compared to other thermoacoustic systems and showed for the first time thermoacoustic images of a mouse at high resolution. The first demand, namely high resolution thermoacoustic imaging, can be fulfilled with the NRT method.
However, the molecular imaging functionality of the NRT method has not been achieved yet. The physical rationale behind NRT to operate as an anatomical *and* functional/molecular imaging tool is based on the assumption that the proposed paramagnetic and superparamagnetic agents exhibit strong RF absorption. The problem is twofold:

1. Magnetic particles dissipate power when exposed to a CW alternating magnetic field [107], [47]. This power absorption is converted into heat through relaxation processes as explained in chapter 2.
2. The NRT method is operating in pulsed mode with duty cycles $< 0.001\%$; thus, the time interval during which energy is deposited in the agent is in the range of ns. With its high voltage output of the nanosecond pulser, the near-field impulse system mainly generates strong electric fields with low magnetic field amplitudes. Thus, NRT is directed towards conductive/dielectric tissue contrast as discussed in chapter 2.

After all, NRT is ill-conditioned when it comes to excitation of magnetic nanoparticles with a pulsed electric source. Although one might argue that the energy per pulse is in the range of hundreds of mJoule, the overall average power is still limited to ~ 5 W. Moreover, magnetic particle excitation is primarily achieved by CW magnetic sources with a magnetic field strength beyond 10 k A m^{-1} [53], [134].
Several magnetic nanoparticles have been tested for acoustic signal generation with the system, the results were sobering. In summary it can be said that the NRT method does not provide higher thermoacoustic signal contrast in combination with magnetic nanoparticles.

5.5 Summary and outlook

This chapter presented a new approach towards thermoacoustic signal generation which is based on ultrashort electric impulses operating in the near-field of an energy transmitting element. Unlike conventional approaches, the sample is not excited with pulse modulated CW sources but instead with a dedicated nanosecond pulse generator, producing ultrashort high voltage pulses. In combination with a custom-built tomography system, the performance of this prototype technology was characterized firstly on copper wires to determine the resolution and later on liquid phantoms and soft biological tissue. Especially with respect to the outstanding resolution that could be achieved with the system, an *ex-vivo* mouse was prepared for NRT measurements. Therefore, NRT images were made while a highly dissipative medium was inserted subcutaneously in the mouse ensued by another measurement after removing the medium. The NRT imaging results confirmed the histological slice of the mouse and revealed a spatial resolution of ~ 230 µm for this specific measurement, however application of transducers with higher cut-off frequencies resulted in a spatial resolution of ~ 150 µm. With respect to the pulse duration of the excitation pulse which is in the order of ~ 20 ns, the resolution is mainly limited by the detection bandwidth of the transducers.

Referring to future steps, a new generation of NRT imaging was recently introduced by Omar et al. [89] [90]. Instead of capacitors, a transmission line is used to store electromagnetic energy before discharging it into the sample. Several advantages come along with this approach: Since the energy and pulse shape is dependent on the length of the transmission line, both electromagnetic energy and pulse duration can be adjusted by changing the length of the lines. Thus, the excited frequencies and amount of energies can be accommodated accurately to the size of the object. The prototype version presented high quality images of *ex-vivo* mice while exhibiting outstanding spatial resolution in the order of ~ 100 µm.

After all, the NRT method is a powerful imaging tool to perform anatomical small animal imaging with RF excitation. However, the system is limited in terms of functional and molecular imaging since no appropriate contrast enhancers could be found. The problems are associated with the NRT specific excitation profile which allows for ultrashort pulse stimulation with strong electric fields, ideal for high resolution imaging combined with conductive/dielectric contrast. At the same time, the optimal operation condition for magnetic particles relates to a CW alternating magnetic field at high frequencies. Considering the magnetic heating of nanoparticles when exposed to CW fields, a new

approach to thermoacoustic signal generation is investigated and will be explained in the following chapters.

6 Frequency domain optoacoustic tomography

6.1 Introduction

Frequency domain optoacoustic imaging (FD-OAI) or tomography (FD-OAT) represents a new diagnosis tool in the field of optoacoustic imaging. Whereas pulsed optoacoustics has been implemented in numerous applications ranging from three dimensional whole body imaging of small animals [13] to microscopic applications [126] while recently also entering the stage of pre-clinical research [99], FD-optoacoustics is at the beginning of a similar evolutionary process.

This chapter discusses the frequency domain optoacoustic tomography scanner which was developed at the IBMI. Section 6.2 presents state of the art FD-optoacoustic imaging systems which are based on linear *x*-*y* scans. The focus of this chapter directs the reader towards the novel tomographic implementation of frequency domain optoacoustics by first showing the experimental setup in section 6.3 before proceeding to the results in section 6.4. The performance of the developed tomographic scanner was tested on non-biological tissue, agar phantoms and finally *in-vivo*, imaging the mouse tail following contrast enhancing ICG (Indocyanine Green) injection.

6.2 Frequency domain optoacoustic implementations

Before starting with the instrumentation employed for frequency domain imaging, initial concepts will be presented followed by contemporary arts in frequency domain optoacoustic imaging. These systems are shortly described to outline the particular difference between existing frequency domain implementations and the developed tomographic approach.

6.2.1 Thermoacoustic microscope

Dated back to the year 1981, Allan Rosencwaig was among the first to describe an implementation of an imaging system based on the photoacoustic effect. The thermoacoustic microscope, patented in [106], characterizes an imaging system on a microscopic scale employing electromagnetic radiation across the whole spectrum, covering both heating of tissue with low frequent electromagnetic radiation (e.g. RF or microwaves) and visible light. Imaging is achieved on a horizontal plane, scanning the surface of the object with a radiation beam and measuring the subsequent acoustic response. The source can be intensity modulated, equivalent to the frequency domain optoacoustic approach, but also time domain thermoacoustic signal generation employing pulsed sources is mentioned. Note that the term thermoacoustics in this case covers both optoacoustic and thermoacoustic methods with respect to the conversion of electromagnetic energy into thermal energy.

6.2.2 Frequency domain sub surface optoacoustic imaging

The first documented technical implementation of a frequency domain optoacoustic scanner with experiments on non-biological samples can be attributed to Fan and Mandelis et al. in the publication [30]. Although theoretical considerations on photoacoustic signal generation in frequency domain were reported before [106], this highly original approach presented the first frequency domain based images using heterodyned detection. The sample was illuminated with a CW ytterbium fiber laser at 1064 nm. Intensity modulation of the laser beam induced acoustic signals from the illuminated spot. Therefore, an acousto-optic modulator (AOM) was introduced in the light path and externally driven by a function generator in the frequency band $1.2 - 3$ MHz with a discrete step size of 50 kHz. Scanning was performed on several points on the sample's surface, repeating the discrete frequency sweep for five times per scanning location. With respect to the heterodyned modulation and lock in detection type, the resulting amplitude and phase image could resolve the boundaries of a rubber phantom. However, the presented images with this preliminary scanner were restricted to non biological tissue and demonstrated a single 2D scan without tomographic cross sectional views of the sample.

6.2.3 Frequency domain photothermoacoustic imaging

Subsequent systems building up on the preceding implementation were also employed for biological soft tissue imaging. In a publication by Telenkov and Mandelis [120],

in addition to the heterodyned lock in detection, the pulse compression method from radar engineering [116] was introduced for subsurface imaging. Similar to the system explained in [30], a CW laser at 1064 nm was employed to excite acoustic responses from tissue. Therefore, an acousto-optic modulator intensity-coded the optical beam using a linear frequency sweep from $1-5$ MHz. An additional delay generator synchronized the AOM driving signal generator and the data acquisition. Imaging was performed on the basis of *x-y* scans, moving the water container which contained the phantom while the laser beam and the acoustic detector took fixed positions. The scanner was able to display depth profilometric images showing structures of turbid plastisol phantoms. In addition, *ex-vivo* chicken breast tissue was imaged with the proposed scanner, revealing embedded inclusions in the tissue as deep as 7 mm.

Similar to the preceding application, an improved system was presented in papers by Telenkov and Mandelis et al. [123] and Telenkov and Mandelis [121]. In the latter publication, the system from [120] was modified so that the sample, consisting of tissue mimicking phantoms, could be moved on the axial direction relatively to the excitation and detection. Thus, the maximum depth of the system could be characterized. In addition, time domain measurements were performed and compared to the frequency domain experiments, showing comparable results in terms of depth sensitivity. However, the scanner's performance was limited to lateral *x-y* scans and could not be employed for tomographic approaches.

6.3 FD OAT - instrumentation

This section discusses a novel optoacoustic imaging system which implemented tomography principles in the frequency domain employing an intensity coded CW light source. Previous FD optoacoustic methods were designed for horizontal *x-y* scans that collected optoacoustic signals by laterally moving the detector. A rotation of the detector with simultaneous signal acquisition at multiple projections results in cross sectional views of samples as compared to the depth profilometric images obtained with conventional FD-imaging systems.

A picture of the frequency domain optoacoustic tomography scanner is schematically depicted in figure 6.1. The sample is placed in the center of the imaging tank which is filled with deionized water. A temperature stabilized diode laser at 808 nm (Omicron-Laserage Laserprodukte GmbH, Germany) illuminates the object with an intensity coded

optical beam. The peak power is limited to 500 mW. A function generator (33210A, Agilent Technologies, Santa Clara, CA, USA) modulates the intensity of the laser beam at frequencies ranging from $0-10$ MHz. Although the laser can theoretically be modulated from $0-350$ MHz, with respect to the detection bandwidth of the transducer (transducer #1: center frequency 3.5 MHz from table 5.1) the modulation frequency exhibits a frequency sweep from $1-5$ MHz for phantom and *in-vivo* experiments. Induced acoustic waves are detected with one focused ultrasonic transducer. The detector and the optical fiber are mounted on a rotational stage (PR50PP, Newport Corporation, Irvine, CA, USA) which allows for simultaneous rotation of both units around the object. Optoacoustic signals are acquired every 2°, resulting in 180 projections over a full circle. For the cross correlation and recovery of the phase delay, the reference signal is acquired in two ways. A photodiode (DET10A/M, Thorlabs, Newton, NJ, USA) which is additionally mounted on the rotation stage detects concurrently a portion of the emitted modulated light. Furthermore, the driving signal from the function generator is acquired additionally by the oscilloscope (DPO7254, Tektronix Inc., Beaverton, OR, USA) which digitizes optoacoustic signals at a sampling rate of 50 MS/s. Acoustic signals are amplified before acquisition by a low noise 65 dB amplifier (Model AU-1291, Miteq, Hauppage, NY, USA). A trigger generator (MXG5181, Agilent, Santa Clara, CA, USA) synchronizes the function generator and the data acquisition system. A special custom made Matlab interface (Mathworks, Natick, MA, USA) facilitates data acquisition, positioning and post processing of the data.

Figure 6.2 shows a photograph of the experimental setup. Key elements are highlighted in the picture such as the directions of the optical beam and the acoustic waves, the simultaneous rotation direction of the transducer, the optical fiber and the photodetector, the mouse holder in the center of the imaging tank and the heating element which ensured constant temperature throughout the *in-vivo* experiments.

6.4 Imaging results

The frequency domain optoacoustic tomography method was evaluated on phantoms with different geometry and absorption characteristics. The overall capability of the frequency domain tomographic implementation was firstly tested on graphite rods which exhibit significant optical absorption. In a next step, more complex irregularly shaped agar phantoms with inclusions of defined optical absorption were prepared. The phantoms differed in size and aimed at evaluating the feasibility of vasculature imaging. Finally, the tail of

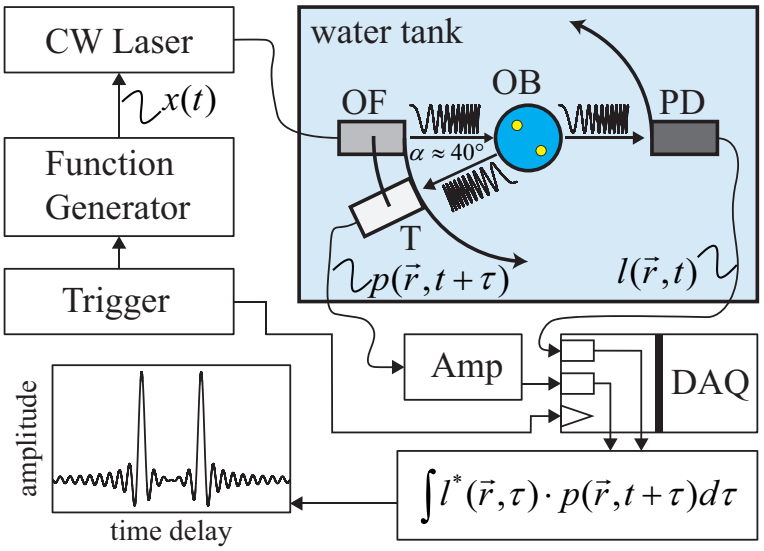

Figure 6.1: Schematic diagram of the frequency domain optoacoustic tomography scanner. An optical fiber (OF) guides the chirps from the laser onto the object (marked as OB). Signals from the transducer (T) and the photodetector (PD) are acquired simultaneously and cross correlated for spatial reconstruction of absorbers (taken from [59])

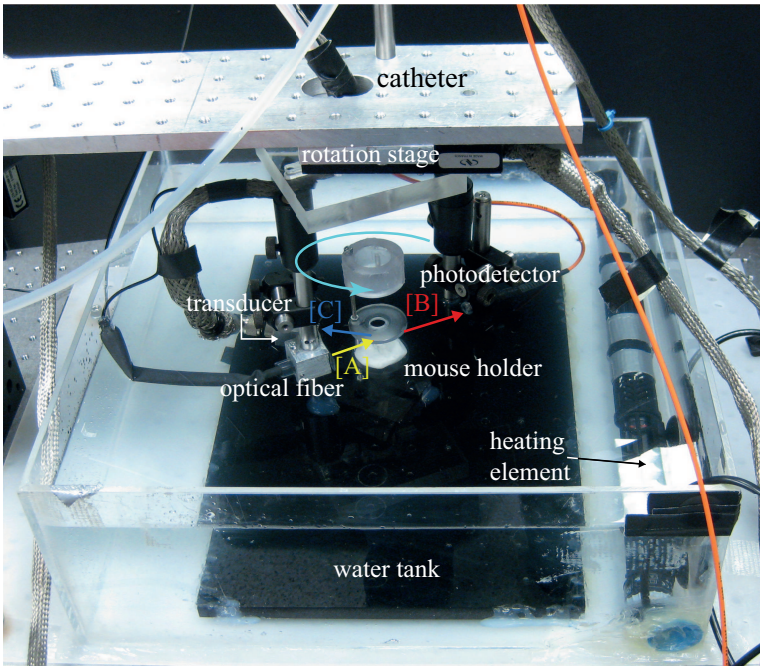

Figure 6.2: Photograph of the FD-OAT scanner, showing the imaging tank, the rotation stage and the mouse holder in the center of the tank; [A] laser beam from optical fiber; [B] reference beam detected by photodetector; [C] acoustic wave detected by transducer

a Balb/c female mouse was imaged *in-vivo* with the FD-OAT scanner before, during and after injection of contrast enhancing ICG.

6.4.1 Graphite rod imaging

In a first study, the proposed tomographic approach was tested on two graphite rods placed ~ 2 mm apart. Each rod had a diameter of 0.35 mm while both were mounted in the center of the imaging tank.

Figure 6.3 depicts a photograph of the experimental FD-OAT scanner which was used

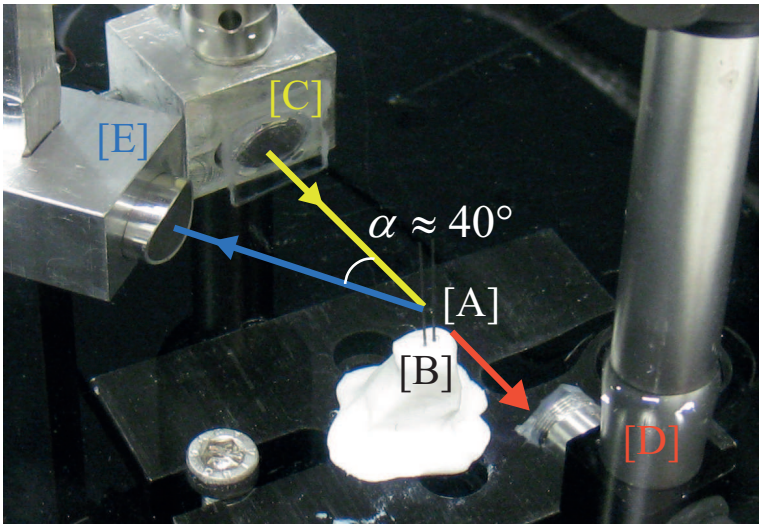

Figure 6.3: Experimental configuration of the FD-OAT scanner used for imaging of graphite rods; graphite rods [A] and [B], optical laser beam [C], photodetector beam [D] and ultrasonic 3.5 MHz transducer [E], $\angle[C]||[E] \approx 40^\circ$ (taken from [59])

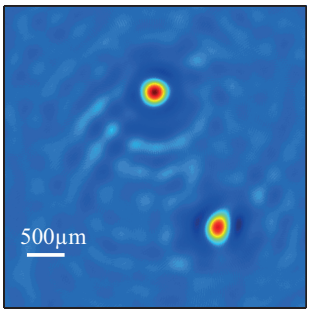

Figure 6.4: FD-OAT reconstruction showing a cross sectional cut through the phantom consisting of two graphite rods (taken from [59])

for evaluating the feasibility of implementing tomographic methods in the frequency domain. The end of the optical fiber [C] was connected to a collimating lens which created an illumination spot of $\sim \varnothing 5$ mm on the surface of the target. The graphite rods [A] and [B] were centered in the imaging tank and surrounded by the illumination and detection units. In this configuration, a photodiode [D] concurrently captured a portion of the laser beam which represented a copy of the modulation signal. Alike an

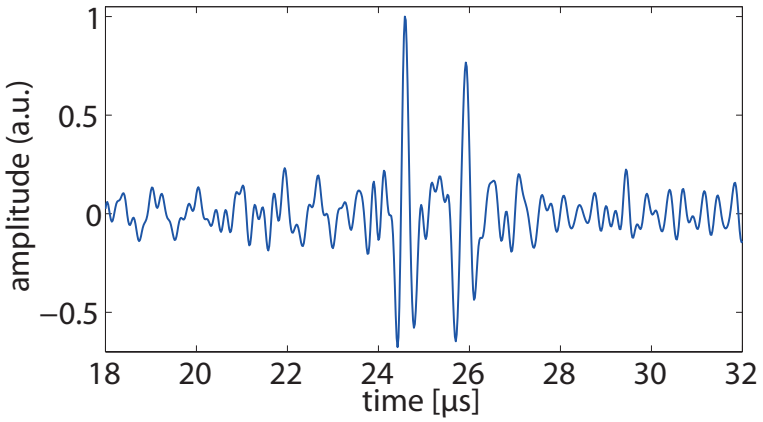

Figure 6.5: Cross correlation result of two graphite rods for one specific projection (taken from [59])

epi-illumination-detection scenario, the rods were illuminated by the laser beam while the transducer (central frequency: 3.5 MHz, marked as [E]), aligned to the optical beam, was focused onto the illumination spot in order to efficiently detect acoustic waves. Detection and illumination were simultaneously rotated around the objects in 2° steps, resulting in 180 projections.

The corresponding cross sectional view of the graphite rods is depicted in figure 6.4. The shape and size of the rods are clearly resolved. Additionally, the raw cross correlation signal which is used to feed the reconstruction algorithm is schematically shown in figure 6.5. The cross correlation result is taken from one specific projection of the tomographic data set which forms a line along the connection of the two objects relatively to the transducer. Comparing the measured signal after cross correlation processing with the simulation from chapter 4, figure 4.11, the experimental signal does not exhibit the characteristic sidelobes to the same extent as the simulation. Thus, the sidelobes are not distinguishable among noise.
In figure 6.5, each absorber represents one peak, exhibiting a duration defined by the bandwidth of the modulation signal. Although various methods for sidelobe reduction exist (e.g. Taylor weighting, Hamming weighting), frequency domain weighting functions were not applied with respect to the low sidelobe level and also with regard to the reduced SNR after weighting.

6.4.2 Phantom imaging

The frequency domain optoacoustic tomography system was furthermore employed for imaging of agar phantoms. Adding a more complex and irregular geometric structure

over the circular shaped graphite rods from the preceding section, the clear agar phantoms in the following section exhibited an outer diameter of ~ 4 mm and contained different absorbing structures made of India ink. A photograph of the first phantom is depicted in figure 6.6.

The rectangular shaped insertion had an absorption coefficient of ~ 2 cm^{-1} with a

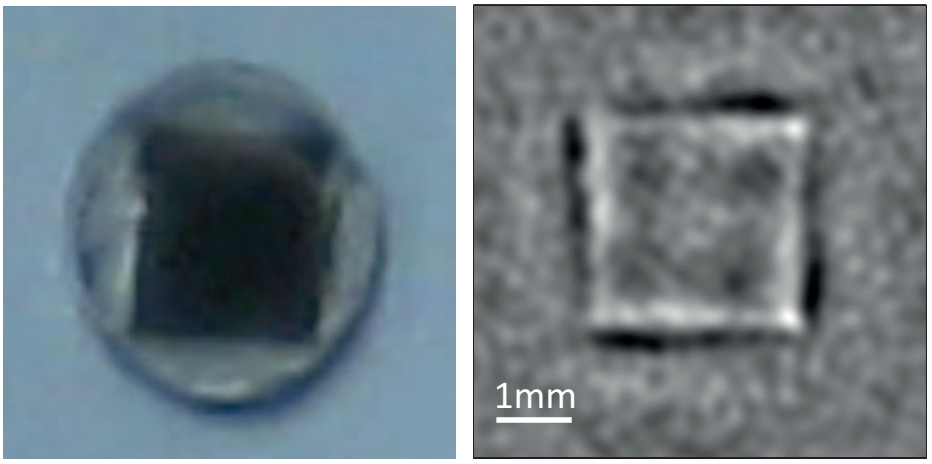

(a) Photograph of the clear agar phantom containing a 2 cm^{-1} India ínk absorption with a size of ~ 3 mm

(b) FD-OAT reconstruction from a 360° tomographic data set

Figure 6.6: FD-OAT phantom measurements: circular shaped clear agar phantom with defined optical absorption inclusion of rectangular shape (taken from [59])

characteristic side length of $l_{rect} \approx 3$ mm. The reconstruction of the cross correlated signal in figure 6.6b shows size and shape congruence to the picture of the phantom. The edges of the object are highlighted with respect to the high optical absorption of the inclusion; thus, most of the light is absorbed on the outer layer of the rectangular insertion. Furthermore, only the frequency band from $1-5$ MHz is excited while lower frequency components ($f < 1$ MHz) are not prominently stimulated by the modulation frequencies.

A similar phantom with a small hexagonal insertion instead of the rectangular shape was subsequently evaluated with the FD-OAT scanner. The size of the insertion was ~ 1 mm and had an absorption coefficient of 2 cm^{-1}. Figure 6.7a depicts a photograph with the layout of the phantom along with the reconstruction of the cross correlated signals in figure 6.7b. The reconstructed image is consistent in size and shape to the cross sectional photograph of the phantom.

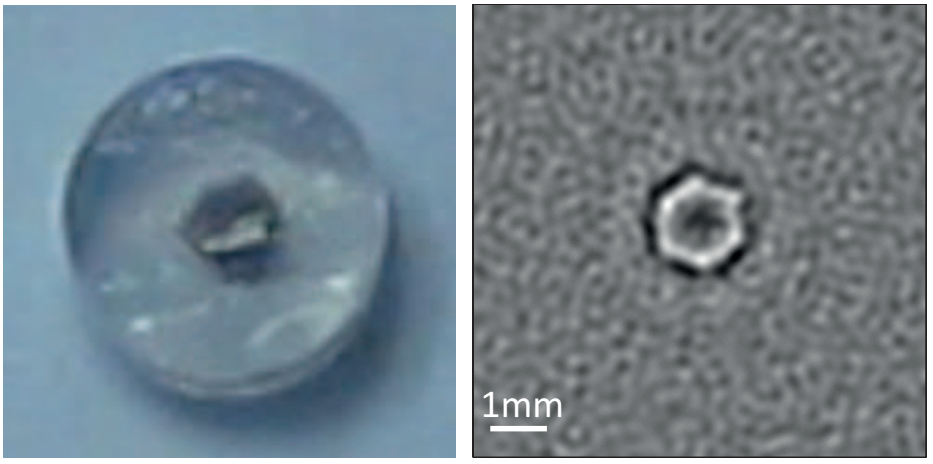

(a) Photograph of the clear agar phantom containing a 2 cm^{-1} India ink absorption with a size of $\sim$ 1 mm

(b) FD-OAT reconstruction from a 360° tomographic data set

Figure 6.7: FD-OAT phantom measurements: circular shaped clear agar phantom with defined optical absorption inclusion of hexagonal shape (taken from [59])

6.4.3 *In-vivo* mouse tail imaging

Upon confirming the feasibility of imaging small structures consisting of soft tissue, the next step included vasculature imaging in small animals. For this reason, a Balb/c female mouse was prepared for FD-OAT imaging. Since the illumination spot was confined to a size of $\sim$ 5 mm, only the mouse tail was imaged.
Picture 6.8 illustrates the FD-OAT scanner during imaging application. The mouse was placed on a custom built mouse holder which allowed for immobilizing the tail. The transducer was aligned to the optical beam onto the surface of the mouse tail to ensure efficient acoustic signal coupling. Both the transducer and the optical fiber casing were rotated around the tail while acoustic signals were simultaneously acquired at multiple projections.

The *in-vivo* measurement protocol consisted of mouse tail imaging (Balb/c female mouse) with mouse gas (isoflurane) anesthesia and catheterization of the right vein at $\sim$ 2 cm from the distal end prior to the measurement. After the mouse was attached to the mouse holder, the FD-OAT scanner imaged the tail at a level of $\sim$ 4 mm from the distal end without contrast enhancing ICG. Subsequent to the first measurement, 130 nmol of ICG was injected into the mouse tail via the catheter. Immediately after injection, the second measurement was initiated at the same imaging level. With respect to the long acquisition time of $\sim$ 10 min/image and to compensate for ICG clearance from

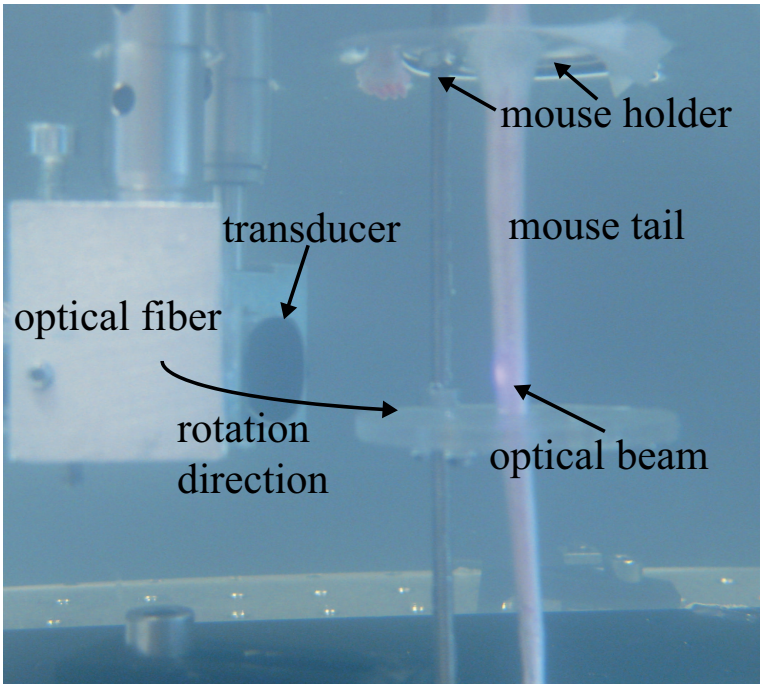

Figure 6.8: FD-OAT system during *in-vivo* mouse tail imaging

the blood stream through the hepatobiliary tract [16], [40], in addition to the initial ICG injection 100 nmol was administered at projection angle 140°, assuring ICG presence in the imaged mouse tail throughout the experiment. After the second measurement, a third FD-OAT measurement was initiated approximately 10 min from the initial ICG injection; thus, dynamic changes such as the clearance of ICG from the blood circulation were recorded. Following the *in-vivo* experiments, the mouse was euthanized and prepared for cryoslicing. Therefore, the mouse was frozen to −80°C, cryosliced and photographed for confirmation of the non-invasive FD optoacoustic images.

Figure 6.9 depicts the results of the experiment. Comparing the optoacoustic images with the *ex-vivo* picture in figure 6.9d shows the tail blood vessels such as the dorsal vein, the ventral caudal artery and the lateral caudal veins. Contrast enhancement following ICG injection is depicted in figure 6.9b, unfolding an absorption increase of almost a factor of 2. Signal to noise ratio in figure 6.9b is calculated to 49.6 dB. The result from the last measurement is showcased in figure 6.9c and reveals a contrast decrease at a scale in between the maximum observed from the ICG administration in figure 6.9b and the baseline from the tail image without ICG injection in figure 6.9a.

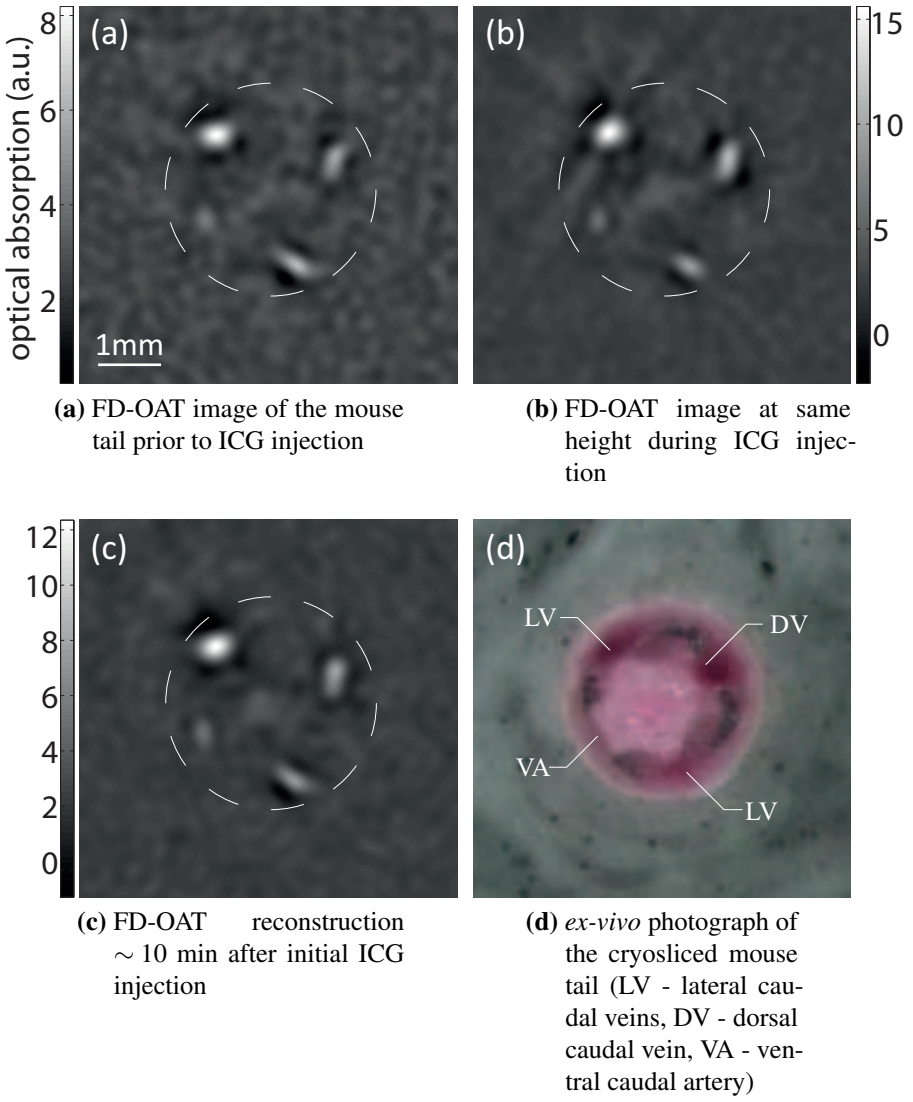

(a) FD-OAT image of the mouse tail prior to ICG injection

(b) FD-OAT image at same height during ICG injection

(c) FD-OAT reconstruction $\sim$ 10 min after initial ICG injection

(d) *ex-vivo* photograph of the cryosliced mouse tail (LV - lateral caudal veins, DV - dorsal caudal vein, VA - ventral caudal artery)

Figure 6.9: *In-vivo* frequency domain tomographic reconstructions of a mouse tail following ICG injection (dashed line represents approximate tissue surface) (taken from [59])

6.5 Summary and conclusive remarks

This chapter presented a novel implementation of frequency domain optoacoustics using a modulated CW light source. Instead of horizontal scans with limited view reconstructions, the FD-OAT scanner is able to perform tomographic data acquisition over 360°. In combination with pulse compression and cross correlation methods which yield the phase and correspondingly the time delay of absorbers within the imaging plane, FD-OAT can resolve the spatial distribution of multiple absorbers employing CW lasers. Cross sectional images are furthermore reconstructed by feeding the backprojection algorithm with the cross correlated functions, thus creating a tomographic map of optical absorbers.

Although imaging with the presented FD-OAT scanner is limited to small sized objects, a proper scaling of the optical beam to objects with larger dimensions would facilitate whole body imaging of small animals. Furthermore, the application of either one wavelength tunable CW laser or an array of multiple CW lasers which are simultaneously emitting at different wavelengths represents a topic of growing interest with respect to the wide application range of time domain multispectral imaging like MSOT [87].
The presented *in-vivo* mouse images exhibit a SNR of 49.6 dB after ICG injection. However, a detailed SNR comparison between the time domain optoacoustic method and the frequency domain implementation is in the scope of further research.

7 Quasi continuous wave thermoacoustics

7.1 Introduction

The term quasi CW refers to an intermediate state between the time domain and frequency domain. Quasi CW is characterized by ultralong pulses which are modulated at a narrowband frequency. The modulation is chosen to match the bandwidth of the detection elements, i.e. the acoustic transducers. While still exhibiting pulsed stimulation of tissue, in particular the narrowband acoustic response accounts for frequency domain characteristics, thus creating the term quasi CW thermoacoustic signal generation.
This chapter describes in section 7.2 the design considerations in combination with the hardware implementation for generation of quasi CW thermoacoustic signals. Based upon the simulations from chapter 3, section 3.4, preliminary experimental results from copper wires exhibiting strong absorption, absorbing liquids and finally excised *ex-vivo* biological tissue are presented. Section 7.4 completes the chapter, summarizing the results and discussing the quasi CW method.

7.2 Implementation of quasi CW

7.2.1 Design considerations

So far, the successful implementation of thermoacoustic methods in the frequency domain has not been documented. Although Ye reported on a CW modulated thermoacoustic system in his dissertation [131], the detection of thermoacoustic signals following narrowband excitation has not been achieved yet. This can be attributed to technical problems which are associated with the cross coupling between acoustic wave detection and electromagnetic interferences coming from the electromagnetic source. For example,

Ye employed a microwave generator operating at $f_{CW} = 407$ MHz which is down converted with a mixer to match the detection bandwidth of the ultrasonic transducers ([131]). Obviously, electromagnetic interferences strongly influence the PZT based transducers which make it difficult to distinguish between the electric excitation signal and the acoustic pressure wave. Nevertheless, Ye came to the conclusion that a better shielding of the detection path in combination with appropriate transducers could result in the successful detection of acoustic waves.

In order to accomplish the detection of acoustic pressure waves following narrow-band RF excitation, a distinct design has to be considered. The problem is twofold:

(1.) The detection has to be decoupled from the excitation.
(2.) The energy of the electromagnetic field has to be increased to yield distinguishable thermoacoustic signals among noise.

Referring back to time domain thermoacoustics in chapter 5, interferences can be separated from thermoacoustic signals through time of flight measurements. The acoustic signals are time delayed due to acoustic propagation while the electromagnetic (interference) signals are detected at the time point of triggering. Thus, the time gating of signals allows for temporal and accordingly spatial separation of distortions and thermoacoustic responses. Therefore, problem *(1.)* can be solved by employing a distinct time gating of signals.

The second issue faces again one of the main problems associated with RF-induced thermoacoustics. Inherently, RF struggles with limited focusing of energy due to the long wavelength. In order to deposit sufficient energy into samples, energy levels have to be raised which comes along with bulky and expensive hardware. Thus, frequency domain thermoacoustics using high power RF/microwave sources would end up in impractical hardware requirements not mentioning shielding aspects.

Taking these constraints into account, the generator which can be employed for induction of CW thermoacoustic signals should exhibit the following features:

- high signal to noise ratio
- time confined excitation
- narrowband stimulation pattern

In other words, the generator should provide an output exhibiting the characteristics of a pulse in order to facilitate a time gated detection of CW thermoacoustic signals (point *(1.)*) while still maintaining pulses of high energy to meet requirement *(2.)*. In addition to it, a narrowband modulation matching the detection bandwidth of the transducer is demanded. Based on these requirements, a modified "pulse" generator was designed which will be described in the next section.

7.2.2 Experimental setup for quasi CW thermoacoustic signal generation

Referring to the requirements from the preceding section, a prototype system based on the time domain pulse generator from chapter 5 has been built. The TD impulse generator was modified to allow for long pulses in the time scale of $t_{quasi\,CW} \sim 10$ µs. Additionally, pulse modulation to achieve narrowband stimulation is facilitated by introducing resonance elements in the quasi CW source.
Figure 7.1 depicts the setup which was used for preliminary experiments. Main components are the quasi CW source which represents a modified version of the impulse generator from chapter 5. The schematic of the source with its narrowband excitation characteristics will be explained in the next section. The output of the quasi CW source is connected to an inductive element which delivers energy into objects placed in close vicinity. The inductance of the coil is chosen to match the capacitive output of the source, creating a low frequent resonance tuned to the detection bandwidth of the transducers. This LC resonance modulates the long pulses and creates a narrowband thermoacoustic excitation waveform. The sample is coupled closely to the inductance element to allow for optimum energy dissipation and the transducer is facing towards the sample, capturing narrowband acoustic waves originating from the targets. Acoustic signals are pre-amplified with a low noise 65 dB amplifier (AU-1291, Miteq, Hauppage, NY, USA) before digitizing. The inductances are isolated with high voltage shrinking tubes (Model HSR3000, 350 kV cm^{-1}, 3M, St. Paul, MN, USA) in order to prevent voltage breakthroughs into the surrounding deionized water which serves as the acoustic coupling medium. Finally, data is acquired with an oscilloscope (Model DPO7254, Tektronix Inc., Beaverton, OR, USA) while a PC controls data acquisition and the trigger generator with a custom made Matlab interface (Mathworks, Natick, MA, USA).

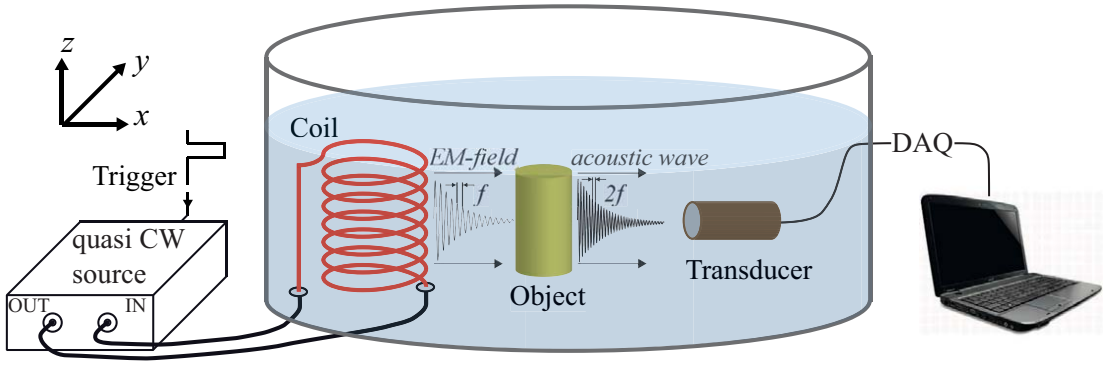

Figure 7.1: Experimental setup for quasi CW thermoacoustic wave excitation and detection; the object is placed in close vicinity to the coil in order to ensure efficient energy coupling; upon absorption of electromagnetic energy, the object induces a thermoacoustic wave at frequency $f_{TAS} = 2f_{quasi\,CW}$

7.2.3 Quasi CW generator

A schematic of the quasi CW source is depicted in figure 7.2. It can be separated into a low voltage part and a high voltage circuit. The low voltage unit consists of a triggering waveform input, connected to a function generator (33210A, Agilent Technologies, Santa Clara, CA, USA) and a dedicated circuit to convert the low voltage pulses from the trigger generator (+10 V) into high voltage equivalents. Therefore, the output of an adjustable DC power supply (Model: 1AA24-P20-M, Ultravolt, Inc., Ronkonkoma, NY, USA) is controlled via a thyristor. The generated 400 V pulses are further converted into high voltage 28 kV pulses with the transformer unit TR-1700 (External Trigger Transformer, Model: TR-1700, Perkin Elmer Optoelectronics, Fremont, CA, USA) which has a winding ratio of 70 : 1.

The high voltage circuit consists furthermore of the transformer output which is connected to a high voltage spark gap switch (Triggered Spark Gaps - Ceramic Metal, Model: GP-41B, Perkin Elmer Optoelectronics, Fremont, CA, USA), the high voltage power source (Model: 30C24-N125, Ultravolt, Inc., Ronkonkoma, NY, USA) and a RLC circuit. The HV source provides −30 kV DC which are used to charge the capacitor. Exhibiting a capacity value of $C = 1700$ pF, up to 1.5 J can be stored in the output circuit of the quasi CW source. The switch is triggered by the high voltage pulses from the transformer and short circuits the capacitor. The capacitor C in combination with the inductance L from the coil and the resistor R forms a dumped series resonance circuit with an exponentially decaying oscillation.

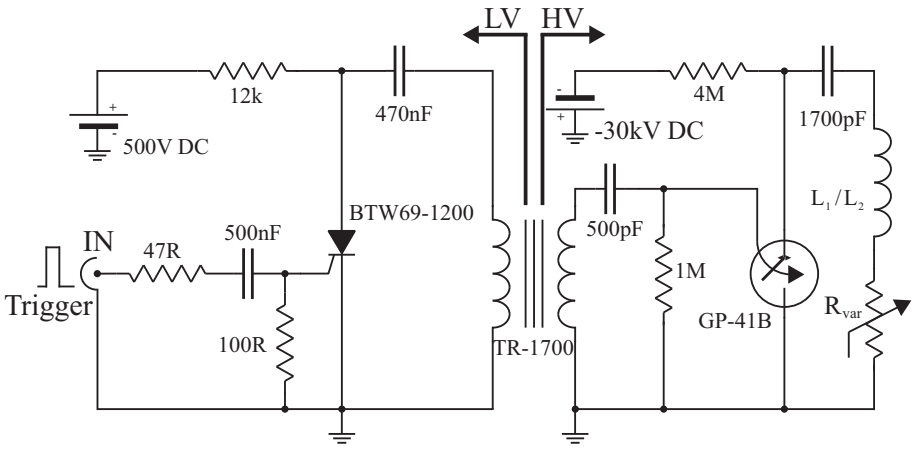

Figure 7.2: Schematic of the quasi CW source used for narrowband thermoacoustic excitation; LV - low voltage side containing the trigger signal and the adjustable 500 V DC power supply; HV - high voltage circuit comprised of the high voltage power supply (-30 kV) and the resonance circuit

7.2.4 RLC resonance circuit for quasi CW excitation

In our case, resonance describes the energy exchange between the inductance L and the capacitor C. The rate of energy transfer can be measured by the resonance frequency

$$\omega_{LC} = 2\pi f_{LC} = \frac{1}{\sqrt{LC}}. \tag{7.1}$$

In this work, two LC combinations were investigated, choosing the resonance frequency to match the detection bandwidth of the ultrasonic transducers. Table 7.1 lists important specifications of the custom made coils with the corresponding resonance frequencies in combination with the predefined capacitor $C = 1700$ pF.

	#turns	⌀ [mm]	length [mm]	L [µH]	resonance frequency f_{LC}
coil#1	3	50	40	3	2.1 [MHz]
coil#2	4	66	40	1.6	3.1 [MHz]

Table 7.1: Specifications of the custom built inductances along with their resonance frequencies in combination with $C = 1700$ pF

To monitor the stimulation signal induced by the designed inductances, a hand made free-field probe was fabricated. Depicted in figure 7.3, it consists of a RG 174 coaxial cable with the inner coaxial conductor connected to the outer ground layer of the cable with a 50 Ohm resistor. The field probe was placed closely to the energy dissipating coil, monitoring the electromagnetic field during thermoacoustic experiments.

Figure 7.3: Hand made probe used for electromagnetic field measurements

7.3 Results

This section presents the results obtained with the setup described above. Prior to the experimental results, numerical simulations using the wave equation solver from chapter 3 are discussed. This should outline the characteristic double frequency property of RF-thermoacoustics with narrowband excitation. Additionally, the RLC circuit is simulated using the PSpice simulation tool (Cadence Design Systems, Inc., San Jose, CA, USA). Subsequent to simulation results, experimental thermoacoustic signals are compared for two cases. First, broadband excitation of objects using an ultrashort pulse is discussed, while removing the damping element R from the resonance circuit finally demonstrates narrowband thermoacoustic signals following quasi CW stimulation. In a next step, liquids consisting of saline solutions and finally biological tissue exposed to narrowband excitation are presented.

7.3.1 Simulation results

The following section discusses the results obtained from simulations. In a first step, the simulation tool presented in chapter 3 provides a fundamental insight into the acoustic

wave induced by quasi CW excitation. Following up, a circuit simulator was used to compare the experimentally measured electric field with simulation results.

7.3.1.1 Thermoacoustic signal generation following quasi CW stimulation

Prior to the measurements which will be presented in section 7.3.2.1, two simulations with parameters similar to the experiments were performed. In a first simulation, a point like absorber ($\varnothing$ 230 µm) was placed at position 30 µs $\equiv$ 45 mm from the detector and excited with an exponentially decaying oscillation at $f_{quasi\,CW,1} = 2.1$ MHz. Figure 7.4a depicts the stimulation waveform pattern along with the thermoacoustic response from the absorber. According to the simulation, the thermoacoustic signal is oscillating at frequency $f_{TAS,1} = 2 \cdot f_{quasi\,CW,1} = 4.2$ MHz (see fourier transform in figure 7.4b).
The second simulation was carried out with similar parameters, changing the excitation frequency to $f_{quasi\,CW,2} = 3.1$ MHz. Observing the results shown in figure 7.4c, the thermoacoustic signal consistently appears at double frequency $f_{TAS,2} = 2 \cdot f_{quasi\,CW,2} = 6.2$ MHz. For the purpose of comparison, the fourier transform of the simulated thermoacoustic response and the excitation is additionally plotted in figure 7.4d.

7.3.1.2 RLC field measurement and circuit simulation

The following simulations and measurements demonstrate the transition from pulsed excitation with broadband nature to narrowband excitation with an exponentially decaying oscillation. Coils from table 7.1 in different RLC combinations were simulated and the results were compared with free-field measurements, using the hand made field probe to detect the electromagnetic field. All circuit simulations were performed using Cadence Orcad PSpice. Figure 7.5 depicts the equivalent circuit which was used for PSpice simulations, employing the parameters listed in table 7.2.

	configuration #	excitation type	R [Ω]	L [µH]	C [pF]	Q
coil#1	1	broadband	50	3	1700	0.7
coil#2	2	broadband	50	1.6	1700	0.7
coil#1	3	narrowband	0	3	1700	11
coil#2	4	narrowband	0	1.6	1700	13

Table 7.2: Parameters for 4 different simulations covering broadband excitation and narrowband quasi CW stimulation

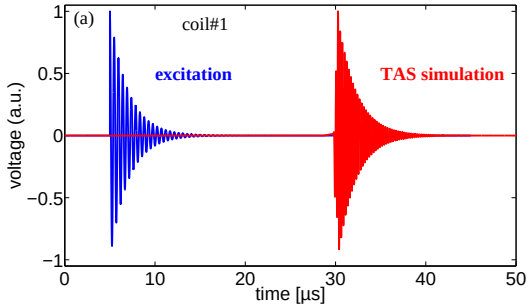

(a) Simulation of the thermoacoustic response following quasi CW narrowband excitation: simulation #1 - resonance frequency $f_{quasi\,CW,1} = 2.1$ MHz

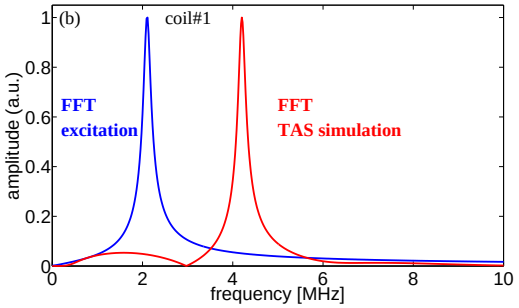

(b) FFT of thermoacoustic response and excitation profile for coil #1

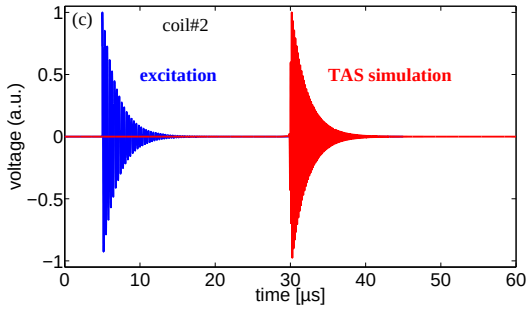

(c) Simulation of the thermoacoustic response following quasi CW narrowband excitation: simulation #2 - resonance frequency $f_{quasi\,CW,2} = 3.1$ MHz

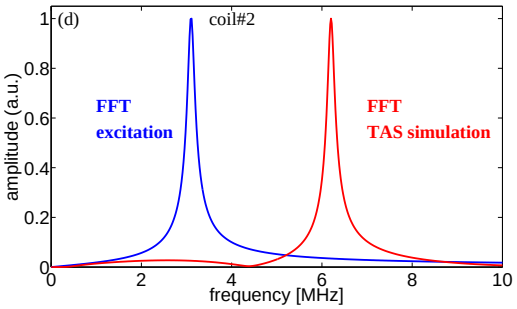

(d) FFT of thermoacoustic response and excitation profile for coil #2

Figure 7.4: Simulation results for excitation frequencies $f_{quasi\,CW,1} = 2.1$ MHz and $f_{quasi\,CW,2} = 3.1$ MHz along with the thermoacoustic response, comparing time domain and frequency domain (FFT)

Depending on the damping element R, excitation can be of broadband or narrowband nature. The Q-factor can be used to describe the quality of a resonance or, in other words, the quality factor estimates the damping factor of an oscillation. It can be calculated according to equation

$$Q = \frac{\omega_0 L}{R} = \frac{1}{\omega_0 RC} = \frac{Z_0}{R} = \frac{f_0}{\Delta f} \tag{7.2}$$

with the resonance frequency f_0 and the bandwidth Δf at 3 dB decay. The Q-factor for each configuration is additionally listed in table 7.2, exhibiting an almost critically damping behavior close to $Q = 1/2$ for both RLC topologies whereas the LC configurations represent underdamped systems with high quality factors.

Figure 7.6 compares the results obtained from PSpice simulations and free-field measurements for the damped RLC configuration. The bipolar shaped pulse from

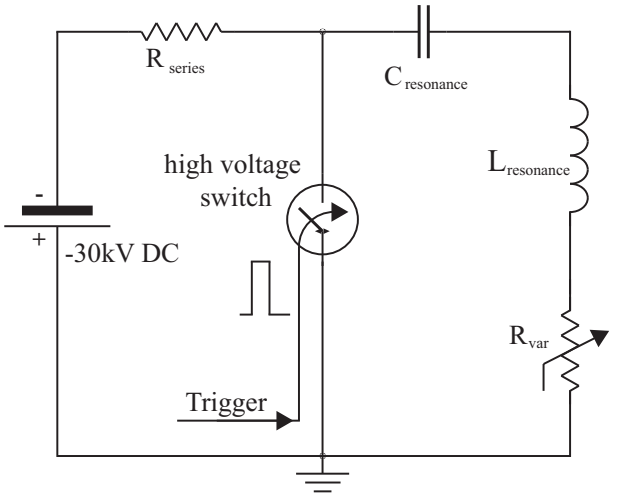

Figure 7.5: Schematic of the circuit used for PSpice simulations

simulation #1, equivalent to a critically damped system with a one cycled harmonic oscillation, ends after $t = 500$ ns, revealing the broadband excitation spectrum of $\Delta f = 3.5$ MHz (7.6a and 7.6b). Similarly, simulation #2 features one oscillation in a critically damped condition, stimulating frequencies from 1 MHz to 6 MHz at 3 dB (7.6c and 7.6d). Comparing the simulation results (red dotted lines) with the measurements (blue solid lines) reveals good congruence for both configurations.

The previous figures demonstrated a broadband excitation spectrum, similar to the time domain thermoacoustic system from chapter 5. Coming up, narrowband excitation profiles are discussed which ultimately will be used in the quasi CW system.
In order to create long harmonic oscillations, the damping element R is removed from the RLC resonance circuit. Figures 7.7a and 7.7b depict the results from the free-field measurement with coil #1, revealing a harmonic oscillation at $f_{quasi\,CW,1} = 2.1$ MHz which is extinguished after $t_{quasi\,CW,1} \approx 12$ µs. Changing the setup and replacing coil #1 with coil #2 results in a harmonic oscillation at $f_{quasi\,CW,2} = 3.1$ MHz due to the lower inductance of coil #2 (figure 7.7d). Moreover, the lower inductance confines the oscillation to a shorter time duration of $t_{quasi\,CW,2} \approx 8\ \mu$s (see figure 7.7c). This is attributed to the lower energy storage capability of coil #2. Comparing the PSpice simulation results (plotted in red) with the free field measurements (highlighted in blue) demonstrates good correspondence for both excitation frequencies.

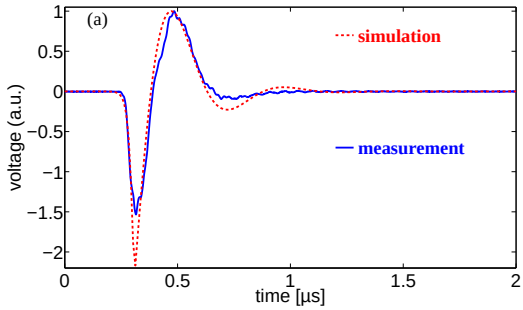

(a) Time domain comparison: configuration #1

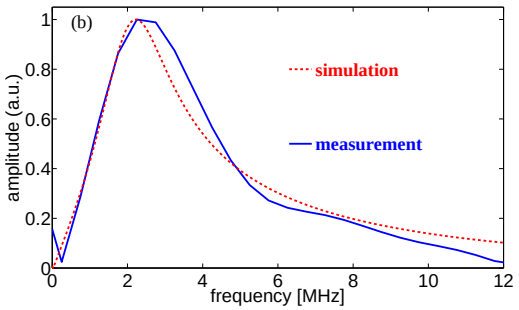

(b) Corresponding FFT of 7.6a

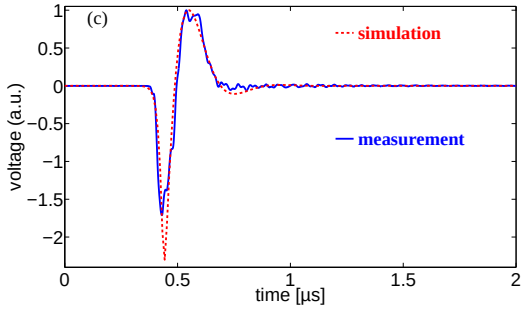

(c) Time domain comparison: configuration #2

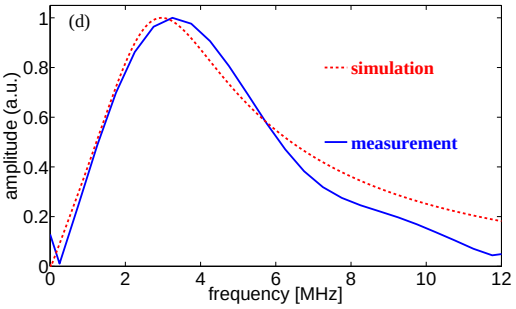

(d) Corresponding FFT of 7.6c

Figure 7.6: Comparison between free field measurement and PSpice simulation of RLC configurations #1 and #2

7.3.2 Phantom experiments

The quasi CW method was tested on three different types of phantoms: Starting with copper wires which generate strong thermoacoustic signals as we have seen in chapter 5, succeeded by liquids in the form of saline solutions and finally *ex-vivo* biological tissue from pork were examined with the quasi CW system. All phantoms were exposed to the quasi CW excitation pattern described in the preceding section while the thermoacoustic response was detected with a 3.5 MHz transducer. In order to distinguish between acoustic signals and excitation, objects were located at distances $d > \tau_{quasi\,CW} \cdot v_s$, with $\tau_{quasi\,CW}$ defined by the duration of the frequency modulated pulses. Since no imaging was performed, thermoacoustic signals were only detected from one projection. In addition to the quasi CW excitation pattern, the first phantom was furthermore exposed to pulsed stimulation to illustrate the transition from a broadband to a narrowband waveform profile.

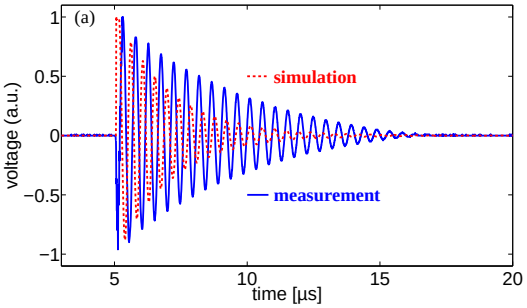

(a) Time domain comparison: configuration #3

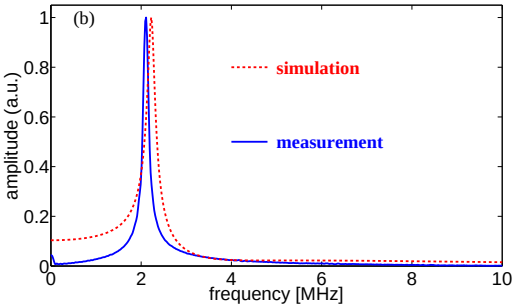

(b) Corresponding FFT of 7.7a

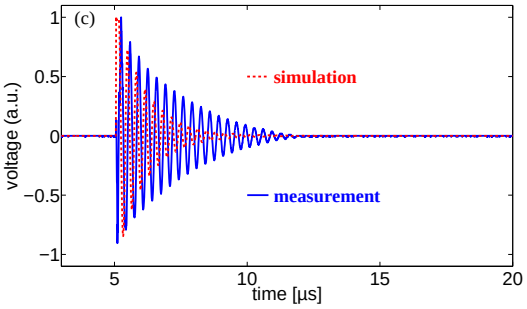

(c) Time domain comparison: configuration #4

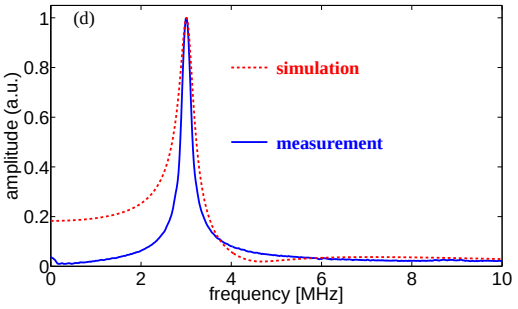

(d) Corresponding FFT of 7.7c

Figure 7.7: Free field measurement of the narrowband (quasi CW) stimulation pattern in comparison with PSpice simulation

7.3.2.1 Copper wire

Figure 7.8 depicts a photograph of the experimental layout with the location of the energy coupling element, the copper wire (diameter: ⌀ 230 µm) and the transducer. Other objects were placed in a similar position relative to the transducer and the energy coupler.

Exposing the copper wire to the pulsed waveform which is depicted in figure 7.6a yields the thermoacoustic response in figure 7.9. The thermoacoustic waveform in the time domain (7.9a) confirms the bipolar shaped (acoustic) pulse. The FFT of the thermoacoustic signal in figure 7.9b shows the broadband response which goes up to frequencies of 5 MHz, limited mainly by the detection bandwidth of the transducer but also by the excited frequency band which is plotted in the same figure for comparison.

So far, impulse excitation resulted in a broadband acoustic response. Recalling theoretical considerations from chapter 3 on the thermoacoustic response due to narrowband stimulation concluded the following:

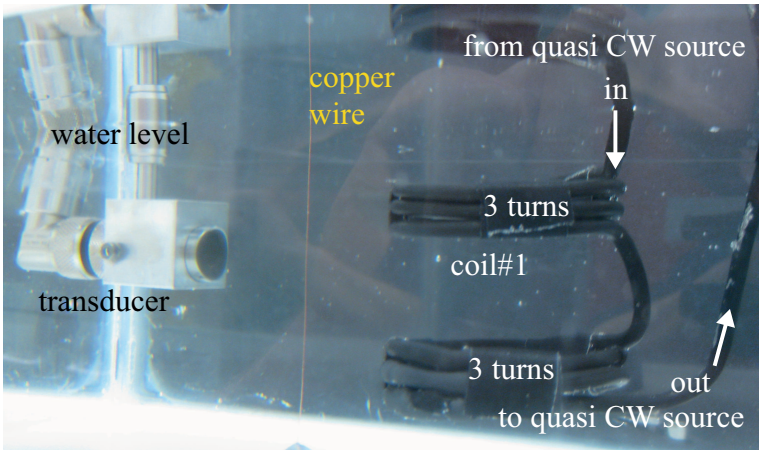

Figure 7.8: Photograph of the quasi CW experimental setup: The transducer is facing the object which is coupled to the energy coupling element (here: coil#1)

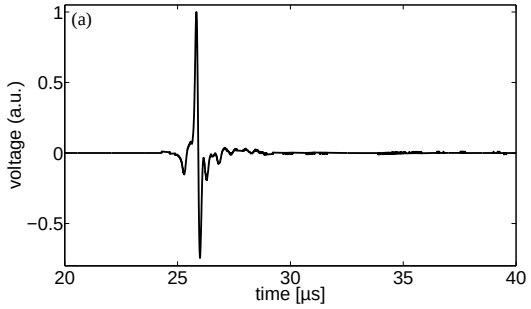

(a) Measured thermoacoustic response following the broadband excitation pattern 7.6a

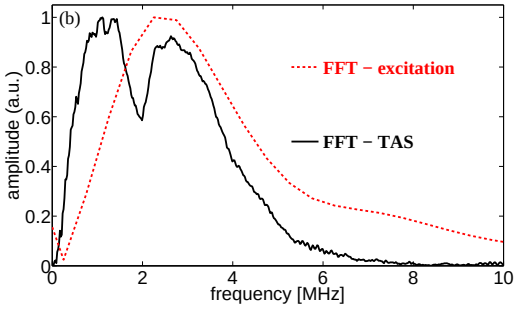

(b) FFT of the thermoacoustic response (black solid line) along with the corresponding FFT of the excitation pulse (red dotted line)

Figure 7.9: Thermoacoustic response from a copper wire in response to broadband excitation in time domain and frequency domain

The optoacoustic response is a replica of the optical input, e.g. assuming an intensity modulated laser beam at frequency f_{opt}, the optoacoustic response will take place at the same modulation frequency $f_{OAT} = f_{opt}$.
For the case of electric field stimulation, assuming a time varying electric field at frequency f_{RF}, the thermoacoustic response will occur at the frequency $f_{TAS} = 2 \cdot f_{RF}$.

Based on this hypothesis, the narrowband excitation in the form of a quasi CW profile as plotted in figure 7.7a would cause a narrowband acoustic response at the frequency $f_{TAS} = 2 \cdot f_{quasi\,CW}$.
Figure 7.10a depicts the stimulation pattern from coil #1 along with the thermoacoustic response from the copper wire. As expected, the acoustic signal is induced at the position of the copper wire, located at a distance of 45 mm from the acoustic detector. The

duration of the thermoacoustic signal is similar to the excitation waveform, exhibiting an exponential decay of the oscillation. Referring to the fourier transform plotted in figure 7.10b, the thermoacoustic response is appearing at the expected frequency $f_{TAS,coil1} = 2 \cdot f_{quasi\,CW,coil1} = 4.2$ MHz.
Confirming the hypothesis with the second coil #2 which had a LC resonance frequency $f_{quasi\,CW,coil2} = 3.1$ MHz, the thermoacoustic response is taking place at $f_{TAS,coil2} = 2 \cdot f_{quasi\,CW,coil2} = 6.2$ MHz as demonstrated in figure 7.10c and 7.10d.

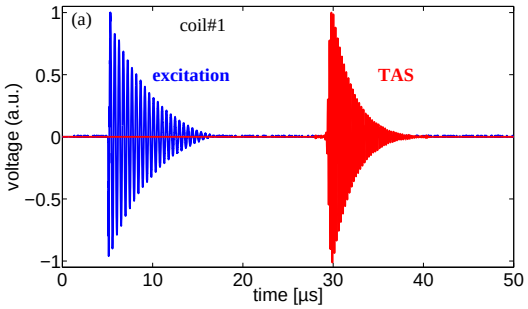

(a) Excitation profile (blue line) along with the measured thermoacoustic response (red line) from coil #1 with a resonance frequency $f_{quasi\,CW,1} = 2.1$ MHz

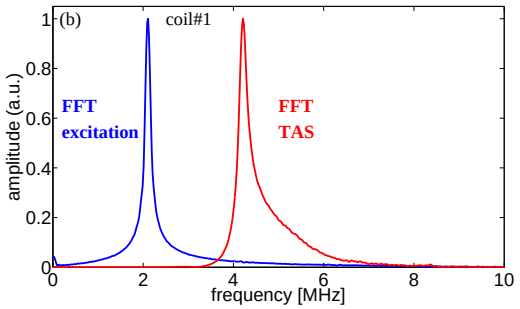

(b) FFT - Excitation profile (blue line) with the measured thermoacoustic response (red line)

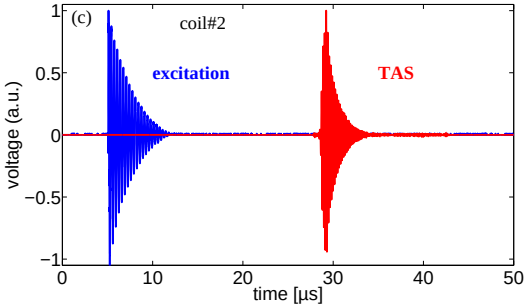

(c) Excitation profile (blue line) along with the measured thermoacoustic response (red line) from coil #2 with a resonance frequency $f_{quasi\,CW,2} = 3.1$ MHz

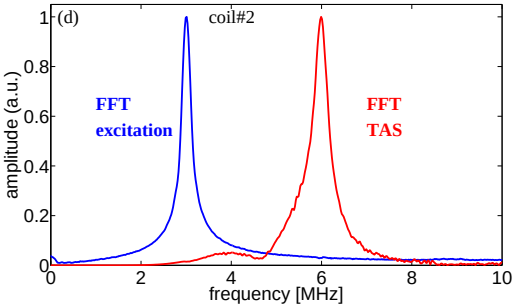

(d) FFT - Excitation profile (blue line) with the measured thermoacoustic response (red line)

Figure 7.10: Experimental results from copper wires: Excitation pattern along with thermoacoustic response at two different frequencies

7.3.2.2 Tissue mimicking phantom

The preceding measurements were performed on high absorbing non biological tissue. In a next step, we investigated the thermoacoustic signals in tissue mimicking phantoms. Therefore, saline solutions at different concentrations were prepared and filled in low RF

absorbing PVC tubes which had a diameter of ⌀ 5 mm. The concentrations ranged from 0.009% to 18% with an additional baseline measurement, consisting of a PVC tube filled with low absorbing mineral oil. Thermoacoustic signals were detected with the 3.5 MHz transducer using configuration #1 with coil#1.

Figure 7.11a plots the thermoacoustic response from a PVC tube filled with 0.9% physiological saline solution. The thermoacoustic signal is initiated at 25.5 µs, corresponding to the location of the tube at a distance of $\sim$ 40 mm from the detector. After $\sim$ 3.5 µs a second signal peak with decaying oscillation occurs, correlating to the diameter of the tube. Clearly, the second peak is almost one order of magnitude higher than the first signal. Taking into account the positioning of the tube in the quasi CW system, the higher peak correlates to the tubing wall which was located closer to the energy coupling coil. Hence, energy deposition was stronger in the tube facing the coil.

Note that a third peak is appearing at time position 36 µs which can be attributed to acoustic reflections from the PVC walls. For a better understanding, chart 7.12 outlines the propagation of acoustic waves outside and within the tube and the origin of signals with respect to the projection angle of the transducer. At the boundary T_1, acoustic waves on both sides of the tube's boundaries are induced, with the first acoustic wave being detected at $t = 25.5$ µs. The second wave is propagating within the tube and reflected at the other end of the tube (tagged as $[A]$), highlighted as T_2.

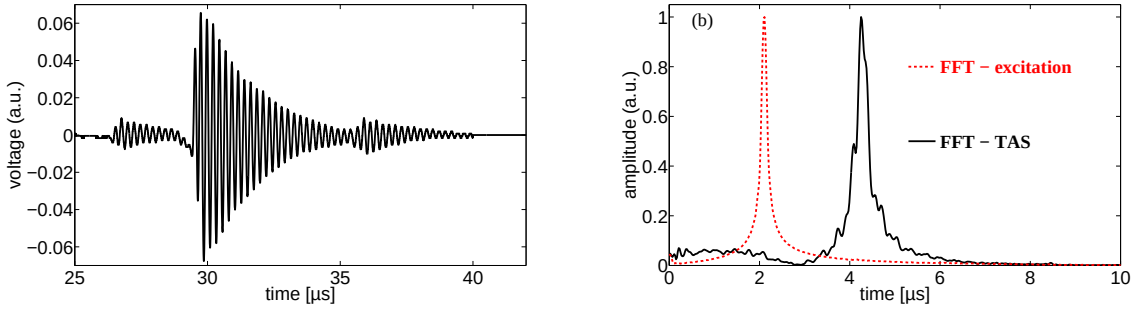

(a) Time domain: Thermoacoustic signals and reflections in the PVC tube

(b) Corresponding FFT of 7.11a along with the excited frequency band

Figure 7.11: Quasi CW thermoacoustic response induced in a saline filled PVC tube

A similar process can be observed for the second wall marked as T_2 where two propagating waves are generated. The acoustic wave at T_2 which is traveling towards the transducer is detected at time point $t = 29$ µs and reflected at the boundary T_1 (marked as $[B]$). Traveling back in the tube, it is again reflected at marker point $[C]$ and finally detected by the transducer at time point $t = 36$ µs. It has to be remarked that the

drawing only outlines the basic reflections which contribute to a detectable signal. Since thermoacoustic waves are propagating isotropically, a holistic explanation towards the reflection mechanisms inside the tube is more complex and not within the scope of the thesis.

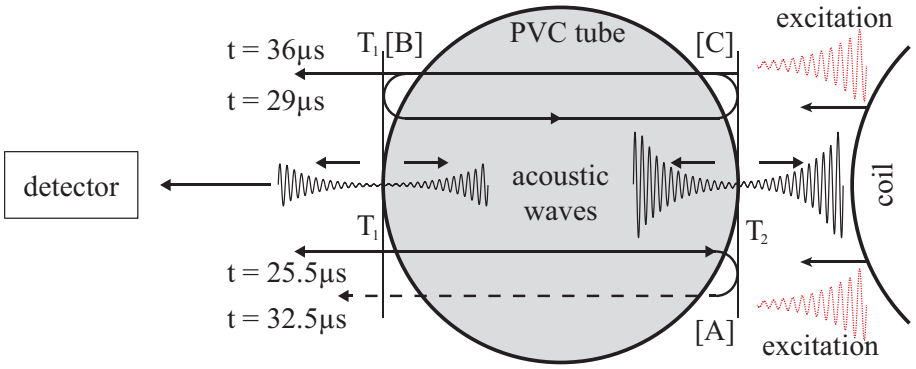

Figure 7.12: Top view of a schematic measurement demonstrating the reflections of acoustic waves occurring in the tube: red lines: excitation; black lines: acoustic response; T_1 tubing wall 1; T_2 tubing wall 2; [A] acoustic reflection at tubing wall T_2; [B] acoustic reflection at tubing wall T_1; [C] second acoustic reflection at tubing wall T_2

Finally, figure 7.13 plots the peak values of measured signals depending on the saline concentration. The value zero corresponds to the baseline measurement, i.e. the mineral oil filled PVC tube. In total, two consecutive measurements were performed with the curve denoting the mean value. Although the deviation is in the order of $\sim 60\%$ between both experiments, a linear increase can be observed starting from low concentrated water saline at 0.009% to higher concentrations at 9%. From that level, a saturation of the signal can be monitored.

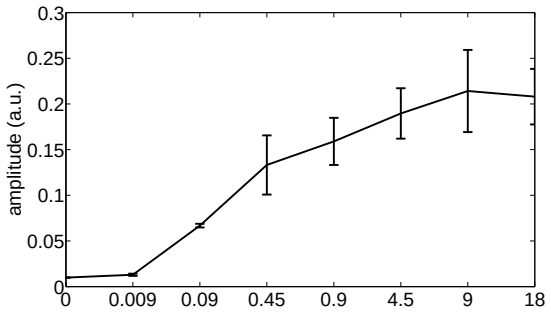

Figure 7.13: Sensitivity measurement showing the linear increase of thermoacoustic signals from saline filled PVC tubes with rising concentrations

7.3.2.3 *Ex-vivo* biological tissue

In a last experiment, the quasi CW response from biological tissue was examined. Therefore, a piece of pork muscle was prepared for quasi CW thermoacoustic measurements, cutting a slice with a thickness of approximately 5 mm into a circular shaped object. The phantom was then placed in the imaging tank closely to the energy dissipating coil #1 (see table 7.1). Similar to previous measurements, a 3.5 MHz transducer was used to detect the narrowband thermoacoustic signals.
Figure 7.14a depicts the results from the measurement. The narrowband signal is confined to the area of the meat, starting at $t \approx 43$ µs and vanishing at time point $t \approx 46$ µs. The Fourier transform of the signal, depicted in figure 7.14b, plots the excitation signal oscillating at $f_{quasi\,CW,1} = 2.1$ MHz and the thermoacoustic narrowband response occurring at $f_{TAS,1} = 4.2$ MHz.

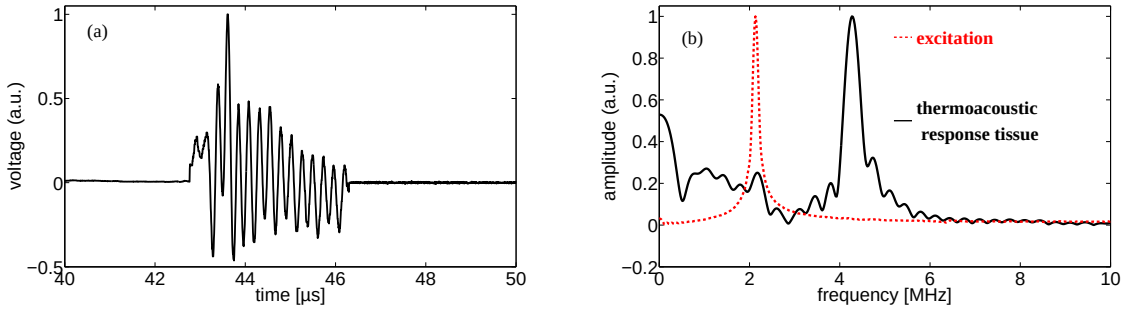

(a) Thermoacoustic response from pork muscle

(b) FFT of the thermoacoustic response (solid black line) along with the excitation profile (dotted red line)

Figure 7.14: Biological tissue measurement revealing the double frequency dependence of biological tissue in time and frequency domain

7.4 Discussion

This chapter described a prototype system which facilitated the induction of narrowband thermoacoustic signals. A dedicated source was built which matched the requirements for long RF pulses with monofrequent harmonic oscillation. The so called quasi CW excitation lasted for ~ 10 µs and exhibited an exponential decay over time, combining high energy with narrowband stimulation.
Theoretical considerations assumed a monofrequent acoustic wave in response to CW excitation. In contrast to optical CW excitation where the acoustic response is a replica

of the modulated light, RF stimulation induces acoustic waves at double frequency $f_{TAS} = 2f_{CW}$. The double frequency dependency is related to the modulated E-field for the RF case whereas in frequency domain optoacoustics the laser intensity is modulated.

The quasi CW method was performed on different phantoms. The first object consisted of a highly absorbing copper wire which was placed closely to the energy emitting coils. According to our knowledge, the induced narrowband signal is the first documented thermoacoustic response following CW stimulation in the radiofrequency band. Upon confirming hypothesis on double frequency dependency, tissue mimicking phantoms and *ex-vivo* biological tissue were furthermore tested with the quasi CW method exhibiting a similar behavior.

Although the developed method represents a powerful tool in particular for the induction of monofrequent acoustic waves, major drawbacks limit the further application towards imaging. In its current state, the quasi CW source is only capable of generating monofrequent signals, however, an imaging approach would necessitate a frequency modulation of the output. Furthermore, similar to the NRT impulse generator, the quasi CW method is primarily generating contrast from conductive/dielectric matter. Thus, without appropriate conductive particles, the quasi CW system can only be used for anatomical imaging while molecular imaging stays in the focus of this research.

8 Frequency domain thermoacoustic tomography

8.1 Introduction

Continuing the transition from time domain to frequency domain thermoacoustics, this chapter presents the prototype version of a frequency domain thermoacoustic tomography system (FD-TAT). Since the generation of thermoacoustic signals with CW sources is associated with several problems (see chapter 7), a special design was considered which makes generation and detection of thermoacoustic waves feasible. The FD-TAT concept along with the experimental setup which is based on a class DE-amplifier is introduced in section 8.2. Section 8.3 reviews the results from highly dissipative objects before the discussion 8.4 summarizes the findings.

8.2 Implementation

8.2.1 Design considerations for a CW thermoacoustic setup

8.2.1.1 A brief retrospect

Before proceeding to the demands on the frequency domain imaging system, a short excursion to the time domain technology is discussed herein. This is important to understand the requirements to the CW based technology.
Basically, all thermoacoustic imaging systems are time domain approaches operating with pulsed excitation sources [66], [29], [70], [10]. Summarizing again the benefits of TD-TAT, a pulsed approach offers
(1) time gating enabling the temporal separation of electromagnetic interferences and thermoacoustic signals

(2) high energies per pulse, resulting in strong thermoacoustic signals (SNR)
(3) time of flight measurements for spatial resolution of acoustic absorbers
(4) broadband excitation yielding broadband acoustic responses
(5) spectral components of thermoacoustic signals inherently carrying information about the object's size

At the same time, the major drawbacks can be summarized as
(1) expensive and bulky technology
(2) limited applications in the field of biomedical imaging (no molecular/functional imaging/less useful intrinsic contrast)

Referring in particular to the last issue, time domain thermoacoustics as a biomedical imaging tool is struggling with low intrinsic contrast from biological tissue and limitations in molecular and functional imaging.
In this sense thermoacoustics has a limited application spectrum since it offers only anatomical imaging with conductive/dielectric tissue contrast (except for one documented molecular imaging study which was presented in a publication by Nie et al. [82]).

8.2.1.2 Frequency domain thermoacoustics with a 407 MHz microwave source

The first documented study on a CW based thermoacoustic imaging system dates back to the year 2009 when Ye presented "a preliminary study of the Thermoacoustic Tomography (TAT) using continuous-wave (CW) modulated microwaves" [131]. In his work, the output of a 407 MHz microwave generator is down converted to an intermediate frequency by means of a mixer to match the detection bandwidth of the transducer. The modulated CW excitation signal is furthermore amplified by a RF amplifier which has an output power of 50 W. Energy is coupled into the sample with a microstrip antenna which is placed below the sample. Acoustic signals from the transducer are detected with the lock in method after preamplification with a 40 dB amplifier. Although significant effort is put in the shielding and suppression of electromagnetic interferences, the system is not capable of detecting a CW thermoacoustic signal. This is mainly attributed to the low signal to noise ratio of the thermoacoustic signal and the strong electromagnetic interferences which are occurring at the same frequency.

8.2.1.3 Frequency domain thermoacoustic imaging - a design study

The findings from the preceding chapters influenced the design study for the frequency domain thermoacoustic imaging system. Similar to the NRT method, the thermoacoustic CW imaging system should be composed of
(1) cost efficient hardware components in a handy casing instead of a bulky implementation. Furthermore, the FD-TAT system should be capable of
(2) performing molecular and functional imaging with thermoacoustic methods. With respect to the expected low signal to noise ratio,
(3) the power should be adjustable from minor to high power levels also to be able to distinguish the thermoacoustic signals from the electromagnetic interferences. Finally, the energy coupling element should be designed in such way that it can
(4) focus the electromagnetic energy on defined areas.

The first point will be elaborated in the experimental setup section 8.2.2.

The second point aims at imaging of extrinsically administered agents or probes. As already described in chapter 2, the thermoacoustic imaging system should be able to resolve sources of magnetic contrast. Magnetic nanoparticles, for instance, represent appropriate thermoacoustic contrast agents for their known ability to convert electromagnetic energy efficiently into thermal energy [107], [74], [51], [23]. Moreover, magnetic nanoparticles with conjugated antibodies are also applied in targeted hyperthermia [18].

According to hyperthermia therapy, magnetic nanoparticles like $CoFe_2O_4$ efficiently convert electromagnetic energy into thermal energy at field strength > 2 kA m^{-1} [117] while magnetites (e.g. Fe_3O_4) are examined for magnetic field strength at > 5 kA m^{-1} in [56]. Thus, the power of the electromagnetic source has to be settled at similar levels.

The last issue corresponds to focusing of electromagnetic radiation in order to couple energy more efficiently into the sample. Therefore, the next section presents the experimental setup with a Helmholtz coil which confines electromagnetic energy onto the area of the coil.

8.2.2 Experimental setup for CW thermoacoustic signal generation

This section discusses the experimental setup focusing in particular on the CW source. A class DE amplifier was built for its known capability to be operated at high power levels

with frequencies in the MHz region [62]. A class DE amplifier is basically a ”Class D type high frequency tuned power amplifier with Class E switching conditions” [61]. In other words, class DE unifies the efficiency of class D amplifiers with the high frequency operation capability of class E amplifiers.
Note that the holistic explanation to the amplifier's operation conditions is not within the scope of the thesis, therefore only the basics such as the technology and the fundamental switching conditions are explained in the following section.

The basic components of the experimental frequency domain thermoacoustic imaging setup are shown in figure 8.1. Each of the elements will be explained thoroughly in this section. The system is comprised of a DC power source (PS) which provides a maximum power of 500 W with a maximum voltage of 100 V. The high power amplifier is connected to the power supply and driven by the signal generator (Model 33210A Function/Arbitrary Waveform Generator, Agilent Technologies, Santa Clara, CA, USA) which produces a pulse train to drive the MOSFETs. The schematic of the amplifier will be explained in the next section. An impedance matching transformer (highlighted as T in the figure) steps down the voltage at the output part of the transformer (marked as a red line), at the same time raising the current on the secondary of the transformer.
The secondary part consists of the resonance circuit, a water cooling system, the acoustic detection part and a personal computer. The resonance circuit includes a capacitor (C) and an inductance (L). The coil is designed as a Helmholtz coil in such way that it can accommodate the transducer (central frequency 3.5 MHz, focal distance 38.1 mm, bandwidth 76.3%; Model V382, Olympus-NDT, Waltham, MA, USA) which is located in the center of the coil. The sample holder, clad by the coil, has a diameter of $\sim$ 50 mm and is filled with deionized water which acted as the coupling medium for induced acoustic waves. The wire of the secondary part is made of a copper pipe (RS, outer-$\varnothing$ 4 mm, inner-$\varnothing$ 2.8 mm, RS Components GmbH, Germany) which is connected to a water cooling system. The water chiller circulates deionized water in the secondary circuit with a pump. The water cooling system will be explained more precisely in section 8.2.2.3.

8.2.2.1 Class DE amplification unit

The following discusses the high power amplifier which is depicted in figure 8.1.
Theoretically, class DE amplifiers can be realized in a full bridge topology, a push pull inverter or a half bridge topology [45], [25]. With respect to the easiness of implementation, the half bridge topology is favored over the full bridge topology since it requires only two switches. The push pull inverter is not considered because of the coupling transformer

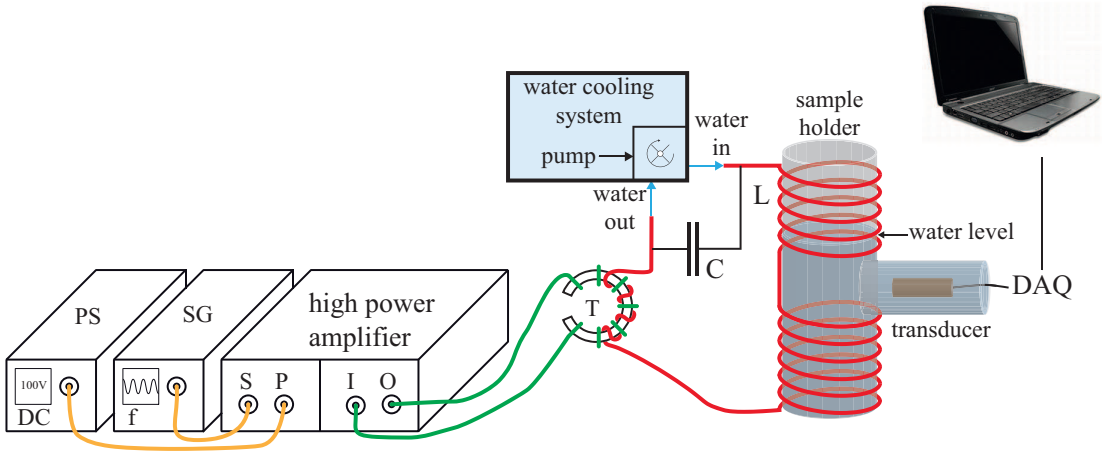

Figure 8.1: Schematic representation of the CW thermoacoustic tomography system; PS - Power Source; SG - Signal Generator; C and L - capacitor and coil creating a resonance circuit; T - Transformer; DAQ - Data Acquisition

which introduces additional limitations and losses.

The corresponding schematic is depicted in figure 8.2. An adjustable DC power supply (500 W, $U_{DC} = 0 - 100$ V) is connected to back-up capacitors (C_1 and C_2) followed by the switching circuit. The switches consist of two N-channel MOSFETs (Model IRFP460, STMicroelectronics N.V., Amsterdam, NL) which are connected in series. Two flyback diodes (D_1 and D_2) together with snubber capacitors (C_3 and C_4) are connected in parallel to the MOSFETs to allow for freewheeling of the induced voltage after switching. The output (OUT) is linked to the mid-point of the half bridge and the mid-point of the capacitors C_5/C_6 which divide the input voltage in half.

Additionally, a picture of the half bridge inverter is shown in figure 8.3. With respect to the intended high frequency high power application, the high side (HS) and ground of the half bridge had to be arranged in a stacked topology. This geometrical design minimized the connection length between high side, low side (LS) and ground, thus keeping parasitic effects at a minimum. For the sake of completeness, the inset in figure 8.3 shows a chart of the front view illustrating the connections between the MOSFETs. The stacked topology is comprised of two layers of copper sheets (thickness: $d = 2$ mm), representing the high side and ground, with a centered insulation layer made of teflon. The low side which is equivalent in size and material to the high side and ground is placed next to the stack for low inductance purposes.

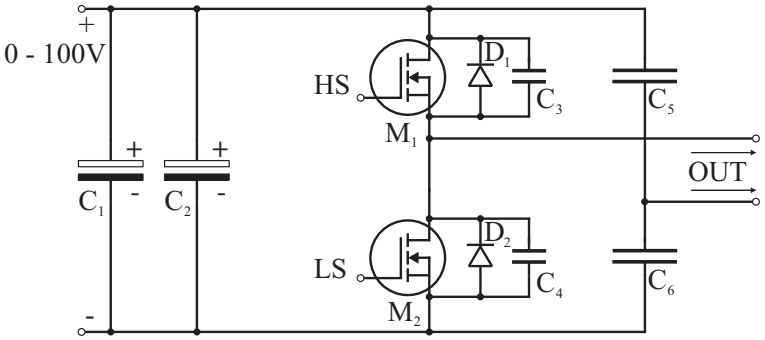

Figure 8.2: Schematic of the high power amplifier realized in a half bridge topology; HS - high side; LS - low side; M_1 - MOSFET1; M_2 - MOSFET2

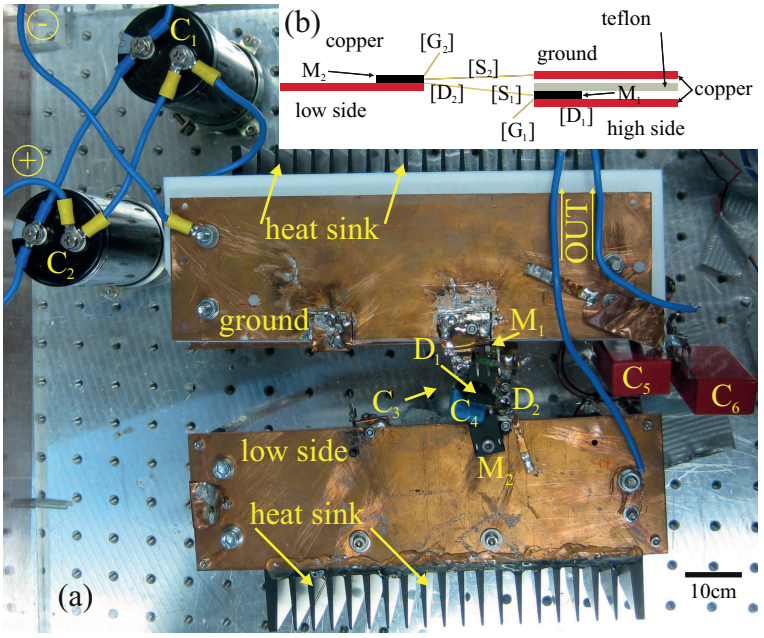

Figure 8.3: (a) Photograph of the experimental high power amplifier showing a top view of the half bridge circuit along with passive components; (b) schematic front view demonstrating the layout of the MOSFETs M_1 and M_2 with the corresponding connections [G] - Gate, [S] - Source and [D] - Drain

8.2.2.2 Functionality and operation characteristics

This section explains the basic operation principles of the amplifier with a particular focus on the driving of the switching elements.

Basically, the amplifier converts a low power input signal into an equivalent signal at higher power. Therefore, an input signal which is comprised of a pulse train at frequency f_{in} with a duty cycle of $40-50\%$ is driving the switching elements. The switches, i.e. the MOSFETs, are successively turned on and off according to the input signal, creating output pulses at equal frequency f_{in}. The output signal contains undesired spectral components which have to be filtered with a low pass filter. After filtering, the output

signal represents an amplified sine-like signal at the frequency f_{in}.

Switching conditions play an important role in the safe and efficient operation of the high power amplifier. Figure 8.4 documents schematically the switching signals which are applied to the two MOSFETs. It can be seen that both MOSFETs are driven at the same frequency and duty cycle except for a π shifted phase between the high and low side signal. The introduced dead time between the *ON* state of first MOSFET and the *OFF* state of the second MOSFET prevents the undesired shoot through condition which causes a short circuit of the power supply. In other words, if both switches are simultaneously *ON*, cross conduction takes place, inducing intense high current pulses in the switching elements. Running the MOSFETs without considerable dead time results in fast degrading and finally in destruction of the switches.

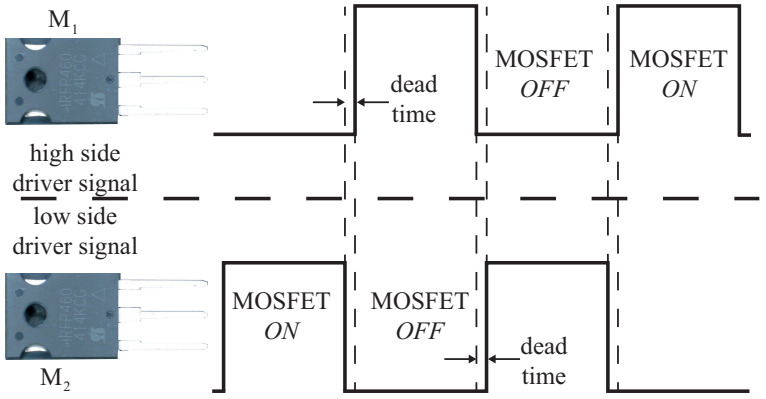

Figure 8.4: Pulse trains applied to the MOSFETs M_1 and M_2 on the high side and low side of the half bridge; the dead time defines a non conducting state both on the high and low side

De Vries suggested a MOSFET driver circuit with an adjustable analog time delay based on simple CMOS logic devices and passive components in his thesis [25]. Based on his findings, a modified driver circuit was built which generates high and low side MOSFET driving signals. The circuit is depicted in figure 8.5 while the corresponding PCB is shown in figure 8.7. Advanced CMOS logic devices with TTL compatibility (ACT) with respect to their fast fall and rise time are employed.
The block diagram in figure 8.6 explains the basic operation steps of the logic devices along with the dead time regulator which is implemented as a RC module in the form of an adjustable potentiometer. The dead time can be changed with the RC time constant, regulating the subtraction of the time delay from the initial signal with a dedicated *AND* logic.
Upon transferring the high side and low side functions to the gates of the MOSFETs, two

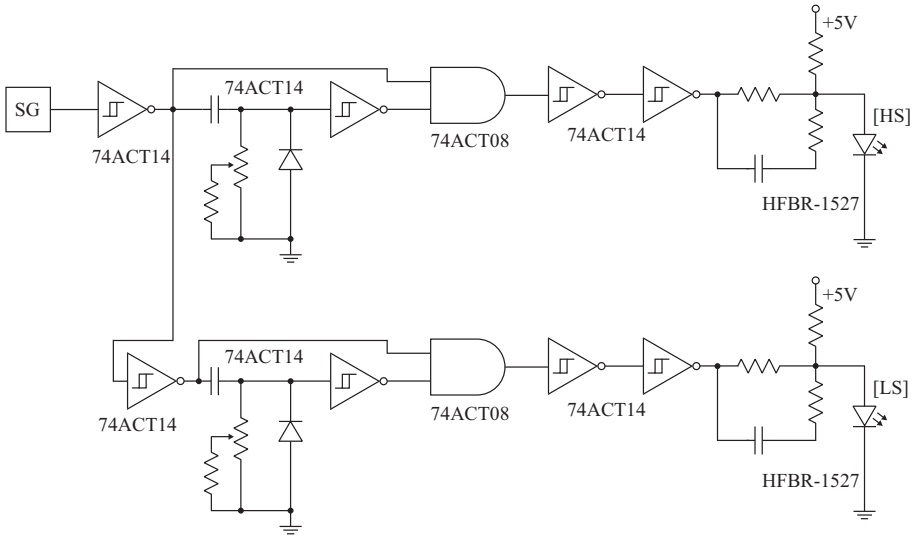

Figure 8.5: Analog circuit creating the drive signals for control of the MOSFETs; SG - signal generator; HS - optical fiber connection to high side; LS - optical fiber connection to low side

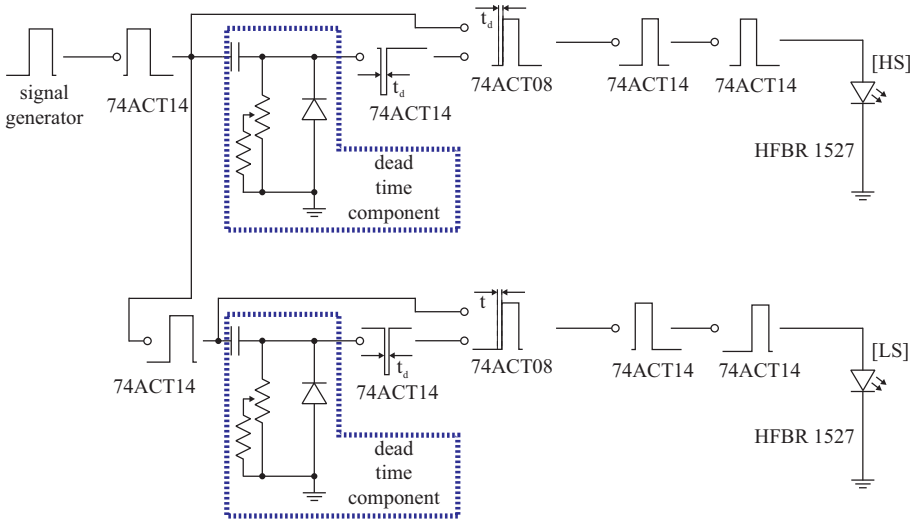

Figure 8.6: Schematic explanation of the components depicted in figure 8.5; the pulse from the signal generator is split into two components introducing a π phase shift; the dead time component allows for individual dead time regulation on each signal

intermediate steps have to be discussed:

Relating to circuit 8.5, the drive signals are referenced to the same ground. However, the half bridge topology requires the high side of the amplifier to be separated from the low side ground. Thus, the high side signal has to be connected to the HS-MOSFET while the high side ground is referenced to the midpoint of the half bridge (see figure 8.2). The low side on the other hand has to be connected to the LS-MOSFET and the common

ground of the amplifier.
Ground separation is facilitated with an optical transmitter (HFBR 1527, Avago Technologies, San José, CA, USA) which allows for broadband transmission of electric signals. Thus, the low side and the high side are decoupled from the common ground and the high side signal can be referenced to the midpoint potential of the half bridge.

Referring to the second step, the gate signals require a special gate driver which is able to provide sufficient drive current to turn the MOSFETs on. Therefore, two identical electric circuits, one for the high side and the other for the low side signal were built based on the template in [25]. Both circuits consist of an optical receiver (HFBR 2526, Avago Technologies, San José, CA, USA) which converts optical into electric signals and an ultrafast comparator (LT1016) which restores the signal to its original shape before optical transmission. Finally, the gates of the MOSFETs are connected to high speed power MOSFET drivers (EL7104, Intersil, Milpitas, CA, USA). The corresponding schematic is depicted in figure 8.8 along with a photograph of the electric circuit realized on a PCB (see figure 8.9).

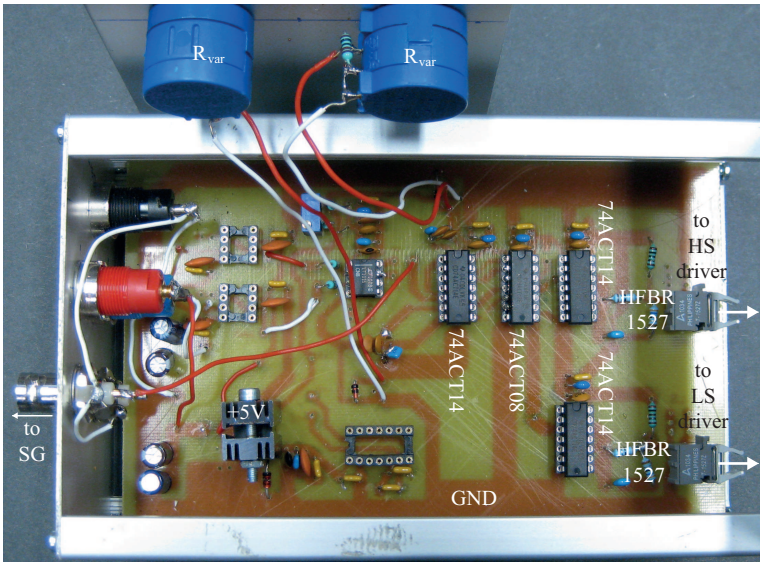

Figure 8.7: Photograph of the circuit on a PCB which generates the high side and low side drive signals; SG - input from signal generator; HFBR1527 - optical output to drive circuit shown in figure 8.9

8.2.2.3 Resonance circuit and cooling system

This section discusses the secondary part of the transformer in figure 8.1, describing the resonance circuit and the cooling system.

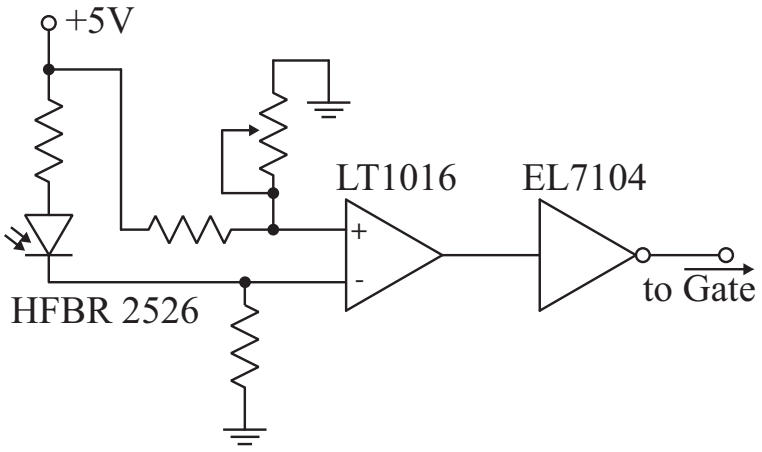

Figure 8.8: Schematic of the drive signal circuit showing the optical receiver HFBR 2526, the comparator LT1016 and the gate driver LT7104 which is connected to the Gate of the MOSFET

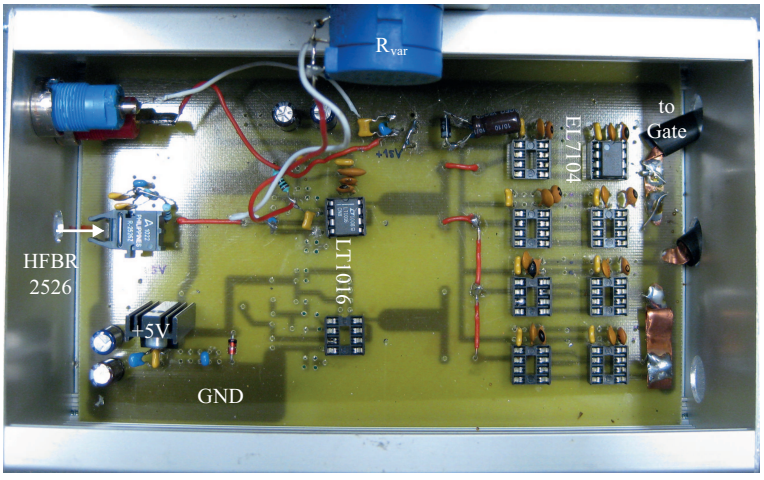

Figure 8.9: Photograph of the drive signal PCB showing the optical receiver HFBR 2526, the comparator LT1016, the gate driver LT7104 and the output connected to the Gate of the MOSFET

An inductance L and a capacitance C constitute the resonance circuit similar to the quasi CW method in chapter 7. The coil had to be designed in such a way that it can accommodate the sample within the coil and the transducer which has to face a certain region of the sample. A Helmholtz coil which is comprised of two identical magnetic coils arranged symmetrically along a common axis meet the requirements since it allows for the phantom accomodation but more importantly provides a detection window between the two pairs of the Helmholtz coil. The length of the coil is $l = 95$ mm with a diameter of $\varnothing\,60$ mm, resulting in 5 turns per Helmholtz coil element or 10 turns in total. The geometry determines the inductance of the coil to $L = 2.6$ µH.

In order to achieve a resonance at the aimed frequency of $f_{CW} \approx 800$ kHz, 6 capacitors

were connected in parallel, resulting in a total value of $C = 14.4$ nF.

Heat dissipation in the resonant circuit requires a distinct cooling method of the

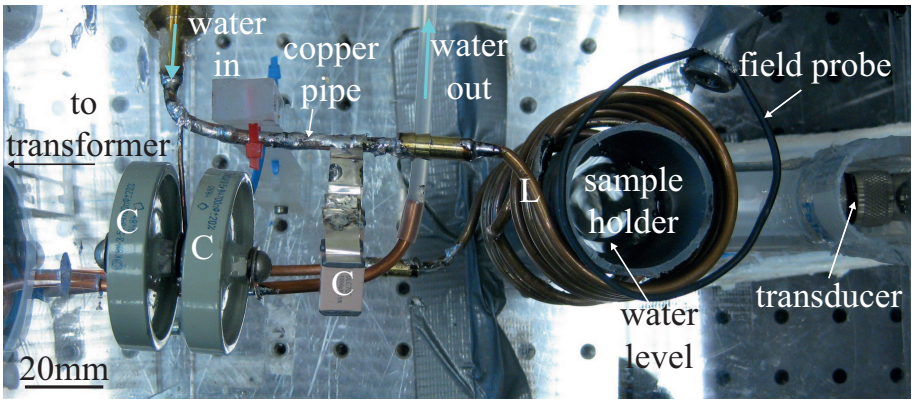

Figure 8.10: Photograph of the resonance circuit showcasing the transformer output, the water cooling system, the resonance elements L/C and the sample holder together with the transducer

wires and elements (i.e. mainly the Helmholtz coil). Therefore, a dedicated cooling system was designed for the secondary winding of the transformer (see figure 8.10). It includes the lead wires and the Helmholtz coil which are both realized as copper tubes with an outer diameter of 4 mm and an inner diameter of 2.8 mm. The end of the tubes is connected via PVC hoses to a water cooling system consisting of a pump and a water chiller (Model HC-500A, Guangdong Hailea Group Co., Ltd, China). The circulation system is filled with deionized water which does not contribute to the current flow. This can be attributed to the skin effect which concentrates the alternating electric current on the surface of a conductor. The skin depth for copper with a conductivity $\sigma = 5.813 \times 10^7$ S m^{-1} [93] and an AC electric current at $f_{CW} = 800$ kHz is calculated to $\delta_{skin} \approx 74$ µm. In other words, the current density is concentrated at the outer surface of the copper pipe, allowing for water circulation in the copper tubings since the interior does not contribute to the current flow. Figure 8.13 illustrates the skin effect occurring in the copper tube.

During operation, the cooling system circulates deionized water through the PVC tubes and copper pipes to ensure a constant temperature of both the Helmholtz coil and the lead wires. It has to be remarked that the cooling system is essential for constant power levels and stable resonance frequency during CW operation.

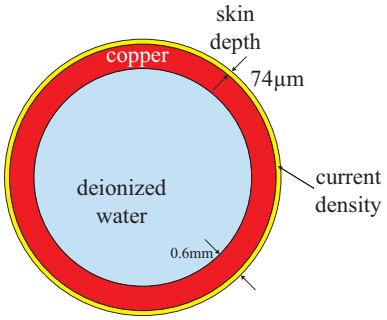

Figure 8.11: Schematic representation of the current which is concentrated on the outer surface due to the skin effect

8.3 Results

This section presents preliminary results obtained with the FD-TAT system. It is important to note that the conducted experiments were confined to non biological tissue while the major interest of this research, i.e. the experimental verification of thermoacoustic signals coming from magnetic nanoparticles, has not been achieved yet. The main problem is still related to electromagnetic interferences originating from the high power amplification unit which generates higher harmonics. In particular the second harmonic which is occurring at the frequency where the thermoacoustic signal is expected complicates the detection of the already low thermoacoustic signals.
The following section presents the electromagnetic interferences which are coupled into the detection path before proceeding to the first documented thermoacoustic signal in response to CW stimulation.

8.3.1 Electromagnetic interferences

Figure 8.12 plots the second harmonic of the high power amplifier. The signal was coupled into the detection path consisting of a shielded cable connected to the transducer (3.5 MHz) which was implemented in the FD-TAT system as described in figure 8.1. Furthermore, the transducer was connected to a spectrum analyzer (Model: MS2036C, Anritsu, Kanagawa, Japan) which allowed for spectral measurements. The interference is occurring at $f_{EMI} \approx 1.64$ MHz equivalent to the double of the excitation frequency $f_{CW} \approx 820$ kHz. Note that the amplitude of the interference exhibits a power level of almost -95 dBm. The signal to noise ratio is calculated to $\mathrm{SNR}_{EMI} \approx 50$ dB.

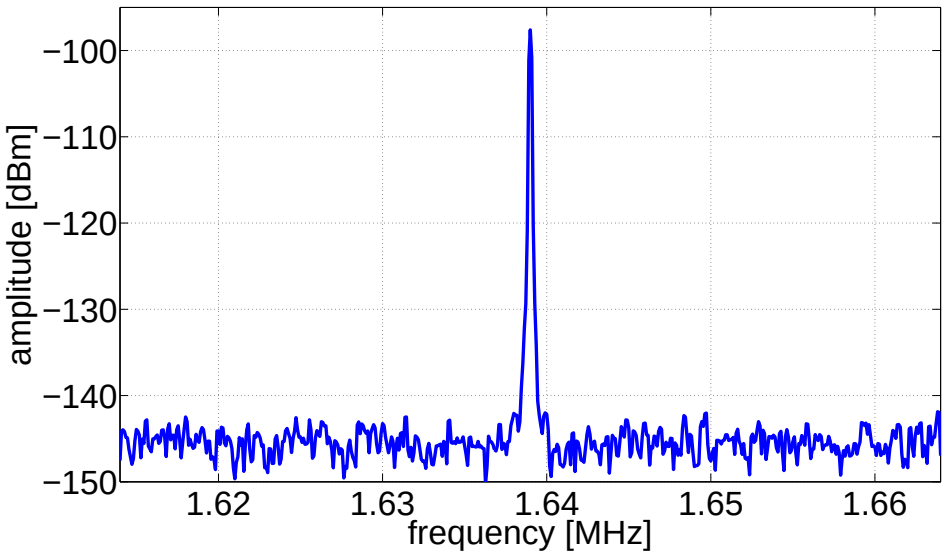

Figure 8.12: Second harmonic of the FD-TAT system which is coupled into the detection path as an electromagnetic interference

8.3.2 Thermoacoustic signal from highly dissipative medium

The measurement from the previous section 8.3.1 supports one conclusion. In order to detect a thermoacoustic signal, it has to outreach the amplitude of the electromagnetic interference. This can be achieved by employing matter which absorbs a significant amount of energy when exposed to AC-magnetic fields. Therefore, a conductive object ($\varnothing$ 1 mm) was placed in the FD-TAT sample holder. Theoretically, referring back to chapter 2, section 2.3.3.5, eddy currents are induced in conductive materials which are exposed to high frequent magnetic fields, giving rise to significant heating of the matter.
Upon operating the system and introducing the conductive matter into the sample holder, a CW thermoacoustic signal which was exceeding the EMI was detected as shown in figure 8.13. The amplitude of the signal is ~ -85 dBm featuring a signal to noise ratio $\mathrm{SNR}_{TAS} \approx 60$ dB. Note that the thermoacoustic signal is congruent to the electromagnetic interference which is additionally plotted from figure 8.12 for comparison.

8.4 Summary and discussion

This chapter presented a frequency domain thermoacoustic system aiming for magnetic excitation. It consisted of a dedicated high power amplifier which allowed for monofrequent stimulation. The system is able to focus magnetic energy onto small areas

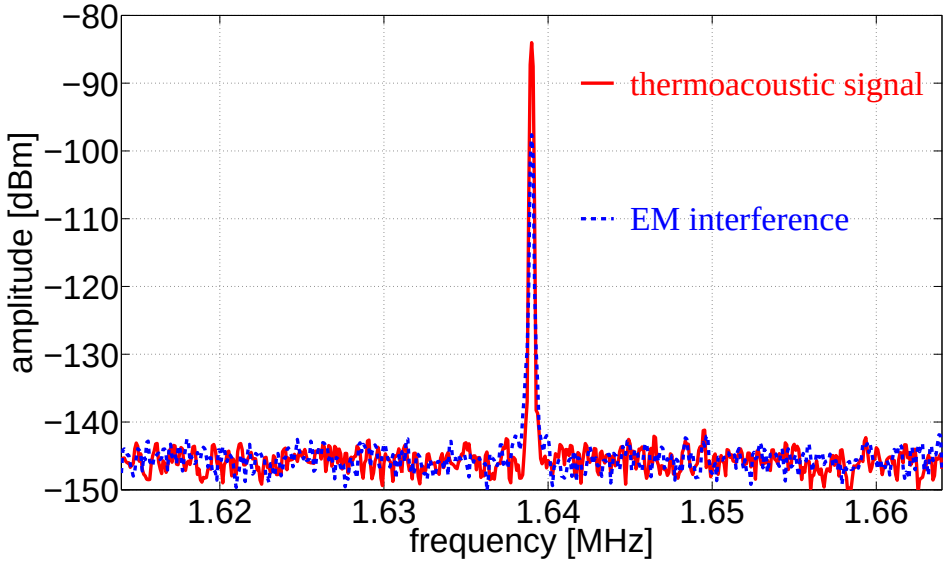

Figure 8.13: Thermoacoustic signal in response to CW excitation at $f_{CW} = 820$ kHz along with the electromagnetic interference from figure 8.12

defined by the resonance element, i.e. a Helmholtz coil. Additionally, the Helmholtz coil facilitated acoustic detection since it offers a window to accommodate the transducer unit.

Operating the system exhibited a strong electromagnetic interference which coincides with the thermoacoustic response. Nevertheless, introducing highly conductive matter into the system proved the first documented thermoacoustic signal following CW excitation.

However, a continuation of this approach will only result in the successful detection of magnetic nanoparticles if the detection can be decoupled from the excitation. This can be achieved by employing optical based mechanical stress detectors instead of PZT based transducers [110], [109]. Thus, EMI can be prevented from being coupled into the detection path, enabling the detection of the low thermoacoustic signals.

9 Conclusion and outlook

9.1 Conclusive remarks and compact review

This work was dedicated to theoretical considerations and experimental implementations in opto- and thermoacoustic imaging.
Driven by the overall objective to implement a novel approach towards thermoacoustic tomography, this research was directed from its initial time domain approach towards an implementation of photoacoustic methods in the frequency domain.

The main interest of this research implied the overcoming of limitations associated with conventional thermoacoustic imaging, i.e. low resolution confined to structural imaging. Thus, a new cost-efficient hardware design should allow for the whole range of imaging applications, including structural, functional and molecular imaging *in-vivo*. A prototype near-field radiofrequency thermoacoustic (NRT) tomography system was built in particular aiming towards small animal imaging at high spatial resolution. The performance of the system revealed the high resolution capabilities with the expected conductive/dielectric contrast; however, the application range of NRT is still limited to anatomical imaging since appropriate exogenous probes like Gadolinium, magnetites or carbon nanotubes did not contribute to enhanced imaging contrast.

Based on hyperthermia for cancer therapy, a new approach was pursued which now aimed at CW excitation instead of pulsed stimulation. Prior to the implementation in thermoacoustics, the method was tested with CW coded optical light. A dedicated tomography system was built which allowed for *in-vivo* imaging, demonstrating undocumented cross sectional views of a mouse tail before, during and after ICG injection.

Frequency domain thermoacoustic tomography inherently struggles with several drawbacks like low signal to noise ratio and electromagnetic interferences. Therefore, a so called quasi CW system was developed which enabled for the first time the detection

of narrowband acoustic responses following monofrequent RF stimulation.

The time domain to frequency domain transition finally directed this research to a CW based thermoacoustic tomography system. With respect to the magnetic field absorption of hyperthermia agents like paramagnetic and superparamagnetic nanoparticles (SPIOs), a system with dominant magnetic field was designed. Although low SNR and EM interferences still are an issue in this system, the successful detection of a CW thermoacoustic signal was achieved, although heat dissipation was not based on relaxation mechanisms but rather on eddy currents.

9.2 Outlook and future directions

The developed CW based thermoacoustic tomography system bears huge potential in the field of biomedical diagnosis. Since the FD-TAT system exhibits strong magnetic field amplitudes, biological tissue with its low magnetic field absorption offers minor intrinsic contrast while the administration of extrinsic magnetic agents can direct diagnosis to new imaging applications. Thus, the tracking of magnetic particles in human body at ultrasound resolution is feasible.
Furthermore, the FD-TAT system can be employed as a theranostic instrument since it utilizes modified hyperthermic technology adapted to an imaging device. This results in an imaging guided thermal therapy system for cancer treatment which enables monitoring the progress of tumor ablation while simultaneously performing treatment.

However, modifications have to be made to the prototype system.
First, a broadband approach allowing for frequency modulation has to be implemented in order to facilitate imaging. More importantly, the detection has to be changed from PZT based transducers to mechanical stress detectors which are based on interferometric technology. This is important since the decoupling of the excitation from the detection will allow for the successful capturing of the low CW thermoacoustic signals.

However, changing from PZT based transducers to optically based acoustic detectors is also linked with significant deficiencies. Whereas PZT based acoustic detectors allow for easy implementation, stable operation conditions and high sensitivity, current state-of-the-art optical hydrophones are characterized by low sensitivity and complex technical requirements.

A dedicated interferometric detector is being developed at the IBMI which will ultimately be implemented in the FD-TAT system for tomographic imaging [110], [109], [108]. This detection system surpasses other optical detectors and provides the expected sensitivity to detect the low CW thermoacoustic signals. Especially the combination of the developed FD-TAT system with the interferometric acoustic detector may result in a theranostic imaging modality which will be able to launch new applications in thermoacoustic imaging.

Appendix A

Dielectric properties of tissue

A.1 Parameters for Cole Cole model

tissue type	ε_∞	$\Delta\varepsilon_1$	τ_1 [ps]	α_1	$\Delta\varepsilon_2$	τ_2 [ns]	α_2	$\Delta\varepsilon_3$	τ_3 [µs]	α_3	$\Delta\varepsilon_4$	τ_4 [ms]	α_4	σ
muscle	4.0	50.0	7.23	0.10	7000	353.68	0.10	1.2×10^6	318.31	0.10	2.5×10^7	2.274	0.00	0.2
fat	2.5	9.0	7.96	0.20	35	15.92	0.10	3.3×10^4	159.15	0.05	1.0×10^7	15.915	0.01	0.035
skin (wet)	4.0	39.0	7.96	0.10	280	79.58	0.00	3.0×10^4	1.59	0.16	3.0×10^4	1.592	0.2	0.0004
liver	4.0	39.0	8.84	0.10	6000	530.52	0.20	5.0×10^4	22.74	0.20	3.0×10^7	15.915	0.05	0.02

Table A.1: Parameters for the multiple Cole Cole approach in equation 2.59 (taken from [37])

Bibliography

[1] Aharoni A,
”Brown’s ”fundamental theorem” revisited”
J. Appl. Phys. **90**, 4645 (2001).

[2] Andrä W, Nowak H,
”Magnetism in Medicine - A Handbook”
2nd Edition, Wiley Interscience (2007).

[3] American National Standards Institute,
”American National Standard for the Safe Use of Lasers in Health Care Facilities: Standard Z136.1-2000”
ANSI, Inc., New York (2000).

[4] Atkinson WJ, Brezovich IA, and Chakraporty DP,
”Usable Frequencies in Hyperthermia with Thermal Seeds”
IEEE Trans. Biomed. Eng. **31** (1), 70-75 (1984).

[5] Bell AG,
”On the Production and Reproduction of Sound by Light”
Am. J. Sci., Third Series, vol XX (118), 305-324 (1880).

[6] Bertotti G,
”Hysteresis in Magnetism”
Academic Press (1998).

[7] Blumm J, Lindemann A, Min S,
”Thermal characterization of liquids and pastes using the flash technique”
Thermochim. Acta **455**, 26-29 (2007).

[8] Born M and Wolf E,
”Principles of Optics - Electromagnetic Theory of Propagation Interference and Diffraction of Light”
Sixth Edition, Pergamom Press (1993).

[9] Bond EJ, Li X, Hagness SC, and Van Veen BD,
”Microwave Imaging via Space-Time Beamforming for Early Detection of Breast Cancer”
IEEE Trans. Antennas Propag. **51** (8), 1690-1705 (2003).

[10] Bowen T, Nasoni RL, Pfifer AE and Sembroski GH,
”Some Experimental Results on the Thermoacoustic Imaging of Tissue Equivalent Phantom Materials”
Proc. IEEE Ultrason. Symp. **2**, 823-827 (1981).

[11] Bowen T,
”Radiation-induced thermoacoustic soft tissue imaging”
Proc. IEEE Ultrason. Symp. **2**, 817-822 (1981).

[12] Boyer C, Whittaker MR, Bulmus V, Liu J and Davis TP,
”The design and utility of polymer-stabilized iron-oxide nanoparticles for nanomedicine applications”
NPG Asia Mater. **2** (1), 23-30, (2010).

[13] Brecht HP, Su R, Fronheiser M, Ermilov SA, Conjusteau A, Oraevsky AA,
”Whole-body three-dimensional optoacoustic tomography system for small animals”
J. Biomed. Opt. **14** (6), 064007-1 - 064007-8 (2009).

[14] Brown WF, Jr,
”The Fundamental Theorem of the theory of fine ferromagnetic particles”
Ann. N.Y. Acad. Sci. **147**, 463 (1969).

[15] Brown WF, Jr,
”Thermal Fluctuations of a Single-Domain Particle”
Phys. Rev. **130** (5), 1677-1686 (1963).

[16] Buehler A, Herzog E, Razansky D, and Ntziachristos V,
”Video rate optoacoustic tomography of mouse kidney perfusion”
Opt. Lett. **35** (14), 2475-2477 (2010).

[17] Chance B, Cope M, Gratton E, Ramanujam N, and Tromberg B,
”Phase measurement of light absorption and scatter in human tissue”
Rev. Sci. Instrum. **69**, 3457 (1998).

[18] Cherukuri P, Glazer ES, and Curley SA,
”Targeted Hyperthermia Using Metal Nanoparticles”
Adv. Drug Deliver. Rev. **62** (3), 339-345 (2010).

[19] Christ A, Samaras T, Klingenböck A and Kuster N,
”Characterization of the electromagnetic near-field absorption in layered biological tissue in the frequency range from 30 MHz to 6000 MHz”
Phys. Med. Biol. **51**, 4951-4965 (2006).

[20] Collin RE,
”Foundations for Microwave Engineering”
Second Edition, IEEE Press Series on Electromagnetic Wave Theory, Wiley Interscience (2001).

[21] De Boer JF, Cense B, Hyle Park B, Pierce MC, Tearney GJ, and Bouma BE,
”Improved signal-to-noise ratio in spectral-domain compared with time-domain optical coherence tomography”
Opt. Lett. **28** (21), 2067-2069 (2003).

[22] De la Zerda A, Zavaleta C, Keren S, Vaithilingham S, Bodapati S, Liu Z, Levi J, Smith BR, Ma T-J, Oralkan O, Cheng Z, Chen X, Dai H, Khuri-Yakub BT, and Gambhir SS,
”Carbon nanotubes as photoacoustic molecular imaging agents in living mice”
Nat. Nanotech. **3**, 557-562 (2008).

[23] Derfus AM, Maltzahn G, Harris TJ, Duza T, Vecchio KS, Ruoslahti E, and Bhatia SN,
”Remotely Triggered Release from Magnetic Nanoparticles”
Adv. Mater. **19** (22), 3932-3936 (2008).

[24] Dobrucki LW and Sinusas AJ,
”PET and SPECT in cardiovascular molecular imaging”
Nat. Rev. Cardiol. **7**, 38-47 (2010).

[25] Douglas de Vries I,
”High Power and High Frequency Class-DE Inverters”
Dissertation - Department of Electrical Engineering - University of Cape Town (1999).

[26] Drexler W and Fujimoto JG,
”Optical Coherence Tomography - Technology and Applications”
Springer Verlag, Berlin Heidelberg (2008).

[27] Eckhart AT, Balmer RT, See WA and Patch SK,
”*Ex vivo* Thermoacoustic Imaging Over Large Fields of View With 108 MHz Irradiation”
IEEE Trans. Biomed. Eng. **58** (8), 2238-2246 (2011).

[28] Fairchild Semiconductor,
”AN9012 - Induction Heating System Topology Review”
Discrete Application, Power Device Division, Fairchild Semiconductor (2000).

[29] Fallon D, Yan L, Hanson GW, and Patch SK,
”rf testbed for thermoacoustic tomography”
Rev. Sci. Instrum. **80**, 064301-9 (2009).

[30] Fan Y and Mandelis A, Spirou G, Vitkin IA,
”Development of a laser photothermoacoustic frequency-swept system for subsurface imaging: Theory and experiment”
J. Acoust. Soc. Am. **116** (6), 3523-3533 (2004).

[31] Fannin PC and Charles SW,
”The study of a ferrofluid exhibiting both Brownian and Néel relaxation”
J. Phys. D: Appl. Phys. **22**, 187-191 (1989).

[32] Fear EC, Li X, Hagness SC, and Stuchly MA,
”Confocal Microwave Imaging for Breast Cancer Detection: Localization of Tumors in Three Dimensions”
IEEE Trans. Biomed. Eng. **49** (8), 812-822 (2002).

[33] Foster KR, Schepps JL, and Schwan HP,
”Microwave Dielectric Relaxation in Muscle”
Biophys. J. **29**, 271-282 (1980).

[34] Foster KR, Schepps JL, Stoy RD, and Schwan HP,
”Dielectric Properties of Brain Tissue between 0.01 and 10GHz”
Phys. Med. Biol. **24** (6), 1177-1187 (1979).

[35] Gabriel C, Gabriel S and Corthout E,
”The dielectric properties of biological tissues: I. Literature survey”
Phys. Med. Biol. **41**, 2231-2249 (1996).

[36] Gabriel S, Lau RW and Gabriel C,
”The dielectric properties of biological tissues: II. Measurements in the frequency range 10 Hz to 20 GHz”
Phys. Med. Biol. **41**, 2251-2269 (1996).

[37] Gabriel S, Lau RW and Gabriel C,
”The dielectric properties of biological tissues: III. Parametric models for the dielectric spectrum of tissues”
Phys. Med. Biol. **41**, 2271-2293 (1996).

[38] Garcia ME, Pastor GM, and Bennemann KH,
”Theory for the Photoacoustic Response to X-Ray Absorption”
Phys. Rev. Lett. **61** (1), 121-124 (1988).

[39] Gibson AP, Hebden JC and Arridge SR,
”Recent advances in diffuse optical imaging”
Phys. Med. Biol. **50**, R1-R43 (2005).

[40] Glatz J, Deliolanis NC, Buehler A, Razansky D, and Ntziachristos V,
”Blind source unmixing in multi-spectral optoacoustic tomography”
Opt. Express **19** (4), 3175-3184 (2011).

[41] Gleich B & Weizenecker J,
”Tomographic imaging using the nonlinear response of magnetic particles”
Nature **435**, 1214-1217 (2005).

[42] Glöckl G, Hergt R, Zeisberger M, Dutz S, Nagel S and Weitschies W,
”The effect of field parameters, nanoparticle properties and immobilization on the specific heating power in magnetic particle hyperthermia”
J. Phys.: Condensed Matter **18**, 2935 - 2949 (2006).

[43] Goodenough JB,
”Summary of Losses in Magnetic Materials”
IEEE Trans. Magn. **38** (5), 3398-3408 (2002).

[44] Gubin SP,
”Magnetic nanoparticles”
Wiley-VCH, Berlin, 1. Edition (2009).

[45] Hamill DC,
”Class DE Inverters and Rectifiers for DC-DC Conversion”
Preprint: Power Electronics Specialists Conference, Baveno, Italy (1996).

[46] Haskell RC, Svaasand LO, Tsay T-T, Feng T-C and McAdams MS, Tromberg BJ, ”Boundary conditions for the diffusion equation in radiative transfer” J. Opt. Soc. Am. A **11** (10), 2727-2741 (1994).

[47] Hergt R, Dutz S, Müller R and Zeisberger M, ”Magnetic particle hyperthermia: nanoparticle magnetism and materials development for cancer therapy” J. Phys.: Condensed Matter **18**, 2919 - 2934 (2006).

[48] Hiergeist R, Andrä W, Buske N, Hergt R, Hilger I, Richter U, Kaiser U, ”Application of magnetite ferrofluids for hyperthermia” J. Magn. Magn. Mater. **201**, 420 - 422 (1999).

[49] Hurt WD, ”Multiterm Debye Dispersion Relations for Permittivity of Muscle” IEEE Trans. Biomed. Eng., **32** (1), 60-64 (1985).

[50] Hyperphysics - Georgia State University http://hyperphysics.phy-astr.gsu.edu/hbase/hframe.html (2012).

[51] Ivkov R, DeNardo SJ, Daum W, Foreman AR, Goldstein RC, Nemkov VS, and DeNardo GL, ”Application of High Amplitude Alternating Magnetic Fields for Heat Induction of Nanoparticles Localized in Cancer” Clin. Cancer Res. **1** (11), 7093-7103 (2005).

[52] Jin X and Wang LHV, ”Thermoacoustic tomography with correction for acoustic speed variations” Phys. Med. Biol. **51**, 6437-6448 (2006).

[53] Jordan A, Scholz R, Wust P, Fähling H, Felix R, ”Magnetic Fluid hyperthermia (MFH): Cancer treatment with AC magnetic field induced excitation of biocompatible superparamagnetic nanoparticles” J. Magn. Magn. Mater. **201**, 413-419 (1999).

[54] Jordan A, Wust P, Fähling H, John W, Hinz A and Felix R, ”Inductive heating of ferrimagnetic particles and magnetic fluids: physical evaluation of their potential for hyperthermia” Int. J. Hyperther. **9** (1), 51-68 (1993).

[55] Judenhofer MS, Wehrl HF, Newport DF, Catana C, Siegel SB, Becker M, Thielscher A, Kneilling M, Lichy MP, Eichner M, Klingel K, Reischl G, Widmaier S, Röcken M, Nutt RE, Machulla HJ, Uludag K, Cherry SR, Claussen CD and Pichler BJ, "Simultaneous PET-MRI: a new approach for functional and morphological imaging"
Nat. Med. **14** (4), 459 - 465 (2008).

[56] Kallumadil M, Tada M, Nakagawa T, Abe M, Southern P, Pankhurst QA, "Suitability of commercial colloids for magnetic hyperthermia"
J. Magn. Magn. Mater. **321**, 1509-1513 (2009).

[57] Kellnberger S, Hajiaboli A, Razansky D and Ntziachristos V, "Near-field thermoacoustic tomography of small animals"
Phys. Med. Biol. **56**, 3433-3444 (2011).

[58] Kellnberger S, Hajiaboli A, Sergiadis G, Razansky D, and Ntziachristos V, "High resolution imaging with impulse based thermoacoustic tomography"
Proc. SPIE 8089, 808905 (2011), SPIE Conference, Molecular Imaging III, 22 May 2011, Munich, Germany (2011).

[59] Kellnberger S, Deliolanis NC, Queirós D, Sergiadis G and Ntziachristos V, "In-vivo frequency domain optoacoustic tomography"
Opt. Lett. **37** (16), 3423-3425 (2012).

[60] Koestli K, Frenz M, Bebie H, and Weber R, "Temporal backward projection of optoacoustic pressure transients using Fourier transform methods"
Phys. Med. Biol. **46**, 1863-1872 (2001).

[61] Koizumi H, Iwadare M, Mori S and Ideka K, "A Class D Type High Frequency Tuned Power Amplifier with Class E Switching Conditions"
IEEE Int. Symp. Circ. S. **5**, 105-108 (1994).

[62] Koizumi H, Suetsugu T, Fujii M, Shinoda K, Mori S, and Ideka K, "Class DE High-Efficiency Tuned Power Amplifier"
IEEE Trans. Circuits Syst. I, Fundam. Theory Appl. **43** (1) (1996).

[63] Kruger RA, Kiser WL, Jr., Miller KD, Reynolds HE, "Thermoacoustic CT: Imaging Principles"
Proc. SPIE Vol. 3916, p. 150-159 (2000).

[64] Kruger RA, Kopecky KK, Aisen AM, Reinecke DR, Kruger GA and Kiser WL, Jr, "Thermoacoustic CT with Radio Waves: A Medical Imaging Paradigm" Radiology, **211**:275-278 (1999).

[65] Kruger RA, Liu P, Fang YR, and Appledorn CR, "Photoacoustic ultrasound (PAUS) - Reconstruction tomography" Med. Phys. **22** (10), 1605-1609 (1995).

[66] Kruger RA, Miller KD, Reynolds HE, Kiser WL, Jr, Reinecke DR and Kruger GA, "Breast Cancer in Vivo: Contrast Enhancement with Thermoacoustic CT at 434 MHz - Feasibility Study" Radiology, **216**:279-283 (2000).

[67] Kruger RA, Reinecke DR, and Kruger GA, "Thermoacoustic computed tomography-technical considerations" Med. Phys. **26** (9), 1832-1837 (1999).

[68] Kruger RA, Stantz K, Kiser WL, Jr, "Thermoacoustic CT of the Breast" Proc. SPIE 4682, 521 (2002).

[69] Ku G and Wang LHV, "Scanning thermoacoustic tomography in biological tissue" Med. Phys. **27** (5), 1195 - 1202 (2000).

[70] Ku G and Wang LHV, "Scanning microwave-induced thermoacoustic tomography: Signal, resolution, and contrast" Med. Phys. **28** (1), 4-10 (2000).

[71] Ku G, Fornage BD, Jin X, Xu M, Hunt KK and Wang LHV, "Thermoacoustic and Photoacoustic Tomography of Thick Biological Tissues Toward Breast Imaging" Technol. Cancer Res. T. **4** (5), 559-565 (2006).

[72] Landsman MLJ, Kwant G, Mook GA, and Zijlstra WG, "Light-absorbing properties, stability, and spectral stabilization of indocyanine green" J. Appl. Physiol. **40** (4), 575-583 (1976).

[73] Larsen LE and Jacobi JH,
"Microwave scattering parameter imagery of an isolated canine kidney"
Med. Phys. **6** (5), 394-403 (1979).

[74] Lee JH, Jang JT, Choi JS, Moon SH, Noh SH, Kim JW, Kim JG, Kim IS, Park KI and Cheon J,
"Exchange-coupled magnetic nanoparticles forefficient heat induction"
Nat. Nanotechnol. **6**, 418-422 (2011).

[75] Low AF, Tearney GJ, Bouma BE and Jang IK,
"This article offers Technology Insight: optical coherence tomography - current status and future development"
Nat. Clin. Pract. Cardiovasc. Med. **3** (3), 154 - 162 (2005).

[76] Ma R, Taruttis A, Ntziachristos V, and Razansky D,
"Multispectral optoacoustic tomography (MSOT) scanner for whole-body small animal imaging"
Opt. Express **17** (24), 21414 - 21426 (2009).

[77] Mashal A, Booske JH and Hagness SC,
"Toward contrast-enhanced microwave-induced thermoacoustic imaging of breast cancer: an experimental study of the effects of microbubbles on simple thermoacoustic targets"
Phys. Med. Biol. **54**, 641-650 (2009).

[78] Meaney PM, Fanning MW, Li D, Poplack SP, and Paulsen KD,
"A Clinical Prototype for Active Microwave Imaging of the Breast"
IEEE Trans. Microw. Theory Tech. **48** (11), 1841-1853 (2000).

[79] Mornet S, Vasseur S, Grasset F and Duguet E,
"Magnetic nanoparticle design for medical diagnosis and therapy"
J. Mater. Chem. **14**, 2161-2175 (2004).

[80] Motrescu VC and Rienen VU,
"Simulation of electromagnetic fields in the human body using finite integration technique (FIT)"
Biomed. Tech. **47**, 282-4 (2002).

[81] Néel L,
"Théorie du traînage magnétique des ferromagnétiques en grains fins avec applica-

tion aux terres cuites"
Ann. Géophys. **5**, 99-136 (1949).

[82] Nie L, Ou Z, Yang S, and Xing D,
"Thermoacoustic molecular tomography with magnetic nanoparticle contrast agents for targeted tumor detection"
Med. Phys. **37** (8), 4193-4200 (2010).

[83] Nie L, Xing D, and Yang S,
"*In vivo* detection and imaging of low-density foreign body with microwave-induced thermoacoustic tomography"
Med. Phys. **36** (8), 3429-3437 (2009).

[84] Ntziachristos V,
"Going deeper than microscopy: the optical imaging frontier in biology"
Nature Methods **7** (8), 603-614 (2010).

[85] Ntziachristos V,
"Introduction to Biological Imaging (ME002) - Modern imaging methods for the post-genomic era"
Chair for Biological Imaging, TUM-Lecture (2011).

[86] Ntziachristos V, Ma XH, and Chance B,
"Time-correlated single photon counting imager for simultaneous magnetic resonance and near-infrared mammography"
Rev. Sci. Instrum. **69**, 4221 (1998).

[87] Ntziachristos V and Razansky D,
"Molecular Imaging by Means of Multispectral Optoacoustic Tomography (MSOT)"
Chem. Rev. **110**, 2783-2794 (2010).

[88] Ntziachristos V, Ripoll J, Wang LHV & Weissleder R,
"Looking and listening to light: the evolution of whole-body photonic imaging"
Nat. Biotechnol. **23** (3), 313-320 (2005).

[89] Omar M, Kellnberger S, Sergiadis G, Razansky D, Ntziachristos V,
"Near-field thermoacoustic imaging with transmission line pulsers"
Med. Phys. **39** (7), 4460-4466 (2012).

[90] Omar M, Kellnberger S, Sergiadis G, Razansky D, Ntziachristos V,
"Near-field radio-frequency thermo-acoustic imaging based on transmission lines for optimized performance"

SPIE Photons Plus Ultrasound: Imaging and Sensing 2012, Conference Proceedings 8223, Eds: Alexander A. Oraevsky; Lihong V. Wang (2012).

[91] Orfanidis SJ,
”Electromagnetic Waves and Antennas”
ECE Department - Rutgers University (2011).

[92] Patel CKN, Tam AC,
”Pulsed optoacoustic spectroscopy of condensed matter”
Rev. Mod. Phys. **53** (3), 517-553 (1981).

[93] Pozar DM,
”Microwave Engineering”
Wiley Interscience, 3rd Edition (2005).

[94] Prahl S,
”Optical absorption of oxy and deoxy hemoglobin based on data from Gratzer WB, Med. Res. Council Labs, Holly Hill, London and Kollias N, Wellman Laboratories”
Harvard Medical School, Boston (1999).

[95] Pramanik M, Ku G, Li C, and Wang LHV,
”Design and evaluation of a novel breast cancer detection system combining both thermoacoustic (TA) and photoacoustic (PA) tomography”
Med. Phys. **35** (6), 2218-2223 (2008).

[96] Pramanik M, Swierczewska M, Green D, Sitharaman B, and Wang LHV,
”Single-walled carbon nanotubes as a multimodal-thermoacoustic and photoacoustic-contrast agent”
J. Biomed. Opt. **14**, 034018-1 - 034018-8 (2009).

[97] Quon A and Gambhir SS,
”FDG-PET and Beyond: Molecular Breast Cancer Imaging”
J. Clin. Oncol. **23** (8), 1664 - 1673 (2005).

[98] Rajadhyaksha M, Grossman M, Esterowitz D, Webb RH, and Anderson RR,
”*In Vivo* Confocal Scanning Laser Microscopy of Human Skin: Melanin Provides Strong Contrast”
J. Invest. Dermatol. **104** (5), 946-952 (1995).

[99] Razansky D, Deliolanis NC, Vinegoni C, Ntziachristos V,
"Deep Tissue Optical and Optoacoustic Molecular Imaging Technologies for Pre-Clinical Research and Drug Discovery"
Curr. Pharm. Biotechnol. **13** (4), 505-522(19) (2012).

[100] Razansky D, Distel M, Vinegoni C, Ma R, Perrimon N, Köster RW and Ntziachristos V,
"Multispectral opto-acoustic tomography of deep-seated fluorescent proteins *in-vivo*"
Nat. Photon. **3**, 412-417 (2009).

[101] Razansky D, Kellnberger S, and Ntziachristos V,
"Near-field radiofrequency thermoacoustic tomography with impulse excitation"
Med. Phys. **37** (9), 4602 - 4607 (2010).

[102] Razansky D, Kellnberger S, and Ntziachristos V,
"Impulse-driven near-field radiofrequency thermoacoustic (NRT) tomography"
Proceedings SPIE, 7899, Photons Plus Ultrasound: Imaging and Sensing; 22.-27. January 2011, San Francisco, USA (2011).

[103] Razansky D and Ntziachristos V,
"Hybrid photoacoustic fluorescence molecular tomography using finite-element-based inversion"
Med. Phys. **34** (11), 4293-4301 (2007).

[104] Razansky D, Soldea DF, and Einziger PD,
"Generalized transmission-line model for estimation of cellular handset power absorption in biological tissues"
IEEE Trans. Electromagn. Compat. **47**, No. 1, 67 (2005).

[105] Rogers WJ, Meyer CH and Kramer CM,
"Technology Insight: in vivo cell tracking by use of MRI"
Nat. Clin. Pract. Cardiovasc. Med. **3**, 554-562 (2006).

[106] Rosencwaig A,
"Thermoacoustic Microscopy"
United States Patent No. 4,255,971 (1981).

[107] Rosensweig RE,
"Heating magnetic fluid with alternating magnetic field"
J. Magn. Magn. Mater. **252**, 370-374 (2002).

[108] Rosenthal A, Caballero MAA, Kellnberger S, Razansky D, and Ntziachristos V,
"Spatial characterization of the response of a silica optical fiber to wideband ultrasound"
Opt. Lett. **37** (15), 3174-3176 (2012).

[109] Rosenthal A, Kellnberger S, Sergiadis G, and Ntziachristos V,
"Wideband fiber-interferometer stabilization with variable phase"
IEEE Photon. Technol. Lett. **24** (17), 1499-1501 (2012).

[110] Rosenthal A, Razansky D, and Ntziachristos V,
"High-sensitivity compact ultrasonic detector based on a pi-phase-shifted fiber Bragg grating"
Opt. Lett. **36** (10), 1833 - 1835 (2011).

[111] Sadiku MNO,
"Numerical Techniques in Electromagnetics"
CRC press, 2nd Edition (2001).

[112] Schwan HP, and Foster KR
"RF-Field Interactions with Biological Systems: Electrical Properties and Biophysical Mechanisms"
Proc. IEEE **68**, 104-113 (1980).

[113] Segelstein D,
"The Complex Refractive Index of Water"
M. S. Thesis, University of Missouri, Kansas City (1981).

[114] Shapiro EM, Skrtic S, Sharer K, Hill JM, Dunbar CE, and Koretsky AP,
"MRI detection of single particles for cellular imaging"
PNAS **101** (30), 10901-10906 (2004).

[115] Skolnik M,
"Radar Handbook"
Second Edition, The McGraw-Hill Companies (1990).

[116] Skolnik M,
"Radar Handbook"
Third Edition, The McGraw-Hill Companies (2008).

[117] Skumiel A,
"Suitability of water based magnetic fluid with $CoFe_2O_4$ particles in hyperthermia"
J. Magn. Magn. Mater. **307**, 85-90 (2006).

[118] Srinivasan VJ, Chen Y, Duker JS, and Fujimoto JG,
"*In Vivo* Functional Imaging of Intrinsic Scattering Changes in the Human Retina with High-speed Ultrahigh Resolution OCT"
Opt. Express **17** (5), 3861-3877 (2009).

[119] Taflove A and Hagness SC,
"Computational Electrodynamics: The Finite-Difference Time-Domain Method"
Third Edition, Boston, MA; Artech House, (2007).

[120] Telenkov SA, Mandelis A,
"Fourier-domain biophotoacoustic subsurface depth selective amplitude and phase imaging of turbid phantoms and biological tissue"
J. Biomed. Opt. **11** (4), 044006 (2006).

[121] Telenkov SA, Mandelis A,
"Photothermoacoustic imaging of biological tissues: maximum depth characterization comparison of time and frequency domain measurements"
J. Biomed. Opt. **14** (4), 044025 (2009).

[122] Telenkov S and Mandelis A,
"Signal-to-noise analysis of biomedical photoacoustic measurements in time and frequency domains"
Rev. Sci. Instr. **81**, 124901 (2010).

[123] Telenkov S, Mandelis A, Lashkari B and Forcht M,
"Frequency-domain photothermoacoustics: Alternative imaging modality of biological tissues"
J. Appl. Phys. **105**, 102029 (2009).

[124] Wang LHV,
"Photoacoustic Imaging and Spectroscopy"
Boca Raton, FL, CRC Press (2009).

[125] Wang LHV, Wu HI,
"Biomedical Optics - Principles and Imaging"
John Wiley & Sons, Inc. (2007).

[126] Wang LHV, Hu S,
"Photoacoustic Tomography: In Vivo Imaging from Organelles to Organs"
Science **23**, **335** (6075), 1458-1462 (2012).

[127] Weissleder R, Pittet MJ,
"Imaging in the era of molecular oncology"
Nature **452**, 580-589 (2008).

[128] Xu M and Wang LHV,
"Universal back-projection algorithm for photoacoustic computed tomography"
Phys. Rev. **E71**, 016706 (2005).

[129] Xu M and Wang LHV,
"Photoacoustic imaging in biomedicine"
Rev. Sci. Instrum. **77**, 041101 (2006).

[130] Xu Y and Wang LHV,
"Signal processing in scanning thermoacoustic tomography in biological tissue"
Med. Phys. **28** (7), 1519-1524 (2001).

[131] Ye G,
"PSTD Method for Thermoacoustic Tomography (TAT) and Related Experimental Investigation"
Dissertation, Department of Electrical and Computer Engineering, Duke University (2009).

[132] Yun SH, Tearney GJ, de Boer JF, Iftimia N and Bouma BE,
"High-speed optical frequency-domain imaging"
Opt. Express **11** (22), 2953-2963 (2003).

[133] Zinke O and Brunswig H,
"Hochfrequenztechnik 1 - Hochfrequenzfilter, Leitungen, Antennen"
Springer Verlag, 6. Auflage, 1999.

[134] Zhao DL, Zhang HL, Zeng XW, Xia QS,
"Inductive heat property of Fe_3O_4/polymer composite nanoparticles in an ac magnetic field for localized hyperthermia"
Biomed. Mater. **1**, 198-201 (2006).